Physical, Chemical, & Nano Sciences Center

Research Briefs

2008

Sandia National Laboratories
Albuquerque, New Mexico

A Multiprogram Laboratory

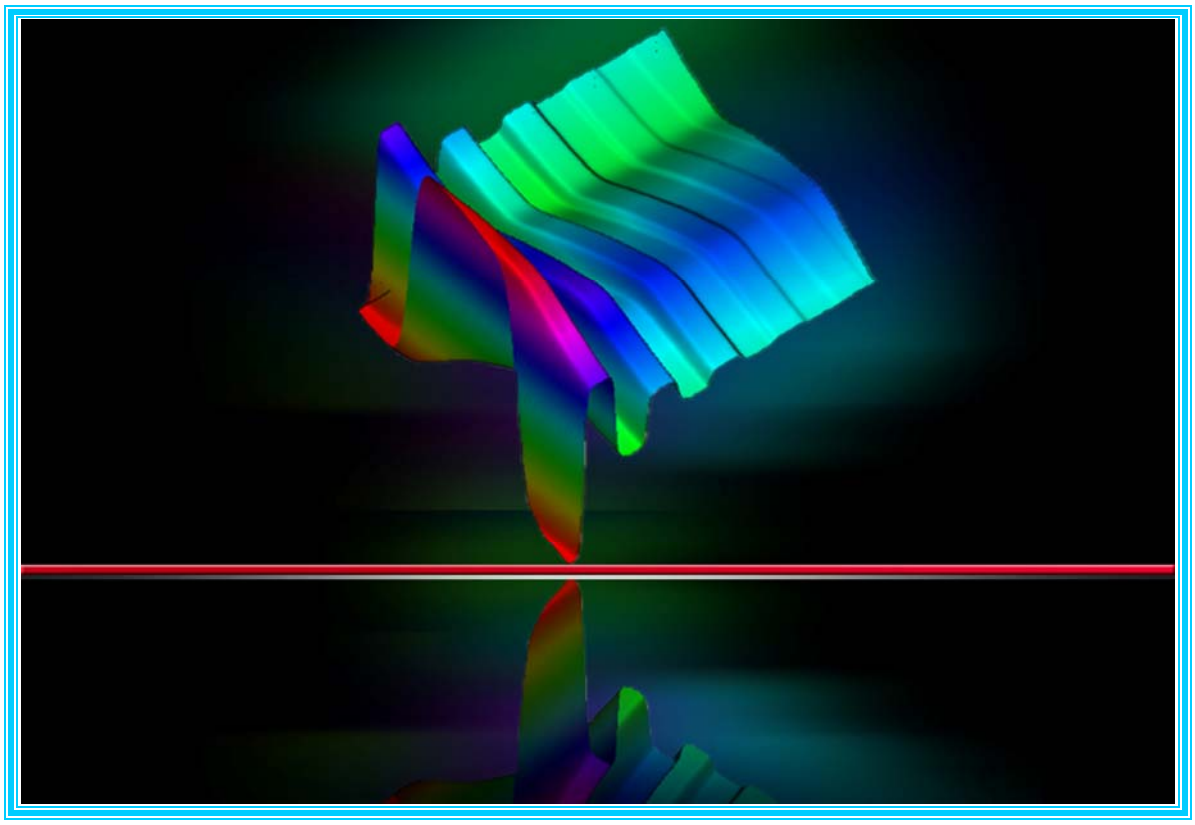

Research Briefs for the Physical, Chemical, & Nano Sciences Center is published by Sandia National Laboratories, a multiprogram laboratory operated by Sandia Corporation, a Lockheed Martin Company, for the United States National Nuclear Security Administration and the Department of Energy under Contract DE-AC04-94AL85000.

Additional complimentary copies are available by contacting:

Julia M. Phillips
Physical, Chemical, & Nano Sciences Center, 1100
Sandia National Laboratories
Albuquerque, NM 87185-1427

Phone: (505) 844-1071
Fax: (505) 844-6098
Email: jmphill@sanida.gov
url: http://www.sandia.gov/pcnsc

Research Briefs

Editors
Julia M. Phillips
David R. Sandison
Jerry A. Simmons

Production
Katelynn G. Florentino
Clare A. Stanopiewicz

Cover Page: **The figure depicts the result of a theoretical calculation of electrons moving through a high mobility two-dimensional (2D) electron layer with a superimposed 2D periodic (superlattice) potential, subject to an in-plane DC electric field. The height shows the number of electrons. The oscillatory behavior in time shows that electrons pass entirely through the Brillouin zone before scattering, hence executing a "back and forth" AC motion in real space, due to a simple DC field. This non-intuitive phenomenon, predicted by Felix Bloch in 1928, is referred to as a Bloch oscillation. See the brief by S.K. Lyo on p. 62**

Message from the Director

The Physical, Chemical, and Nano Sciences Center creates new scientific knowledge in support of Sandia's mission areas – nuclear weapons; energy, resources, and nonproliferation; defense systems and assessments; and homeland security and defense. We provide science-based solutions in support of Sandia's broad national security mission. We also perform focused long-term research in areas likely to have impact on future Sandia missions and national security, particularly in the physical, chemical, and nano sciences. This volume highlights representative research in our areas of emphasis, including Science for Sandia's National Security Mission [including the Qualification Alternatives to the Sandia Pulsed Reactor (QASPR) Program]; GaN and Related Materials; Nanoscience and Nanotechnology; and a sampling of some of our most fundamental scientific studies.

The activities of the Physical, Chemical, and Nano Sciences Center are supported by a diverse set of funding sources reflecting the broad impact of our work, both scientifically and programmatically. The research described in this volume illustrates the importance of a strong science base in the physical, chemical, and nano sciences for the success of the Department of Energy's missions and Sandia's broader mission in national security. In this work, we have benefited immeasurably from our partnerships with colleagues across the labs, in universities, and in industry. We gratefully acknowledge their collaboration.

We appreciate your interest in our work and welcome your comments and inquiries.

Julia M. Phillips
Director

Table of Contents

Qualification Alternatives to the Sandia Pulsed Reactor (QASPR)

The Science of QASPR (Qualification Alternatives to the Sandia Pulsed Reactor) in Sandia's Physical, Chemical, and Nano Sciences Center (PCNSC) (S.M. Myers and W.R. Wampler) 6

Model of Defect Evolution and Carrier Reactions in a Neutron Recoil Cascade and Comparison with Experiment (S.M. Myers) 8

Inverse Gain Comparison between Experimental and Simulation Results for Ion Beam Irradiations in Silicon Bipolar Junction Transistors (E. Bielejec, G. Vizkelethy, D.B. King, W.R. Wampler, and S.M.Myers) 10

Effects of Neutron Damage on Photocurrent in Silicon Bipolar Junction Transistors (W.R. Wampler) 12

Measuring Defects in Silicon Damage Cascades (R.M. Fleming) 14

Physical, Chemical, and Nano Sciences for National Security

Ion-Imaging Plasma Diagnostics (E.V. Barnat and P.A. Miller) 18

Rapid Time to Fire Nd: Cr: GSGG Lasers (M.V. Pack and P.A. Miller) 20

Ion Luminescence of Multi-Quantum Well Structures (J.V Branson, G. Vizkelethy, B.L. Doyle, D.D. Koleske, P. Rossi, P.L. Gourley, and J.A. Knapp) 22

Thermal Tests of Target Materials in Gamma-tubes for Active Interrogation (P.P. Provencio, F.D. McDaniel, A.J. Antolak, B.L. Doyle, and D.H. Morse) 24

Depolarization Measurements of Biological Aerosols for Standoff Detection (R.L. Schmitt, S.M. Sickafoose, M.S. Johnson, and P.J. Hargis, Jr.) 26

GaN and Related Materials

Mg Doping of AlGaN Alloys for Optoelectronic Devices (A.A. Allerman, M.H. Crawford, and A.M. Armstrong) 30

Indium-induced step transformation during InGaN quantum-well Growth on GaN (D.D Koleske, S.R. Lee, G. Thaler, M.H. Crawford, M.E. Coltrin, and K.C. Cross) 32

Surface Plasmon Enhanced Emission from InGaN LEDs (A.J. Fischer, D.D. Koleske, K.W. Fullmer, A.J. Coley, and J.R. Wendt) 34

Observations of Gas-Phase Nanoparticles During InGaN MOCVD (J.R. Creighton, M.E. Coltrin, and J.J. Figiel) 36

Deep Level Optical Spectroscopy of GaN Nanowires (A.M. Armstrong, G.T. Wang, Q. Li, and A.A. Talin) 38

Table of Contents Cont'd

Nanoscience and Nanotechnology

Extreme Response Field-Structured Chemiresistors for Chemical Switch Arrays (D.H. Read and J.E. Martin) 42

Integrated Contamination Layers for Corrosion Sensors (N. Missert, J. Rivera, and R.G. Copeland) 44

High Refractive Index TiO_2 Nanoparticle/Silicone Composites (T.C. Monson and D.L. Huber) 46

Expitaxial Diamond Growth on Ir(100) Surfaces (T.A. Friedmann, J.P. Sullivan, E.S. Piekos, and S.L. Shinde) 48

Microstructural Origins of Saccharine Induced Stress Reduction in Electrodeposited Ni (S.J. Hearne) 50

Large Enhancements of Magnetic Anisotropy in Oxide-Free Iron Nanoparticles (D.L. Huber, T.C. Monson, J.M. Lavin) 52

Measuring Diode Characteristics of Individual Semiconductor Nanowires (B.S. Swartzentruber, A.A. Talin, F. Leonard, S.T. Picraux) 54

Elucidating Acid-base Behavior of Silica with *ab initio* Molecular Dynamics (K. Leung, I.M.B. Nielsen, and L.J. Criscenti) 56

Fundamental Studies

Dynamics of Entangled Polymer Melts: A Perspective from 20 Years of Molecular Dynamics Simulations (G.S. Grest) 60

Scattering in Bloch Oscillations in a One-Dimensional Quantum Dot Superlattice (S.K. Lyo) 62

Coulomb Drag of Electron-Hole Bilayers in the Exciton Regime (M.P. Lilly, J.A. Seamons, C.P. Morath, and J.L. Reno) 64

Active Control of Surface Plasmons (E.A. Shaner and J.G. Cederberg) 66

Recent Awards & Prizes 70

Government Advisory Boards & Professional Societies 74

Resource & Capabilities 80

Physical, Chemical, and Nano Sciences Center FY08 Budget 87

Acronym Glossary 89

Qualification Alternatives to the Sandia Pulsed Reactor (QASPR)

The Science of QASPR (Qualification Alternatives to the Sandia Pulsed Reactor) in Sandia's Physical, Chemical, and Nano Sciences Center (PCNSC)

by S. M. Myers

Motivation—The QASPR program is developing means to certify electronic systems for intense bursts of MeV neutrons without the Sandia Pulsed Reactor (SPR), decommissioned in Sept. 2006. Testing in available irradiation facilities will be combined with new, science-based modeling to predict time-dependent device and circuit performance under inaccessible conditions. A central concern is carrier recombination at neutron damage in Si bipolar-junction transistors (BJTs). Gains may be reduced from > 100 to < 1, and rapid damage evolution causes this reduction to vary greatly over times from microseconds to seconds.

The PCNSC has two key roles in QASPR. Our theoretical and experimental studies to characterize the fundamental, interrelated behaviors of defects and carriers – and to devise new methods for their mathematical representation – enable the modeling of devices. Further, research in the Ion Beam Laboratory (IBL) is establishing pulsed ion irradiation as a tool for assessing the transient response of devices to displacement damage.

Accomplishment—IBL is among the primary irradiation facilities to be used in QASPR qualification procedures. Ed Bielejec and George Vizkelethy are developing experimental capabilities to provide ever more intense and better quantified pulses in the μs range. Simultaneously, they are researching the similarities and differences of neutron and ion-beam effects. They have recently focused on the time dependence of gain reductions under ion bombardment and its consistency with results from neutron irradiation and from modeling, as discussed in these Briefs.

I previously developed the code Cluster to describe the time evolution of defects and their carrier reactions in a recoil cascade produced by one neutron collision. With Bill Wampler, I validated this model by comparing its results with electrical and Deep Level Transient Spectroscopy (DLTS) measurements under neutron and electron irradiations where results reflected a single local condition (in contrast to the multiple disparate regions of a BJT). Favorable results, described in the present Briefs, led me to write a new transistor model, 1DC, incorporating multiple instances of Cluster and running parallel on a large machine.

Photocurrents due to gamma ionization and carrier recombination at neutron damage were long considered separately, neglecting the large reduction of photocurrent by the recombination. Bill Wampler has now used our device model 1D to quantitatively describe the combined effects for SPR, as described in these Briefs.

Robert Fleming is successfully extending DLTS to the doubly challenging problem of clustered neutron damage within an actual transistor instead of an idealized structure, as discussed in these Briefs. His characterization and counting of defects is providing unique guidance for the device modeling as well as new fundamental understanding of the defect physics.

QASPR modeling depends critically upon the theoretical calculations of Normand Modine and Alan Wright, who are using density-functional theory (DFT) to obtain defect properties inaccessible to experiment. For example, the bandgap levels and diffusion coefficients of the Si interstitial are taken entirely from DFT, (S. M. Myers, P. J. Cooper, and W. R. Wampler, J. Appl. Phys. *104*, 044507 (2008).

Significance—Work within the PCNSC enabled the success of the Simple Prototype device exercise, the most important milestone of QASPR to date. See Fig.1 .

Sponsors for various phases of this work include: Nuclear Weapons Program: Nuclear Survivability, Advanced Simulation & Computing, Enhanced Surety, and Enhanced Surveillance Campaigns

Contact: Sam M. Myers; Rad, Nano & Interface Sciences, Dept. 1110
Phone: (505) 844-6076, Fax: (505) 844-7775, Email: smmyers@sandia.gov

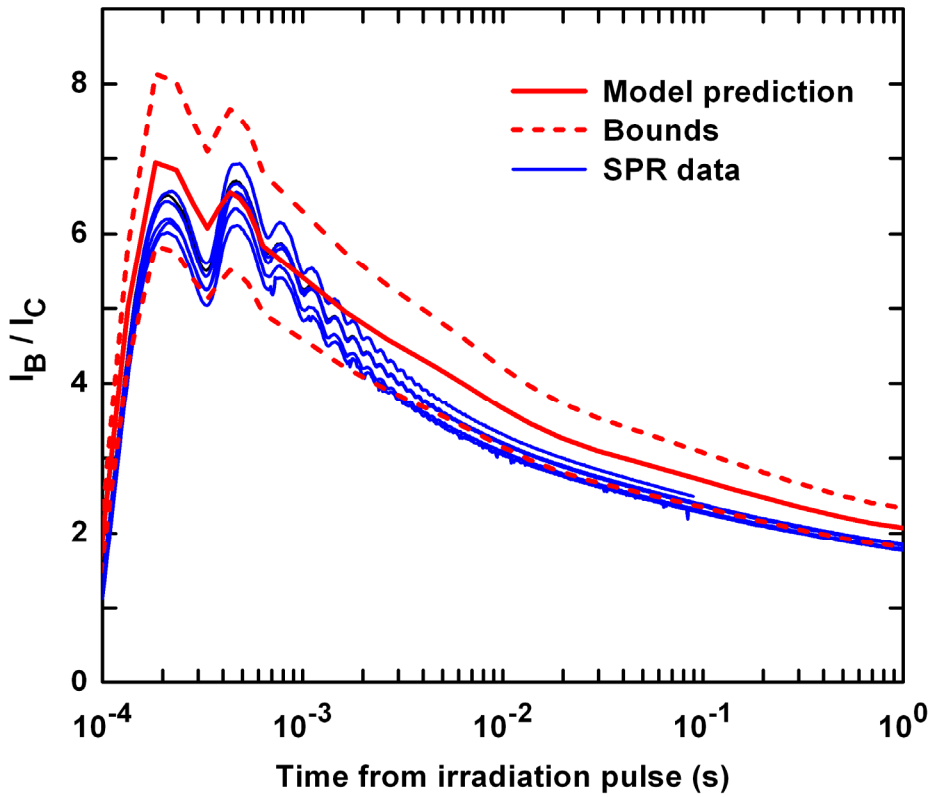

Figure 1. Results from the Simple Prototype device exercise: blind predictions of the test-calibrated model show impressive agreement with experimental results for the inverse gain of a Fairchild 2N2222 npn BJT exposed to a maximum SPR pulse. These exploratory calculations by Bill Wampler, using the physics-development code 1D from 1100, served to prototype the formal Simple Prototype exercise that was subsequently carried out with the ASC code Charon, developed in the Computer and Information Sciences Center. The downward excursion and oscillations at small times are due to photocurrents arising from gammas, an effect included in the modeling. (The SPR reactor experienced minor mechanical instabilities during pulse termination, producing variations in output that led to the observed oscillations.) It is noteworthy that the variation of inverse gain with damage level is increasingly faster than linear as the inverse gain rises above 1, making the test more challenging.

Model of Defect Evolution and Carrier Reactions in a Neutron Recoil Cascade and Comparison with Experiment

by S. M. Myers and W. R. Wampler

Motivation—Atomic displacements produced in Si by impinging MeV neutrons are not randomly dispersed, instead being localized in damage cascades caused by the primary Si recoils from the relatively infrequent neutron collisions. Such clustering can have substantial effects both on the time evolution of the defects and, as a result of local electrostatic fields, on the interactions of carriers with the defects. Quantitative modeling of transient neutron effects on transistor performance requires understanding of the nature and magnitude of these phenomena. For several decades prior to QASPR, there were debates and rough estimates but no detailed modeling.

Accomplishment—We previously developed the code Cluster to treat the transport and reactions of defects and carriers (39 species including multiple charge states) within a single, radially symmetric recoil cascade. In these calculations, the starting radial profiles of the primal vacancies and Si interstitials are obtained by correlation-function analysis of defect maps from binary-collision and molecular-dynamics simulations of the cascade-forming collisions. In 1st-generation modeling of transistors for QASPR, the device codes have assumed randomly dispersed defects and made only rudimentary use of the predictions of Cluster, e.g., reducing the starting concentrations of primal defects to account for rapid vacancy-interstitial recombination within the core of a cluster.

We progressed from this beginning in two stages. First, the fidelity of Cluster was assessed by comparing its predictions to experimental results. We restricted these comparisons to cases where the measured properties arise predominantly from a single local condition, allowing them to be predicted on the basis of one Cluster calculation. This requirement is not satisfied by the electrical properties of a bipolar transistor, whose behavior reflects the combined influences of multiple disparate regions. Instead, we employed published minority-carrier lifetimes in neutron- and electron-irradiated solar cells and bulk Si, along with defect densities and defect-charging kinetics observed by Robert Fleming in his Deep Level Transient Spectroscopy (DLTS) studies under QASPR. Generally good agreement was obtained without adjustment of model parameters. Figure 1 shows the time dependence of the annealing factor (AF), related to the minority-carrier lifetime τ by

$$\mathrm{AF} = \frac{\tau^{-1}(\mathrm{t}) - \tau^{-1}(\text{pre rad})}{\tau^{-1}(\text{long time}) - \tau^{-1}(\text{pre rad})} ,$$

for n- and p-type solar cells at various levels of carrier injection following pulsed neutron irradiation. The model calculations capture both the forms of the transients and their variations with doping and carrier injection.

In view of this success, we proceeded to develop the transistor model 1DC, which incorporates multiple (typically 40) instances of Cluster to treat the varying local concentrations of carriers, dopants, and impurities. Evaluation of the utility of 1DC for QASPR purposes is underway.

Significance—The code 1DC may provide the basis for more accurate, 2nd-generation modeling of transistors and other bipolar Si devices in the QASPR program.

Sponsors for various phases of this work include: Nuclear Weapons Program: Nuclear Survivability, Advanced Simulation & Computing, Enhanced Surety, and Enhanced Surveillance Campaigns

Contact: Sam M. Myers, Rad, Nano & Interface Sciences, Dept. 1110
Phone (505) 844-6076, Fax (505) 844-7775, Email: smmyers@sandia.gov

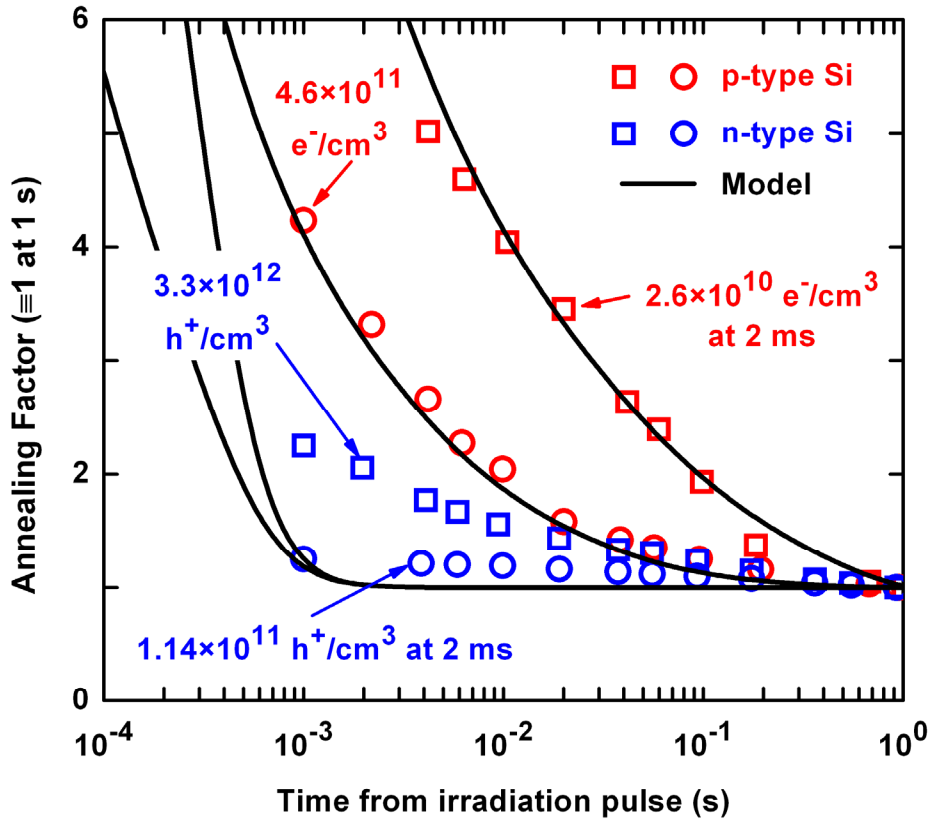

Figure 1. Time-dependent annealing factor for solar cells after pulsed-neutron irradiation in SPR, from the Cluster model [1] and from experiment [2]. The elevated minority-carrier concentrations resulting from constant injection are indicated for the specific time of 2 ms, since these concentrations vary with time as the damage responsible for recombination undergoes annealing.

[1] S. M. Myers, P. J. Cooper, and W. R. Wampler, J. Appl. Phys. **104**, 044507 (2008).

[2] B. L. Gregory and H. H. Sander, IEEE Trans. Nucl. Sci. **NS-14**, 116 (Dec. 1967).

Inverse Gain Comparison between Experimental and Simulation Results for Ion Beam Irradiations in Silicon Bipolar Junction Transistors

by E. Bielejec, G. Vizkelethy, D. B. King, W. R. Wampler and S. M. Myers

Motivation—Late-time damage equivalence between the alternative facilities of the QASPR program makes use of the Messenger-Spratt damage factor to provide a comparison metric across the facilities. There are, however, many instances where we are interested in the transient behavior of the device on short time scales after the irradiation. For this early-time behavior we compare the inverse gain degradation across facilities, as defined by equation (1),

$$\Delta(1/G) = 1/G(t) - 1/G_0 \qquad (1)$$

where $G(t)$ is the time dependent gain measured during and after the irradiation and G_0 is the pre-irradiation gain. It is in this early-time regime that the ion beam irradiations are of particular importance. While no one alternative facility can replicate fast burst reactor testing (high neutron flux, short pulse width and uniform test volume) the combination of modeling and experimental results will allow parameter space exploration. As summarized in Table 1, comparison of the QASPR fluence values (in 1 MeV neutron equivalent fluence) and pulse lengths for the QASPR relevant facilities, testing in the Ion Beam Laboratory (IBL) will achieve the desired damage creation rates.

Accomplishment—We have previously demonstrated the ability to use the Messenger-Spratt damage factor as a means of late-time comparison across the QASPR relevant facilities and as a method of rescaling of the ion fluence to an effective 1 MeV equivalent neutron fluence. Furthermore, we have demonstrated the ability to match the temporal profile and the damage creation rate of SPR-III irradiations using Si ions in the IBL. Here we turn our attention to a comparison between experimental and simulation results for ion beam irradiations.

Figure 1 compares experimental and simulation results for a series of 4.5 MeV Si irradiations, spanning the critical QASPR fluence values. The simulation results are based on an atomistic model for the static and dynamic changes in gain of a silicon bipolar transistor due to energetic particle irradiation. The model is calibrated to SPR fast neutron data by adjusting the values of the carrier cross-sections within independent experimentally determined bounds. This provides a physics-based approach to simulate these effects and the resulting transient changes in transistor gain. We observe excellent agreement between the time-dependent shape and fluence dependence of the gain response (Figure 1). Similar results were found for the comparison between 36 MeV Si irradiation and simulation. The systematic offset between the simulation and experimental results is of great interest, as it indicates either an error in the measured ion or neutron fluence or a fundamental issue in the simulated defect creation rates for ion or neutron irradiations.

Significance—We have shown excellent agreement between the experimental results and 1D simulation for the shape and fluence dependence of inverse gain. The systemic offset on the order of 2x is an excellent result given the complexity of the calculations from incident ion fluence to the initial configuration of interstitials and vacancies after irradiation.

Sponsors for various phases of this work include: Nuclear Weapons Program: Nuclear Survivability Campaign

Contact: Edward S. Bielejec, Radiation-Solid Interactions, Dept. 1111
Phone: (505) 284-9256, Fax: (505) 844-7775, Email: esbiele@sandia.gov

Facility	QASPR Fluence	QASPR Pulse Length
SPR-III	~4E14 n/cm^2	~100 µs
IBL (Si EOR 4.5 MeV)	~4E14 n/cm^2	~10 µs
ACRR	~4E14 n/cm^2	~30 ms
IBL (Si Uniform 36 MeV)	~1E14 n/cm^2	~100 µs
WSMR FBR	~1E13 n/cm^2	~50 µs
LANSCE	~2E12 n/cm^2	~150 ns

Table 1. QASPR alterative facilities with QASPR relevant fluence levels (in 1 MeV equivalent neutron fluence) and pulse lengths. The Si End-of-Range (EOR), i.e., 4.5 MeV, corresponds to energies targeting the base-emitter (BE) junction directly, while Si Uniform refers to high energy Si irradiations, i.e., 36 MeV, that produce uniform damage levels throughout the emitter and base diffusion.

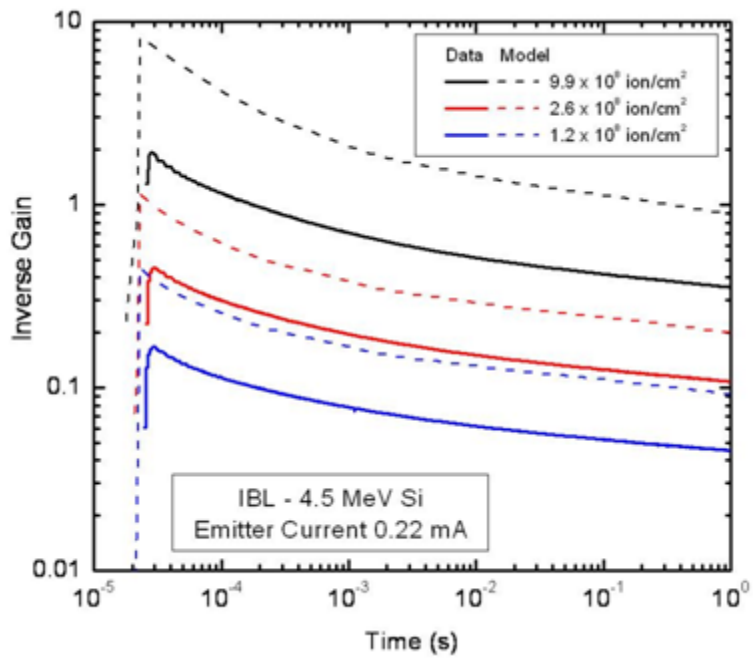

Figure 1. Inverse gain for both experiment and 1D simulations. There is excellent agreement in the shape and fluence dependence. The observed systematic offset (~ factor of two) is currently under investigation. This is an excellent result considering the computational chain for the calculation which starts with the number of interstitials and vacancies (IVs) produced from the initial irradiation (taking recombination and clustering effects into account) and then transports the initial IVs through higher order defect formation (VV, VP, etc..) and reactions which ultimately determine the final device performance. In addition, this calculation is complicated by the device geometry and nature of the ion beam irradiation.

Effects of Neutron Damage on Photocurrent in Silicon Bipolar Junction Transistors

by W.R. Wampler

Motivation—The goal of the QASPR project is to simulate the response of semiconductor devices to pulsed radiation. This includes effects of atomic displacements by energetic neutrons or ions and photocurrents from carrier generation by ionizing radiation. Previous simulations have treated damage and photocurrent separately. However, the two effects are interdependent because defects produced by atomic displacements increase carrier recombination, thereby reducing collected photocurrents. Furthermore, defect annealing depends on carrier concentrations which are increased by ionization. New models developed for QASPR now enable damage and photocurrent to be treated together for the first time.

Accomplishment—A one dimensional simulation was done of currents in a Microsemi 2N2222 npn silicon bipolar-junction transistors (BJT). This simulation includes production of vacancies and interstitials by atomic collisions with the energetic neutrons and carrier generation by ionization. The simulation also includes diffusion and reaction of the defects. Conditions were those of a Sandia Pulsed Reactor (SPR) cavity pulse, ionizing dose 10^4 kRad, peak dose rate 10^9 Rad/sec, neutron fluence 4.3×10^{14} /cm^2, constant emitter current = 0.22ma. The time dependence of dose rate and neutron flux in the simulation followed the photoconducting diode (pcd) signal, which is approximately proportional to ionizing dose rate. Because of the low doping and high reverse bias (10V) the depletion region of the base collector junction is much thicker than that of the emitter base junction, so most of the photocurrent comes from ionization in the collector. Therefore, in the 1D simulations the effective area for photocurrent was taken to be that of the base. Figure 1 shows that the photocurrent is much larger than the injected current and that the simulation (black solid curve) agrees well with results from several SPR shots (red curves). The blue curve shows that without displacement damage, the simulated photocurrent is significantly higher than the test results. This difference results largely from increased recombination in the neutral region of the collector rather than in the depletion region. Figure 2 shows the carrier concentrations are increased by the ionization. The simulations show that the reason the effect of damage on photocurrent is modest in this device, is because recombination by the Auger process in the highly doped sub-collector (2×10^{19}/cm^3) gives a short lifetime (10 nsec) and carrier diffusion length (~2 microns) which is smaller than the collector depletion thickness (~6 microns) already in the undamaged material. The photocurrent prior to damage is therefore predicted to be greater, and the reduction from displacement damage greater, in more lightly doped devices.

Significance—These simulations demonstrate the coupled effects of damage and photocurrent in semiconductor devices. The comparison with SPR data provides a validation that the model closely reproduces the photocurrent observed in Microsemi 2N2222 BJTs, with no adjustable parameters.

Sponsors for various phases of this work include: Nuclear Weapons Program: Nuclear Survivability, Advanced Simulation & Computing, Enhanced Surety, and Enhanced Surveillance Campaigns

Contact: W.R. Wampler, Radiation-Solid Interactions, Dept. 1111
Phone: (505) 844-4114, Fax: (505) 844-7775, Email: wrwampl@sandia.gov

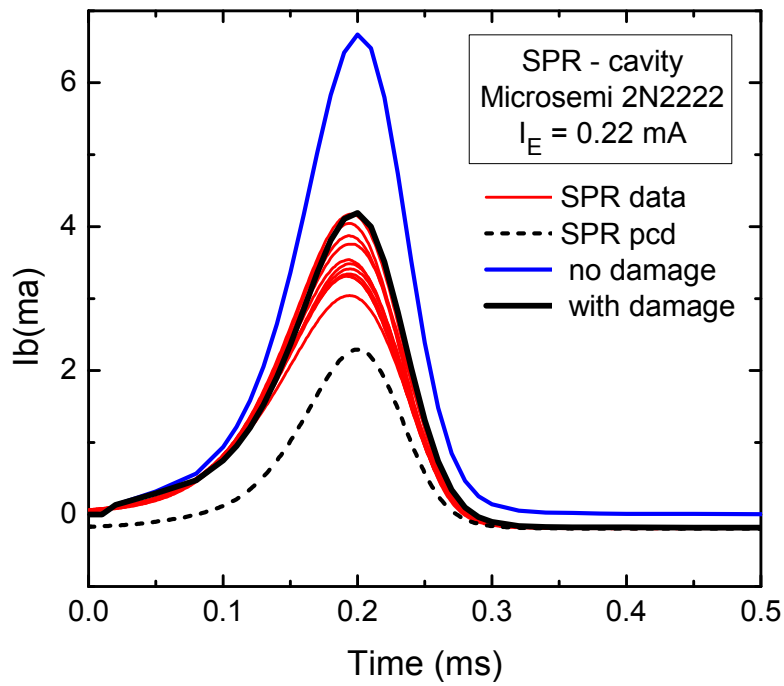

Figure 1. Comparison between measured and simulated photocurrent peak in the base current of Microsemi 2N2222 npn transistors from a SPR pulse. Red curves show measured response. The black and blue solid curves show simulated response with and without displacement damage, and the black dashed curve shows the photoconducting diode response which is proportional to the ionizing dose rate. The origin of the time scale is 0.2 millisecond before the peak of the pcd signal.

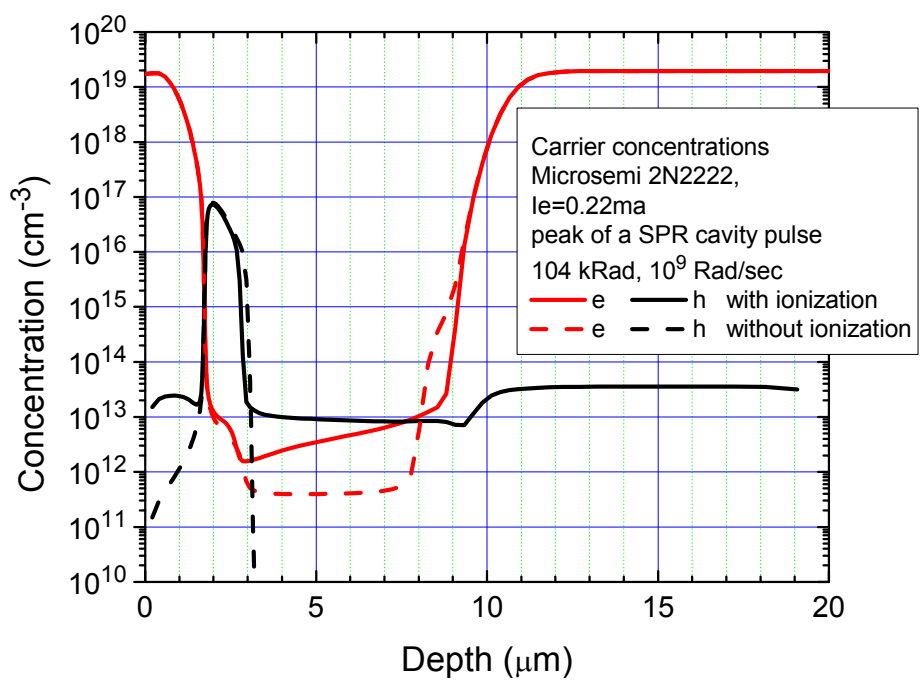

Figure 2. Carrier concentrations before the pulse (dashed) and at the peak of a SPR pulse (solid). The junctions are at 1.7 microns (emitter-base) and 3.8 microns (base-collector).

Measuring Defects in Silicon Damage Cascades

by R. M. Fleming

Motivation—The QASPR program seeks to predict the performance of silicon transistors following fast neutron irradiation we must first measure the device response following an alternative radiation such as heavy ions. Data from the alternate sources provide input to models that predict the response of the device to fast neutrons. Atomistic inputs to the models are based both on physical information about defects from the literature and from measurements of defects in a clustered-defect environment typical of neutron damage. The primary experimental source of atomistic information is deep level transient spectroscopy (DLTS). DLTS was originally developed to study modest damage from a uniform distribution of point defects. In this program we have needed to both extend the DLTS technique to include clustered damage characteristic of neutrons and to apply the technique to actual devices, here silicon bipolar transistors.

Accomplishment—Defects that are important in modeling radiation-induced gain reduction of a bipolar transistor are located near the emitter-base junction. Two important defects have been identified; the vacancy-phosphorus (VP) and the divacancy (V_2), and both defects can be seen in DLTS of n-type silicon. Deconvolution of these two defects from DLTS spectra in the base is difficult because of overlap of the VP and V_2 signals. We have been able to attack this problem by analysis of DLTS spectra from the collector. The number of VP defects in the collector is much smaller, allowing one to study the behavior of the V_2 in neutron damage cascades.

Using careful studies of the annealing of V_2 in the collector following neutron irradiation, we have found at least three types of V_2 defects. These are: (1) normal V_2 defects also seen in the case of uniform damage (2) strained V_2 defects located within a damage cascade and (3) bistable V_2 defects also located within the cascade.[1,2] The bistable V_2 is only seen if one first injects minority carriers at room temperature.

Two fortuitous properties of the bistable V_2 allow us to use it to deconvolve the VP and V_2 signals in the base. First, the positions of the two bistable V_2 peaks are sufficiently shifted to allow easy measurement and second, we have shown in the collector that one can predict the normal plus strained V_2 DLTS by a simple scaling of the bistable V_2 signal. Measurements of the bistable V_2 in the base thus allow us to determine the annealing behavior of the V_2 which is obscured by the VP defect. We subtract a scaled bistable V_2 signal (representing the normal plus strained V_2) from the total signal, and this allows us to deduce the fraction of deep defects that are comprised of VP.

Significance—Our results provide critical information and are part of the validation of the QASPR models. In the case of silicon devices, DLTS data are the only source of independent experimental data from actual devices in a neutron environment. We have also shown that one can extend DLTS, a technique designed to examine dilute impurities, in a clustered environment characteristic of neutron damage.

[1] R. M. Fleming, C. H. Seager, D. V. Lang et al., Appl. Phys. Lett. *90*, 172105 (2007).
[2] R. M. Fleming, C. H. Seager, D. V. Lang et al., J. Appl. Phys, in press (2008).

Sponsors for various phases of this work include: Nuclear Weapons Program: Nuclear Survivability Campaign
Contact: Robert M. Fleming, Semiconductor Materials and Device Sciences, Dept. 1123
Phone: (505) 284-8460, Fax: (505) 844-1197, Email: rmflemi@sandia.gov

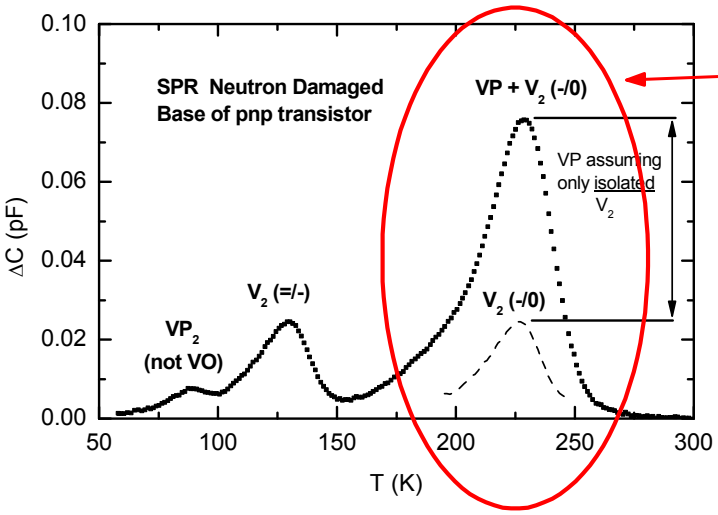

Problem: DLTS of the transistor base contains at least two defects that degrade gain, VP and V2, and both have the same emission energy.

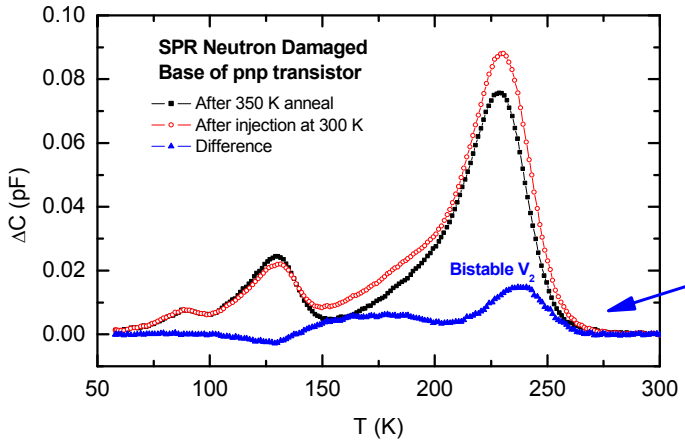

Solution: Use the bistable V_2 obtained by minority carrier injection to estimate the amount of normal plus strained V_2 in the transistor base.

Measurement and scaling of the bistable V_2 allows one to determine amount of normal + strained V_2 and consequently the amount of VP.

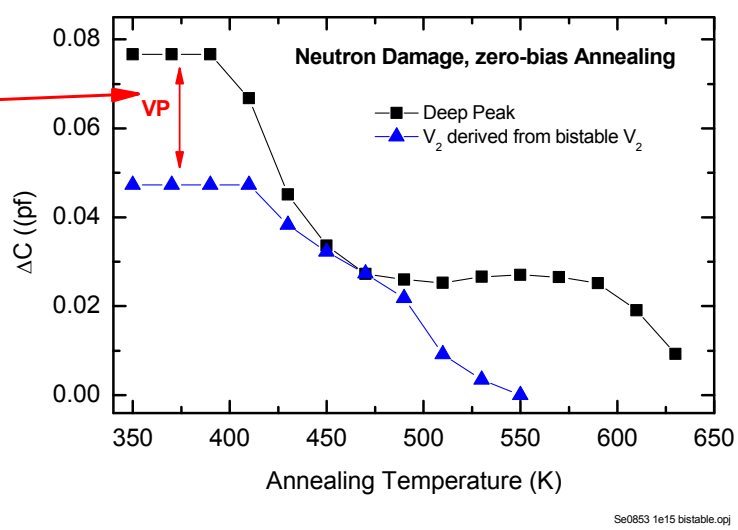

Physical, Chemical and Nano Sciences for National Security

Ion-Imaging Plasma Diagnostics

by E. V. Barnat and P. A. Miller

Motivation—Sandia is developing a 3-D unstructured-mesh plasma code which will provide unprecedented capabilities for modeling plasma and charged-particle flows. This will greatly improve Sandia's computational capabilities for design and manufacturing of critical components that employ plasma for ion generation. In parallel with this code work, we are developing novel plasma diagnostic techniques and conducting experimental tests for code validation. The diagnostics and tests are designed to isolate key pieces of plasma physics that the code must be able to treat accurately for eventual success.

Accomplishment—A plasma "sheath" is a region in which plasma properties change abruptly with spatial position. Plasma sheaths have been studied for decades, and their properties under different plasma conditions continue to be scientifically interesting and computationally challenging. The initial focus of our experimental studies is the extraction of an ion beam from quasi-neutral plasma. This effort tests the ability of the code to treat flowing, field-free plasma, its interaction with surfaces, and the transition in a sheath from plasma to a high-electric-field region in which an ion beam forms.

Advanced diagnostic capabilities have been developed to examine the interaction between flowing plasma and a structured electrode. Both the concept and realization of the diagnostic technique are illustrated in Figure 1. Ions are extracted from plasma generated by a vacuum arc ion source. The accelerated ions impact a meshed electrode, which in turn generate 'secondary' electrons. These electrons are then accelerated towards a fast responding phosphor screen (P47, with ~ 50 ns decay time). Spatial distribution of the photons generated by the electron beam is imaged using a gated, intensified CCD (ICCD) camera. Time evolution of the ion beam is obtained by scanning the gated ICCD over the period of plasma generation.

Representative images formed by ion flow through three structured electrodes, for three accelerating voltages are illustrated in Figure 2. The different structured electrodes demonstrate a transition from symmetric (round hole) to more complex (plus shaped hole) geometry. Accelerating potentials are varied from low voltage, where the plasma pushes through the hole to high voltage where the accelerating fields penetrate into the plasma. The resulting distribution of ions is observed to clearly depend on the coupling of the plasma to the applied electric fields. The 3-D predictive capabilities of the plasma code are being tested by measurements like these presented here.

Significance—Diagnostic techniques that we developed are being used for validation of Sandia's new plasma code. We are comparing the observed and predicted dynamics of ion beam formation and propagation through structured electrodes. Through this iterative procedure, we can understand the interaction between the species generated in the plasma and the structured electrodes that the plasma flows through. These measurements address sensitive and critical physics that will need to be implemented into the code. Successful validation will give confidence in use of the developed code towards aide in design and manufacturing.

Sponsors for various phases of this work include: Nuclear Weapons Program

Contact: Paul Miller, Lasers, Optics, & Remote Sensing, Dept. 1126
Phone: (505) 844-8879, Fax: (505) 844-5459, Email: pamille@sandia.gov

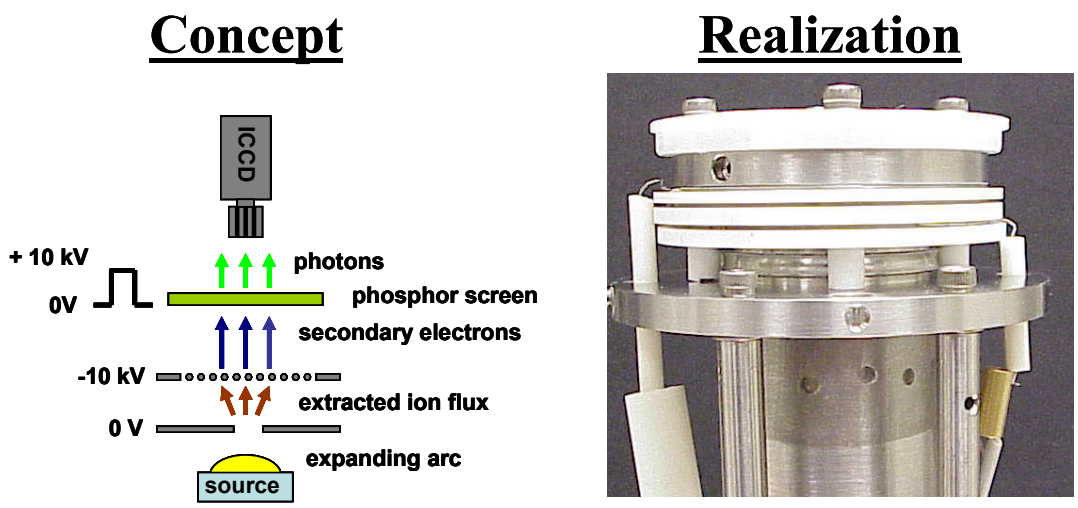

Figure 1. Concept and realization of ion imaging diagnostic used to study ion flow from plasma through structured electrodes.

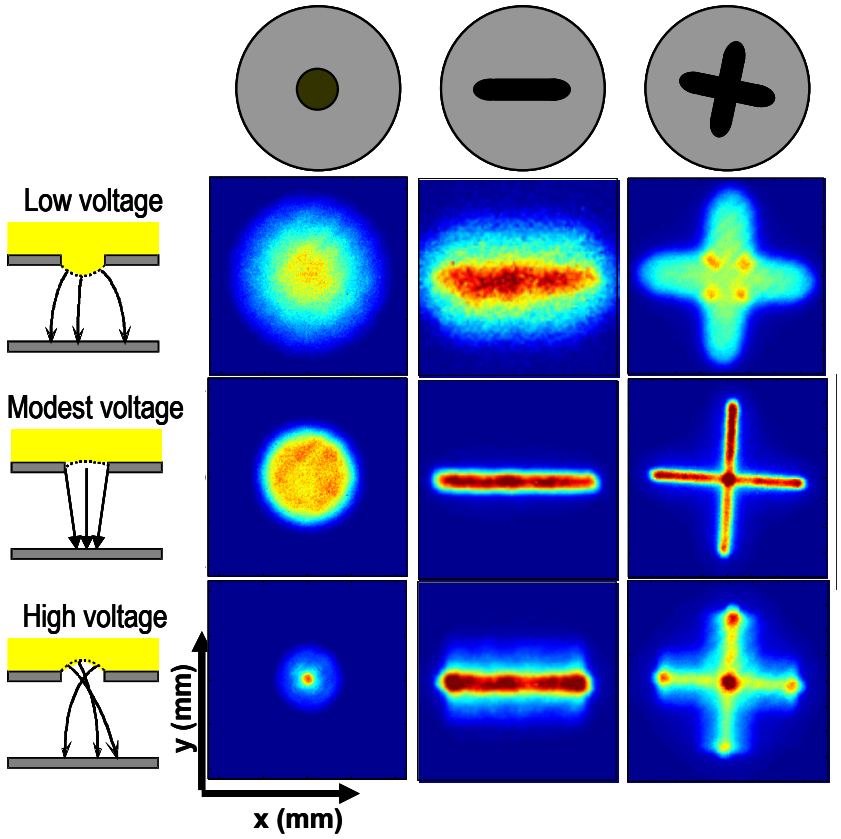

Figure 2. Representative images of the ion beam obtained with ion imaging diagnostic for various structured electrodes (illustrated above each column) and accelerating voltages (illustrated to the left of each row).

Rapid Time to Fire Nd:Cr:GSGG Lasers

by M. V. Pack and P. A. Miller

Motivation—It is well known that laser rods made of gadolinium scandium gallium garnet (GSGG) doped with neodymium and chromium are radiation hard, which is important for laser applications in high radiation environments. One open question surrounding Nd:Cr:GSGG Q-switched lasers is how quickly the laser can be fired after it is triggered. If this firing time is too long, this laser technology will be inadequate for some weapons applications.

Accomplishment—It has been demonstrated that the discharge time of the flashlamps, which pump the Nd:Cr:GSGG laser into the excited state, can be decreased by multi-channel plasma formation in the flashlamps. In contrast to other methods, which also speed up the flashlamp discharge, multi-channel plasma formation should not increase the chance of catastrophic failure because it does not increase the peak current flowing through the flashlamp. By quickly discharging the flashlamp the laser medium becomes inverted more quickly, decreasing the time to fire.

A typical flashlamp will have a straight trigger wire running along the outside of the quartz tube to initiate the plasma formation, and the plasma will develop from a single channel which forms on the inside of the quartz tube right next to the trigger wire. As the plasma channel expands to fill the tube, the current increases until it peaks and the power in the capacitors drops. Using a spiral configuration, the trigger wire (see Fig. 1) initiates the plasma formation along multiple channels allowing the plasma to expand and fill the tube more quickly. We found that the flashlamp optical emission reached its peak value 25% faster for a spiral trigger wire than for a straight trigger wire under fast firing conditions. We have also developed models for the inversion dynamics in Nd:Cr:GSGG in order to predict gain power as a function of time given different flashlamp dynamics and spectral characteristics. The inversion dynamics of Nd:Cr:GSGG are more complicated than more common lasers such as Nd:YAG. In Nd:YAG when a flashlamp photon is absorbed by a neodymium ion, the ion almost instantaneously decays into the lasing excited state where it has a lifetime of about 250 µs. Nd:Cr:GSGG lasers are more efficient than Nd:YAG because the chromium ions, which have different absorption resonances than the neodymium ions, absorb flashlamp photons and nonradiatively transfer their excitation to the neodymium ions with an average transfer time of 17 µs. Figure 2 compares fluorescence at 1064 nm from Nd:YAG and Nd:Cr:GSGG laser rods which are pumped by a flashlamp that has been frequency filtered. It is evident that Nd:Cr:GSGG is better at converting flashlamp light of all wavelengths to inversion and fluorescence, but at those wavelengths where the chromium ions contribute significantly to the inversion process the inversion rise time is much longer. By curve fitting similar measurements with 50 nm spectral filters for the flashlamp light we have developed models for the inversion dynamics of Nd:Cr:GSGG as a function of pumping wavelength

Significance—By decreasing the flashlamp firing time without sacrificing flashlamp lifetime, and by modeling the dynamics of the inversion processes in Nd:Cr:GSGG, we can improve the ability of radiation hard lasers to operate in rapid time to fire applications.

Sponsors for various phases of this work include: Nuclear Weapons Program

Contact: Michael V. Pack, Lasers, Optics & Remote Sensing, Dept. 1128
Phone: (505) 844-8148, Fax: (505) 844-5459, Email: mvpack@sandia.gov

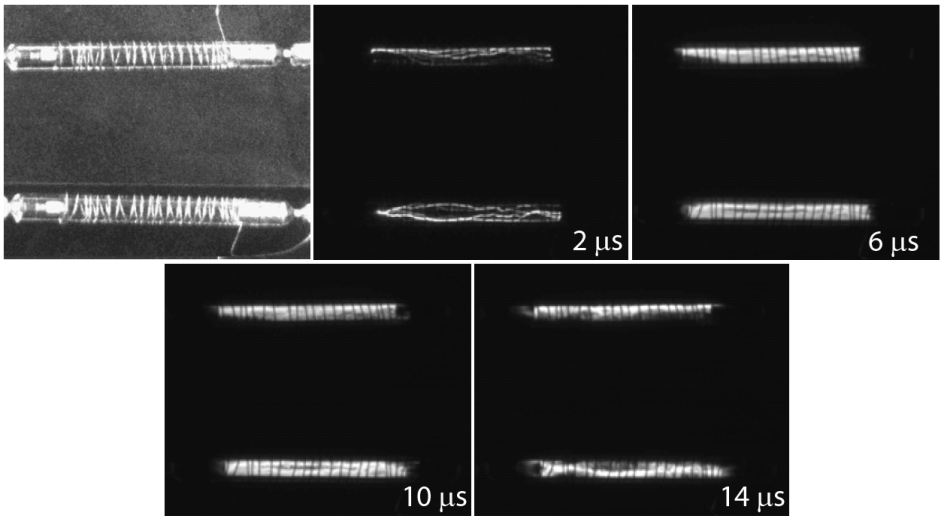

Figure 1. Framing-camera images of the plasma formation in a 1000-Torr flashlamp with a spiral trigger wire. The first image shows a long exposure time of the flashlamp before it is discharged. The remaining images show the plasma formation at times 2 µs, 6 µs, 10 µs, and 14 µs after the discharge is triggered. Different exposure times and amplifier gains were used to avoid saturating the individual images.

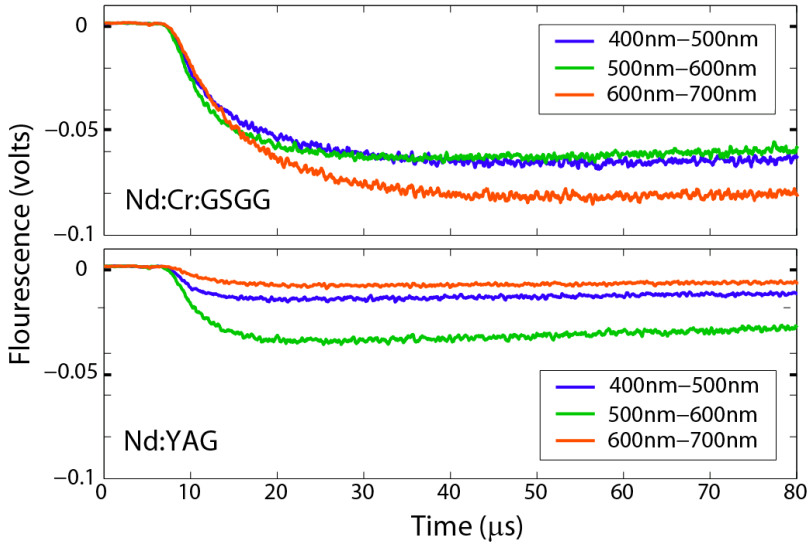

Figure 2. Measurements of 1064 nm fluorescence from Nd:Cr:GSGG and Nd:YAG laser rods. The same flashlamp light was used to pump both rods, and the pump light was wavelength filtered before the rods to select wavelength bands of 400nm to 500nm, 500nm to 600nm, and 600nm to 700nm.

Ion Luminescence of Multi-Quantum Well Structures

by J.V. Branson, G.Vizkelethy, B.L.Doyle, D. D. Koleske, P. Rossi, P.L. Gourley, and J.A. Knapp

Motivation—A new microscopy technique, ion-photon emission microscopy (IPEM), is crucial for analyzing failure and pinpointing radiation sensitive elements in today's complex integrated circuits. The technique requires a thin (<5 μm) self-supporting luminescent layer, demonstrating sufficient quantum efficiency when excited by ions, as well as rapid decay. InGaN/GaN multiple quantum well (MQW) structures grown by MOCVD on sapphire substrates are being studied as possible candidates due to their potential for producing high light intensity with short lifetimes. These materials have demonstrated two significant ion-luminescence peaks: the blue near-band edge emission and the defect-induced yellow band. These characteristic emissions exhibit very fast (nanoseconds) and very slow (hundreds of microseconds) lifetimes, respectively. Various quantum well structures are being studied to optimize the blue emission and reduce/eliminate the slow yellow emission.

Accomplishment—A series of InGaN/GaN MQW structures were grown at Sandia, with various composition, layer thicknesses, and layer ordering (see Figure 1). Ions have been utilized to analyze these materials, allowing us to characterize their luminescence properties, such as emission peaks and lifetimes of the various emissions. In addition to providing insight into how the materials will behave on an IPEM, ionoluminescence experiments offer several benefits over the more common photoluminescence (PL) and cathodoluminescence (CL) techniques. The large penetration depth of a MeV ion beam over the relatively shallow penetration of keV electrons (from CL) is a significant advantage, especially when studying multi-layer structures. The ability to vary the beam energy and see into different layers allows us to pinpoint the main sources of the two emission bands, and engineer the structures to better optimize the light output. As seen in Figure 2a, when using a higher energy proton beam, the relative intensity of the yellow band increases dramatically, demonstrating that the majority of this light originates from the defective buffer layers. In addition, we concluded that n-type GaN barrier layers are undesirable, as they produce more yellow light than intrinsic GaN. In Figure 2b, the advantage of using quantum wells is demonstrated, highlighting the decrease in luminescence decay time. This is crucial to IPEM experiments to avoid overlapping of detected photons from sequential ions, which would result in inaccurate position determinations and poor spatial resolution.

Significance—The future of heavy ion radiation effects microscopy depends on developing scanned microbeams and/or emission microscopes that can easily be used on cyclotrons. IPEM provides a reasonable solution, and its continuing progress is promising. GaN seems to be an ideal ionluminescent material for IPEM, with InGaN/GaN MQWs providing advantageous and unique properties. These materials create copious quantities of photons and are demonstrating fair resolution on an IPEM system. We expect further improvement with additional materials engineering. IPEM will allow us to extend radiation effects microscopy to increasingly thick integrated circuit (IC) overlayers.

Sponsors for various phases of this work include: Nuclear Weapons Program and Defense Threat Reduction Agency

Contact: Gyorgy Vizkelethy, Radiation-Solid Interactions, Dept. 1111
Phone: (505) 284-3120, Fax: (505) 844-7775, Email: gvizkel@sandia.gov

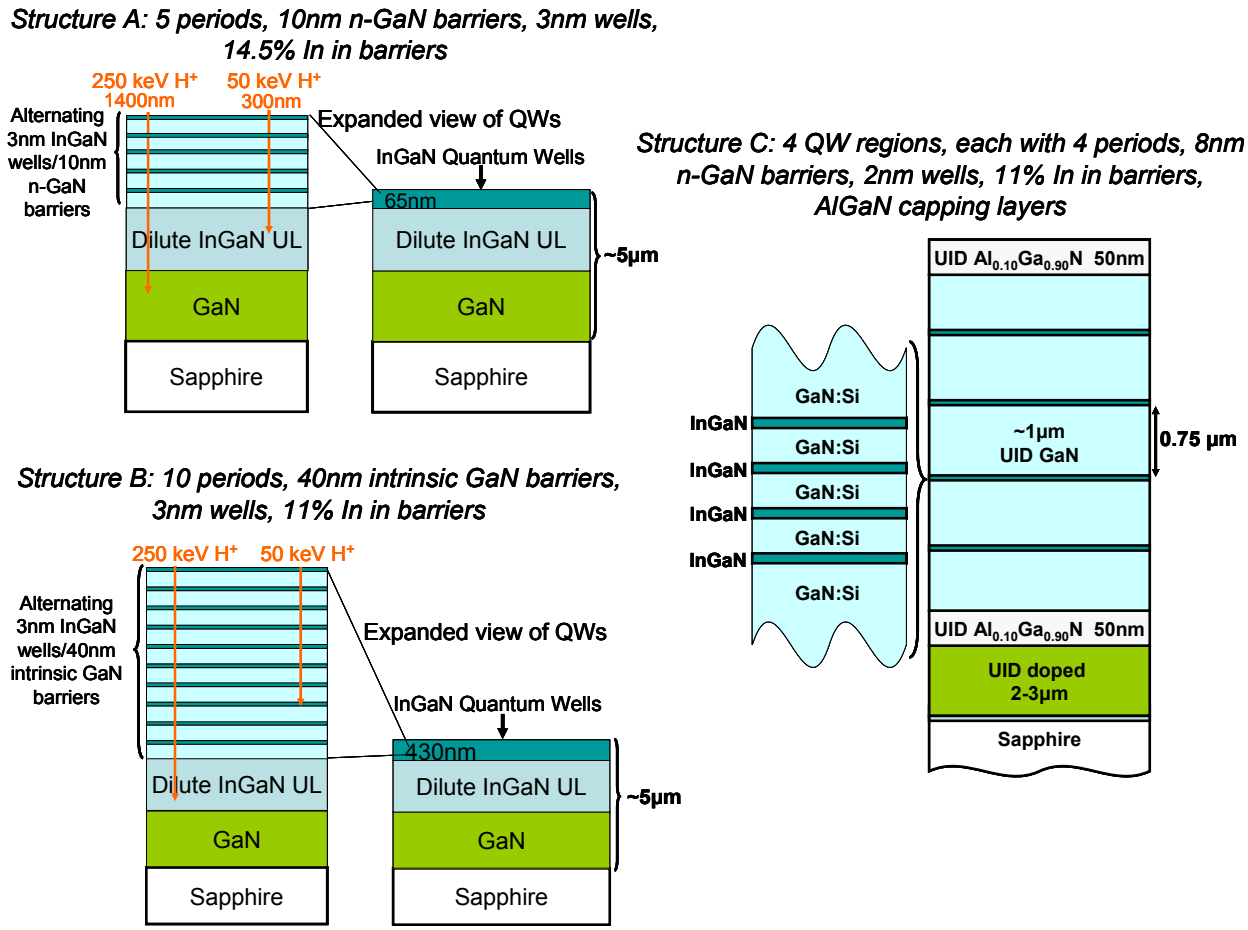

Figure 1. Various InGaN/GaN quantum well structures studied for their application in IPEM. Structure C is the most recent approach, utilizing AlGaN capping layers to limit the yellow emission.

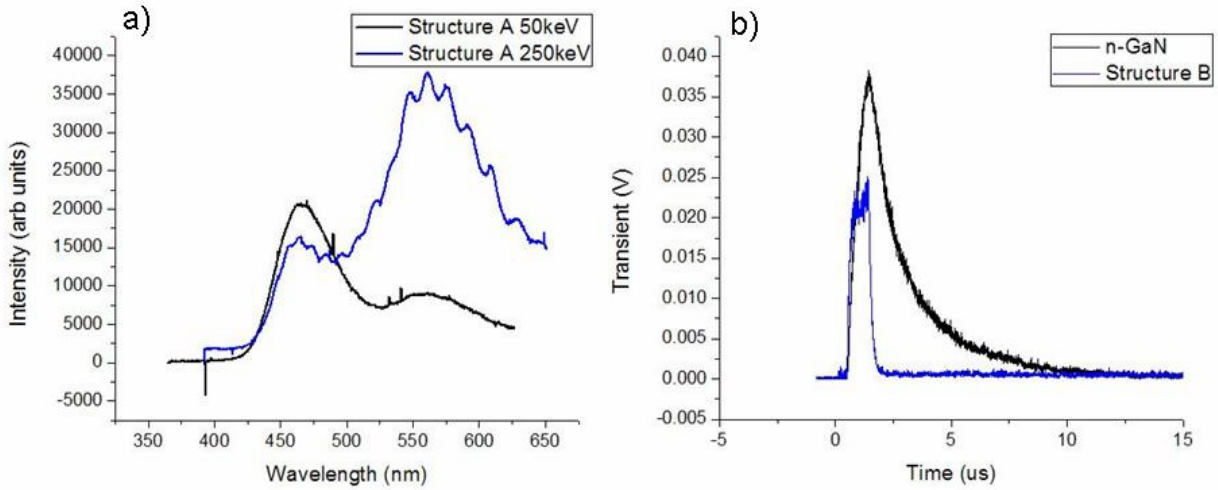

Figure 2. a) Ionoluminescence spectra of Structure A at different ion energies. b) Lifetime of ionoluminescence emission with a 1µs excitation pulse, demonstrating the advantage of using quantum wells over bulk n-type GaN. This shortened lifetime will improve the IPEM operation, limiting false coincidence signals, and thus allowing better resolution.

Thermal Tests of Target Materials in Gamma-tubes for Active Interrogation

by P.P. Provencio, F.D. McDaniel, A.J. Antolak, B.L. Doyle, D.H. Morse

Motivation—Active interrogation of nuclear materials involves probing an object with high-energy photons or neutrons and detecting the emitted fission neutron and gamma-ray signals. The source neutrons/photons are usually produced using large, high-energy accelerators such as radio frequency quadrupole or linear accelerators. However, the neutrons/photons can also be generated by much lower energy (p, γ) and (d, n) nuclear reactions (see Table 1), allowing for the development of much more compact and lower energy particle generators. Robust target materials for these low-energy sources need to be easy to fabricate, withstand the harsh radiation environment inside the source, and also have good thermal, electrical, and mechanical properties. We evaluated target materials for interrogation sources, by performing rapid thermal loading and high power density tests that reach conditions expected during source operation.

Accomplishment—Rapid thermal loading and high power density tests were performed on LiF, Li_2O, and CaF_2 films on Cu, and $LiNbO_3$, B_4C, and LaB_6 crystals. Following the tests, the targets were analyzed with scanning electron and cross-sectional microscopies to assess possible physical or structural damage. At 700°C, the CaF_2 film degenerated to a powder, and the LiF film became more crystalline. Elemental analysis during electron microscopy showed very little loss of fluorine. *In situ* X-Ray Diffraction (XRD), during 850°C heating in vacuum, showed Li metal formation at a temperature greater than 700°C. Elemental analysis showed that all F was lost. Li metal has a very low melting point of 180°C. LiF may be a candidate target for the $^{19}F(p,\alpha\gamma)^{16}O$ reaction at 340 kV, but only at or below a temperature of 700°C. The target would have to be cooled and the proton beam spot spread to reduce the power density and keep the operating temperature at or below 700°C. Furthermore, a buffer layer film over the Cu source substrate is necessary to eliminate reaction of F with the Cu. LiF is not recommended as a candidate for the the $^{7}Li(p,\gamma)$ reaction at 441 kV because the gammas produced from the $^{19}F(p,\alpha\gamma)^{16}O$ reaction at 340 kV would overwhelm it. Li_2O may be a good candidate if the target material is never exposed to air, but this may not be feasible. Microscopic examination of B_4C, and LaB_6 indicate these are possible target materials for the $^{11}B(p,\gamma)^{12}C$ reaction, if the beam could be spread to reduce the power density load.

Significance—Target source photons are usually produced using high-energy accelerators. However, with the use of low energy (p, γ) nuclear reaction resonances (See Table 1), compact gamma generators can be developed that produce high-energy mono-energetic gamma-rays [1,2]. Robust B-containing target materials can be found (e.g. B_4C, and LaB_6) that are easy to fabricate and can withstand the harsh beam heating and radiation environments inside the gamma generator. At this time, no robust F containing material has been found unless the operating temperature can be kept below 700°C.

Sponsors for various phases of this work include: Laboratory Directed Research & Development

Contact: Barney L. Doyle, Radiation-Solid Interactions, Dept. 1111
Phone: (505) 844-7568, Fax: (505) 844-7775, Email: bldoyle@sandia.gov

Nuclear reactions for neutron/gamma interrogation sources.

Reaction	Interrogation Particle	Cross Section
$^{11}B(p,\gamma)^{12}C$	12-MeV gammas	0.16 mb @ 163 kV
$^{19}F(p,\alpha\gamma)^{16}O$	6-MeV gammas	160 mb @ 340 kV
$^{7}Li(p,\gamma)^{8}Be$	15/18 MeV gammas	6 mb @ 441 kV
$^{7}Li(d,n)^{8}Be$	13 MeV neutrons	50 mb @ 300 keV

References:

1) A.J. Antolak, B.L. Doyle, K.N. Leung, D.H. Morse, P. Provencio, "Active Interrogation Using Low-Energy Nuclear Reactions", (Proceedings of SPIE: Penetrating Radiation Systems and Applications VII, F.P. Doty, H.B. Barber, and H. Roehrig, Editors) v. 5923 (2005) 592303-1.

2) B.A. Ludewigt, A.J. Antolak, E. Henestroza, J.W. Kwan, M. Leitner, K.-N. Leung, W. Waldron, S. Wilde, "Coaxial Mono-Energetic Gamma Generator for Active Interrogation", AIP Conference Proceedings: CAARI2008, (2008).

Depolarization measurements of biological aerosols for standoff detection

by ***R. L. Schmitt, S. M. Sickafoose, M. S. Johnson, and P. J. Hargis, Jr.***

Motivation—LIDAR (Light Detection and Ranging) systems are now a key component in the DoD strategy to protect troops from biological weapons in the battlefield. Although UV laser induced fluorescence LIDAR systems have been quite successful in detecting and discriminating biological aerosols at ranges exceeding 3 km, these systems sometimes confuse diesel smoke with weakly fluorescing biological aerosols. In order to reduce the false alarm rate due to diesel smoke, LIDAR systems are now exploiting the depolarization of the elastically scattered laser light as an additional factor to aid in discrimination. To optimally use this new information in discrimination algorithms, calibrated measurements of the depolarization ratio for a wide variety of relevant biological and non-biological aerosols are needed.

Accomplishment—Since the size, shape, and composition of biological particles (cells and spores) are markedly different than diesel smoke (soot particles), the depolarization of backscattered light from these particles should be different. For example, a spore which is oblong in shape will tend to depolarize scattered light whereas a spherical soot particle will not.

We modified the Sandia B70 LIDAR trailer to measure elastic backscatter depolarization ratios at 355 nm and 1064 nm, and used the enhanced system to measure depolarization ratios of a variety of aerosol clouds at a range of 1.2 km. The measurements were made during several field test campaigns conducted at Dugway Proving Ground.

A schematic diagram of the B70 LIDAR system is shown in Figure 1. A Q-switched Nd:YAG laser produces both 1064- and 355-nm pulses which are directed towards the aerosol cloud using a series of turning mirrors. Backscattered light is collected by a large telescope, collimated, and sent to a series of detectors.

The depolarization detection system, shown in Figure 1, consists of $\lambda/2$ and $\lambda/4$ waveplates to compensate for polarization ellipticity induced by mirror reflections, a Glan-Taylor polarizer to separate the two orthogonal polarizations, a spatial filter to improve polarization purity, and a photodetector in each channel to measure the light. The 1064-nm channel uses Si Avalanche Photodiode (APD) detectors and the 355-nm channel uses photomultiplier tubes. The signals are digitized by an oscilloscope and processed to obtain the depolarization ratio as a function of time.

Figure 2 shows a subset of the measured depolarization values from agent simulants. The first four simulants are released dry, while the second four are released wet. Wet-release simulants are encased in water and appear more spherical to polarized laser radiation; with a correspondingly lower depolarization ratio.

Significance—We have made calibrated elastic backscatter depolarization measurements on a wide variety of biological aerosols and common interferents (such as diesel smoke). This database will be used to design more robust discrimination algorithms and also to design optimum receiver configurations for new standoff LIDAR systems. To properly exploit depolarization ratio in a scanning LIDAR system, one must compensate for the polarization ellipticity induced by the beam directing mirrors on both the transmitter and receiver.

Sponsors for various phases of this work include: DoD Joint Biological Standoff Detection Systems

Contact: Randy Schmitt, Lasers, Optics, and Remote Sensing, Dept. 1128
Phone: (505) 844-9519, Fax: (505) 844-5459, Email: schmitt@sandia.gov

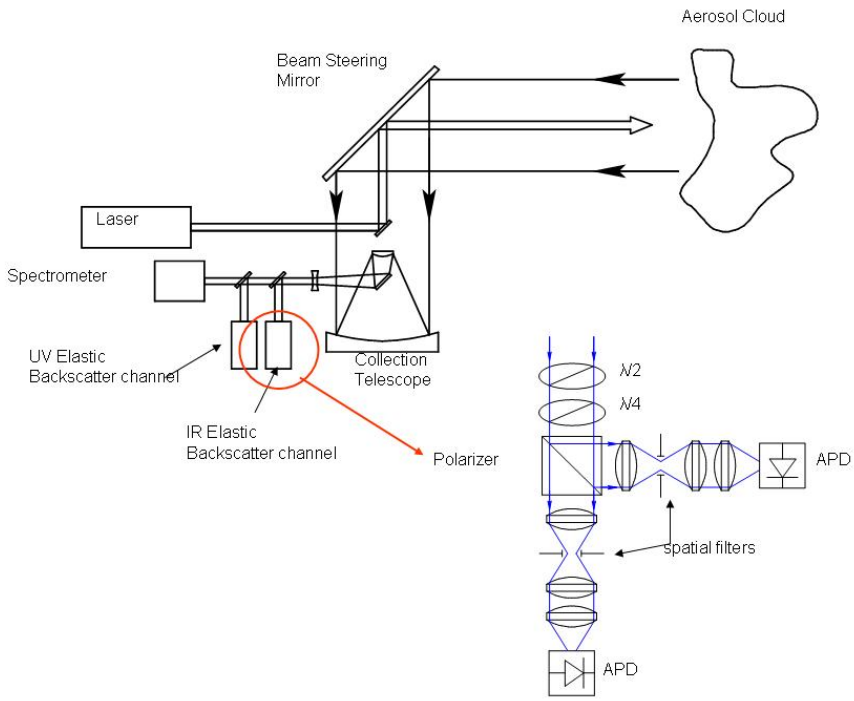

Figure 1. Schematic diagram of B70 LIDAR system. Inset shows details of the depolarization setup.

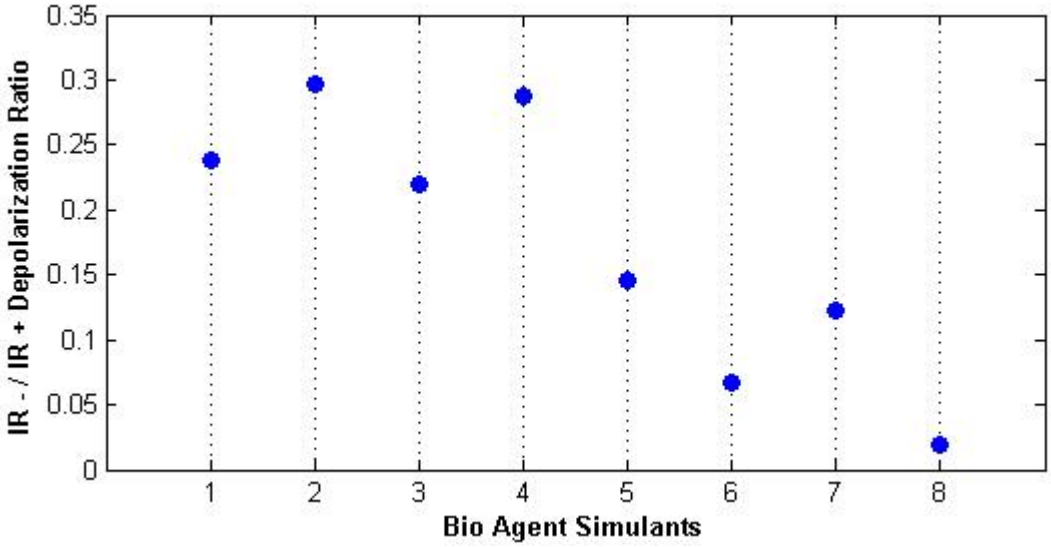

Figure 2. Depolarization values for selected simulants. The first four materials are dry, while the second four are released wet.

GaN and Related Materials

Mg Doping of AlGaN Alloys for Optoelectronic Devices

by A. A. Allerman, M. H. Crawford, and A. M. Armstrong

Motivation—AlGaN semiconductors have emerged as materials of great technological importance. With direct energy bandgaps that are tunable throughout much of the ultraviolet (UV) region of the spectrum (200-365nm), compact solid-state, solar-blind detectors as well as UV light emitting diodes (LEDs) and laser diodes have been demonstrated in this alloy system. Relevant applications for these devices include fluorescence-based biological agent detection, non-line-of-sight communication, portable water purification, and quantum information processing.

A major challenge of realizing high performance AlGaN optoelectronic devices, especially laser diodes, is the difficulty of achieving low resistivity p-type alloys of even modest Al composition (~10%). Mg is the most effective p-type dopant to date, yet it still exhibits an extremely large acceptor activation energy, which increases with Al composition from ~200meV in GaN to as high as ~400meV in AlN. We have focused on minimizing the p-type resistivity of Mg doped AlGaN alloys by optimizing the metal-organic chemical vapor deposition (MOCVD) process.

Accomplishment—AlGaN films with an Al composition of 30% were grown using bis(cyclopentadienyl)magnesium, trimethyl-aluminum, trimethylgallium and NH_3 at 75torr. Gas flow conditions in the reactor were previously optimized to minimize parasitic, gas-phase chemical reactions that could mask intrinsic effects of growth conditions. Optimal activation of the Mg dopant was achieved using a post growth anneal in a N_2 ambient at 900°C for 2 minutes. Hot probe measurements were used to confirm p-type conductivity, and conventional van der Pauw measurements were used to measure resistivity. The focus of these growth studies was to minimize the resistivity of $Al_{0.3}Ga_{0.7}N$ films by optimizing critical growth parameters such as temperature, and flux of NH_3 and group-III sources.

Figure 1a suggests that the resistivity of $Al_{0.3}Ga_{0.7}N$ films is dominated by the NH_3/group-III ratio when the ratio is less than ~1200. However, the Mg flux dominates when the NH_3/group-III ratio exceeds ~1200 (Fig. 1b). The higher NH_3 flux presumably leads to more effective p-type doping by reducing the density of n-type, compensating nitrogen vacancies. The resistivity is relatively insensitive to changes in growth temperature from 990°C to 1025°C once NH_3, Mg and group-III fluxes are optimized.

Under optimized conditions, a resistivity of 8 ohm-cm is achieved for $Al_{0.3}Ga_{0.7}N$ films which is one of the best results reported for this composition. Figure 2 shows the resistivity measured for AlGaN films with Al compositions from 10% to 30% using optimized conditions developed in this work. P-type AlGaN films at these compositions have been used in our effort to develop laser diodes with emission at UV wavelengths.

Significance—The ability to effectively p-type dope AlGaN films with Al compositions to 30% is a key element in realizing laser diodes with emission near 340nm. With improved performance enabled by more effective p-type doping, AlGaN optoelectronic devices will replace photomultiplier tubes, mercury lamps, and large frame lasers and enable a new generation of compact, robust, and portable systems for sensing and communications.

Sponsors for various phases of this work include: Laboratory Directed Research & Development, and Defense Advanced Research Projects Agency

Contact: Andrew Allerman, Advanced Materials Sciences, Dept. 1126
Phone: (505) 845-3697, Fax: (505) 844-3211, Email: aaaller@sandia.gov

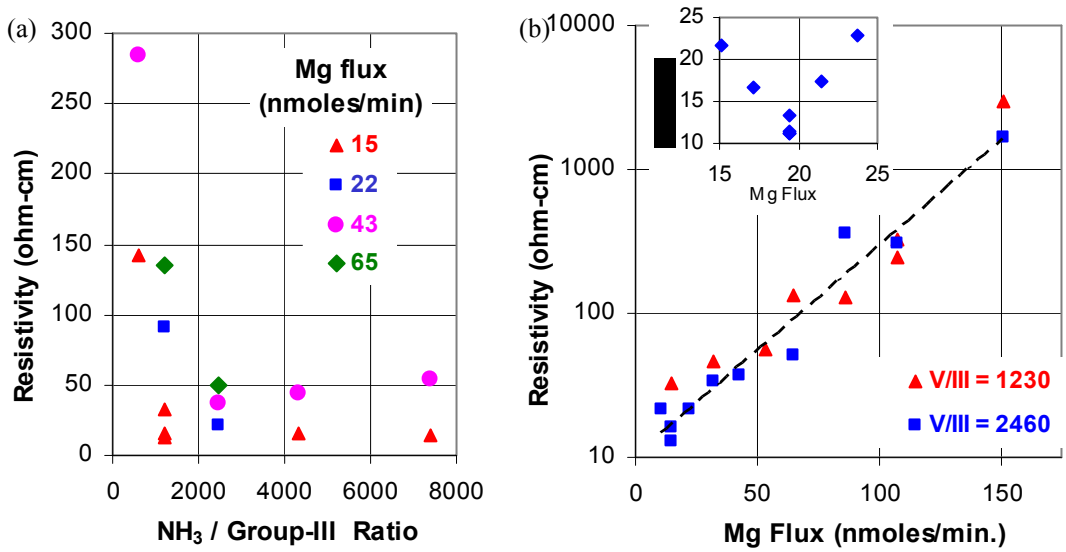

Figure 1. The resistivity of 30% AlGaN films is shown in a) where the resistivity is largely independent of NH_3 flux for NH_3/group-III ratios exceeding ~1200 and in b) where the sensitivity to Mg flux clearly dominates the effects of NH_3/group-III ratios (.i.e. V/III ratio) exceeding ~1200. The dashed line is drawn as an aid to the eye. The inset shows the resistivity eventually increasing for decreasing Mg fluxes, indicating a minimum resistivity is achieved for an optimum Mg flux.

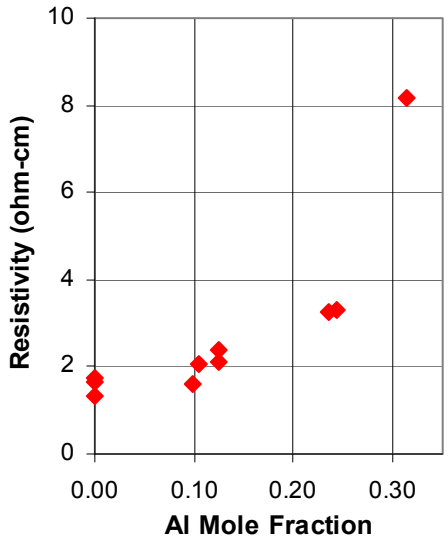

Figure 2. The resistivity of AlGaN films grown under optimized conditions from this work. The sharp rise in resistivity reflects the increase in Mg acceptor activation energy with higher Al mole fraction.

Indium-induced Step Transformation during InGaN Quantum-well Growth on GaN

by D.D. Koleske, S.R. Lee, G. Thaler, M.H. Crawford, M. E. Coltrin, and K.C. Cross

Motivation—LEDs fabricated from the group-III nitrides are surprisingly bright despite the fact that they contain high dislocation density. Several theories have been proposed to explain the efficient light emission. These theories require some form of spatially distributed energy minima that localize carriers away from non-radiative recombination centers located at dislocations; however, definitive proof for one given theory over another is still lacking. The importance of localization and the extent to which it can be manipulated to further improve light efficacy are intriguing questions.

Accomplishment—One theory proposes that InGaN-quantum-well (QW) thickness fluctuations couple to piezoelectric-fields in the QWs, thereby producing energetic fluctuations strong enough to spatially localize carriers. These QW thickness fluctuations have been observed in high-resolution TEM images, lending credence to this theory.

Recently, we have found that these thickness variations can arise naturally through changes in the structure of surface steps during InGaN growth on GaN. Figure 1 shows examples of this morphology change for single- and double-QW heterostructures. Image (a) shows an AFM of the starting GaN step structure, which is dominated by single-layer steps. Images (b) and (c) show the increase in multiple-layer steps after the growth of single $In_{0.10}Ga_{0.90}N$ and $In_{0.20}Ga_{0.80}N$ QWs. The notably greater texturing of $In_{0.20}Ga_{0.80}N$ QWs indicates that the driving force for this transformation likely depends on indium concentration in the QW. Image (d) shows a double $In_{0.20}Ga_{0.80}N$ QW structure, which has a similar step structure to the single $In_{0.20}Ga_{0.80}N$ QW in image (c). The key result is that reduced growth temperature, which is required for indium incorporation, does not act alone to alter the GaN step structure, but concomitant addition of indium to the growth does.

Figure 2 further quantifies the change in step structure as the number of $In_{0.20}Ga_{0.80}N$ QWs increases. The figure reveals two notable observations. First, the frequency of single-layer steps decreases and the frequency of multiple-layer steps increases. Second, the step-height frequencies stop changing for heterostructures containing more than two QWs, suggesting that the mechanisms that roughen and smooth the multi-QW structures are balanced by each other. In other experiments, we found that the degree of multiple-layer step evolution depends on the amount of indium incorporated into the QWs. We speculate that the InGaN roughens in an attempt to reduce the stress of the InGaN layer. Although more evidence is required, this roughened InGaN step configuration might be essential to nitride-based LED brightness by providing QW thickness fluctuations sufficient to localize the electron-hole pairs.

Significance—Although the mechanism of the electron-hole localization is not yet well understood, this research aims to investigate morphological influences on overall luminescence efficiency. As shown here, this morphology evolves naturally during InGaN growth on GaN. If this morphology influences the localization, it may explain the reason single InGaN QWs typically do not show appreciable luminescence, while multiple QWs do. Additional research is underway to correlate the InGaN morphology to the luminescence efficiency.

Sponsors for various phases of this work include: DOE Offices of Basic Energy Sciences & Energy Efficiency & Renewable Energy

Contact: Daniel D. Koleske, Advanced Materials Sciences, Dept. 1126
Phone: (505) 284-4531, Fax: (505) 844-3211, Email: ddkoles@sandia.gov

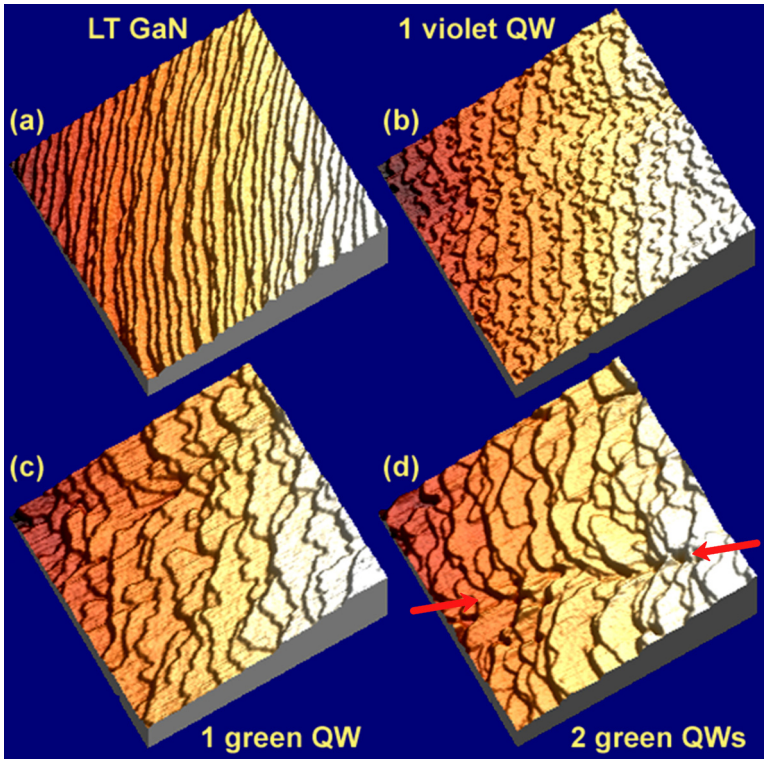

Figure 1. Atomic-force microscopy images measured after the growth of (a) a low-temperature GaN barrier layer, (b) a single $In_{0.10}Ga_{0.90}N$ quantum well (QW) capable of violet light emission, (c) a single $In_{0.20}Ga_{0.80}N$ QW capable of green light emission, and (d) two $In_{0.20}Ga_{0.80}N$ QWs. The image sizes are all 1x1 μm^2. The red arrows mark a valley feature formed at surface of the InGaN MQWs.

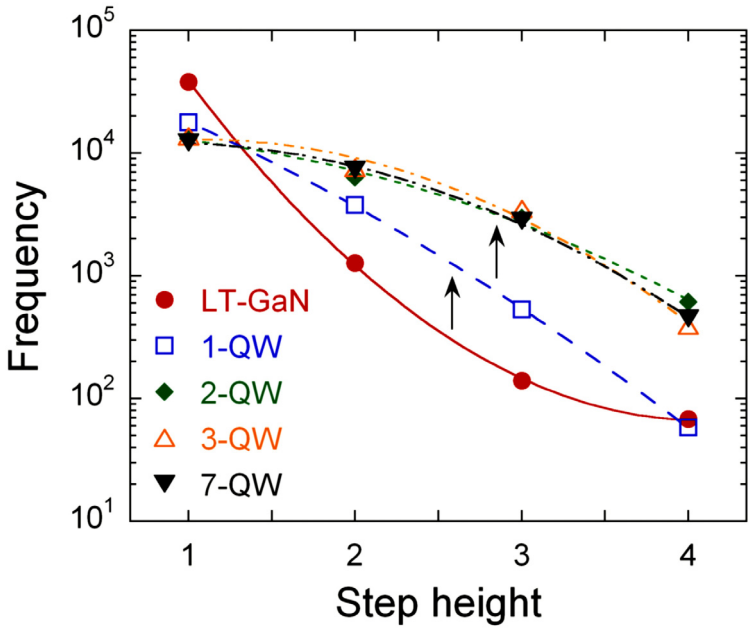

Figure 2. Step-height frequency distributions for a series of $In_{0.20}Ga_{0.80}N$/GaN heterostructures containing varying numbers of quantum wells. The step height is given in units of c/2 where c is the wurtzite lattice parameter along [0001].

Surface Plasmon Enhanced Emission from InGaN LEDs.

by A. J. Fischer, D. D. Koleske, K. W. Fullmer, A. J. Coley, and J. R. Wendt.

Motivation—Spontaneous emission of light from a semiconductor is generally thought to be characterized by a constant rate such that the efficiency of light emission is fixed for a wide range of experimental conditions. However, there are a number of methods to change the radiative recombination rate by altering the photonic density of states. By increasing the number of available final photon states for a transition, the probability for that transition can be changed. In a properly designed structure, surface plasmons can be used to increase the photonic density of states thereby increasing the radiative recombination rate resulting in an overall increase in efficiency for InGaN LEDs.

Accomplishment—Surface plasmon related enhancements to luminescence can only be observed when the metal film supporting surface plasmons is placed extremely close (< 75 nm) to an emitter. Since the field from a surface plasmon mode falls off exponentially from a metal-dielectric interface, emitters must be placed as close as possible to this interface. In our case, a single InGaN quantum well (QW) is grown very near the surface of a sample such that metal can be deposited in close proximity to the QW. The emission wavelength of the QW must also be close to the surface plasmon resonance in order to change the photonic density of states. Photoluminescence measurements have shown increases in both the total luminescence and the PL decay time for samples with a deposited metal film.

An electrically injected device showing surface plasmon enhanced emission is much more difficult due to the constraint that the QW be placed very close to the metal surface. Figure 1 shows a schematic diagram of our design for an electrically injected InGaN surface plasmon LED. A considerable amount of growth related research was required in order to grow extremely thin p-GAN material that would also form a robust contact layer for hole injection. In this design the metal film acts as an Ohmic contact to the thin p-GaN and lateral patterning of the metal is used to extract surface plasmon modes from the semiconductor. In this way, the metal film is used to increase both the radiative and the extraction efficiencies.

Light emitting diode wafers with a single QW were grown by metal-organic vapor phase epitaxy with different p-GaN thicknesses. Material with a very thick p-GaN layer is not expected to show surface plasmon enhancements since the QW is far from the metal interface. Figure 2 shows light vs. current curves for an InGaN surface plasmon LED with emission at 450 nm with a p-GaN thickness of 50 nm compared to a control LED with a standard thickness p-GaN layer (200 nm). The inset of the plot shows the enhancement factor as a function of drive current. At low current where there is increased non-radiative recombination, enhancements as high at 15 times have been observed, whereas at higher current, where solid state lighting devices will operate, an enhancement of about 7 times has been observed due to surface plasmon effects.

Significance—Poor internal quantum efficiency continues to be a problem for InGaN LEDs particularly for emission at green and yellow wavelengths. This work shows that surface plasmons can be used in a practical device structure to enhance efficiency. Surface plasmon mediated emission has the potential to dramatically improve the efficiency of longer wavelength green and yellow emitters for solid state lighting applications.

Sponsors for various phases of this work include: Department of Energy Office of Energy Efficiency & Renewable Energy, and Laboratory Directed Research & Development

Contact: Arthur J. Fischer, Chemical Processing Sciences, Dept. 1123
Phone: (505) 844-6543, Fax: (505) 844-3211, Email: ajfisch@sandia.gov

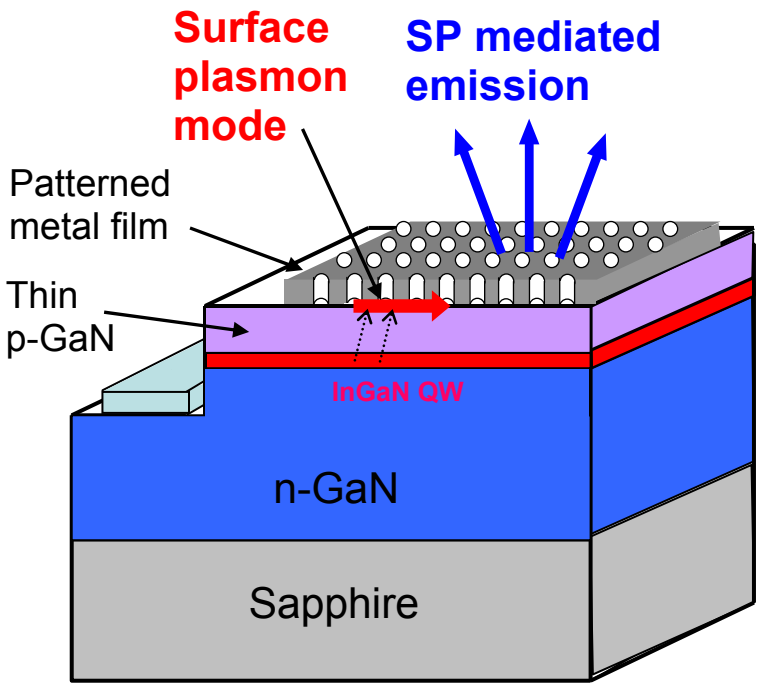

Figure 1. Schematic diagram of an electrically injected InGaN surface plasmon LED showing a patterned metal film for extraction of surface plasmon modes.

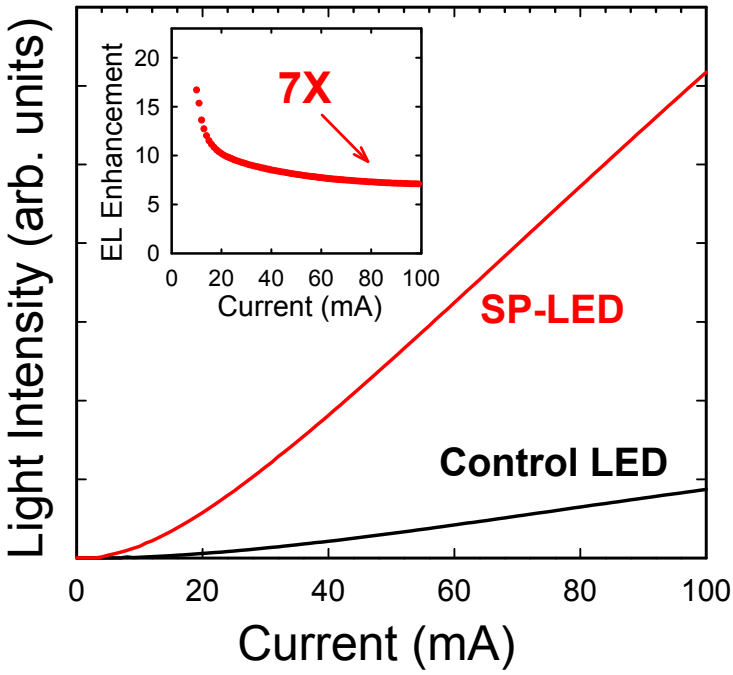

Figure 2. Light vs Current for a surface plasmon LED (SP-LED) compared to a control LED. The inset shows the enhancement due to surface plasmons as a function of current.

Observations of Gas-phase Nanoparticles during InGaN MOCVD

by J. Randall Creighton, Michael E. Coltrin, and Jeffrey J. Figiel

Motivation—InGaN alloys are foundational for current and likely-future solid-state-lighting (SSL) architectures because their bandgaps match the human visual response and the solar spectrum. Metal-organic chemical vapor deposition (MOCVD) is normally used to grow epitaxial InGaN thin films for such devices, but a number of significant complications arise that make this a very challenging process. In general, indium incorporation into the growing InGaN films is very inefficient, temperature sensitive, and difficult to control. While these problems are often thought to be due to the limited thermodynamic stability of InGaN, other issues such as gas-phase parasitic chemical reactions may well play an important and previously unrecognized role.

Accomplishment—Example images of nanoparticles formed during InN MOCVD conditions comparing H_2 and N_2 carrier gases are shown in Fig. 1. The InN results in H_2, Fig. 1(a), are similar to the earlier GaN and AlN results, with particles residing ~5 mm from the heated surface. Switching to N_2 carrier gas at the same flow rate causes the nanoparticles to move much closer (~2 mm) to the surface, see Fig. 1(b). While there is some evidence that switching carrier gases affects the degree of nanoparticle formation (scattering intensities change), the large shift in nanoparticle position is entirely consistent with the different physical properties of H_2 and N_2. In fact the thermal boundary layer thickness in H_2 is expected to be about 2.6 times thicker than for N_2, consistent with these measurements. The nanoparticle position is determined by the counterbalancing of the thermophoretic and convective forces, and thus they will congregate in a layer much closer to the surface when N_2 is used as the carrier gas.

To determine the nanoparticle size we measured the angular dependence of the scattering intensity around 90° using the p-polarization condition. In the small particle size limit ($d \ll \lambda$) the p-polarized intensity should closely approximate a $\cos^2(\theta-\Delta)$ function, where the small angular shift Δ contains the size information. For dielectric nanoparticles, Δ is > 0, and the scattering curve minimum is shifted to an angle $\theta_{min} = 90 + \Delta$. As shown by the example in Figure 2, our p-polarized scattering results for InGaN MOCVD conditions (N_2 carrier gas) consistently show a shift with $\Delta < 0$ ($\theta_{min} < 90°$), which is indicative of metallic nanoparticles. We therefore analyzed the scattering results using the optical constants for liquid indium at elevated temperatures.

Over a range of temperatures typically used to deposit InGaN (and using N_2 carrier gas) the nanoparticle diameters were 24-45 nm for InGaN, and 21-35 nm for InN conditions. Near 800°C under InGaN conditions the particle density (N_p) was in the range of 1-2 X 10^9 cm^{-3}, and for InN conditions N_p was in the range of 1-4 X 10^9 cm^{-3}. Near 800°C a large fraction of the input indium (near 100% within experimental uncertainty) is consumed in forming the nanoparticles, and is unavailable for InGaN deposition.

Significance—The large quantity of indium converted into nanoparticles demonstrates that gas-phase parasitic processes play a very significant, detrimental role while depositing InGaN films for SSL applications. Now that we recognize the significance of this process, it should be possible to mitigate the associated problems through proper reactor design and process optimization.

Sponsors for various phases of this work include: DOE Office of Energy Efficiency & Renewable Energy

Contact: J. Randall Creighton, Advanced Materials Sciences, Dept. 1126
Phone: (505) 844-3955, Fax: (505) 844-3211, Email: jrcreig@sandia.gov

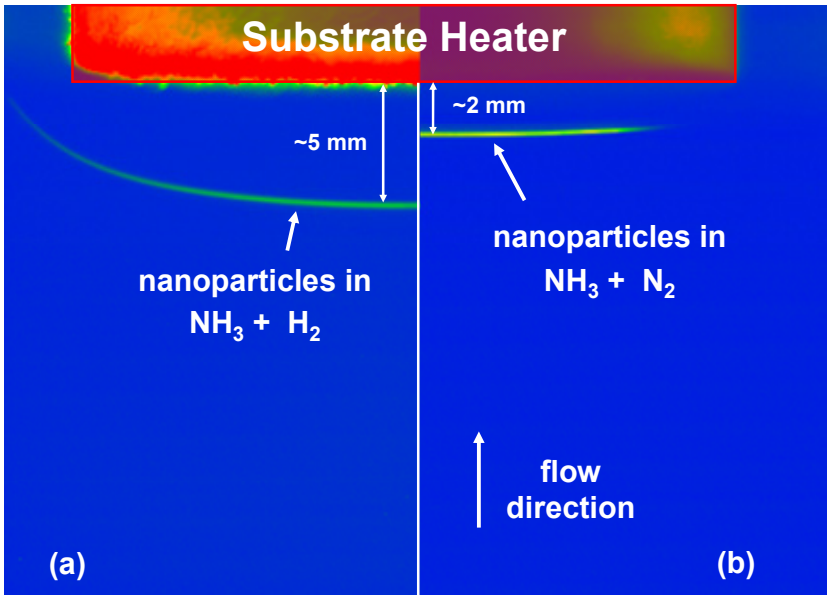

Figure 1. Laser illumination reveals a sharp layer of particles residing 5 mm (in H_2) and 2 mm (in N_2) from the heated surface during InN MOCVD at ~800°C, 200 Torr (inverted stagnation point flow geometry). The outline of the heater has been highlighted with the red rectangle.

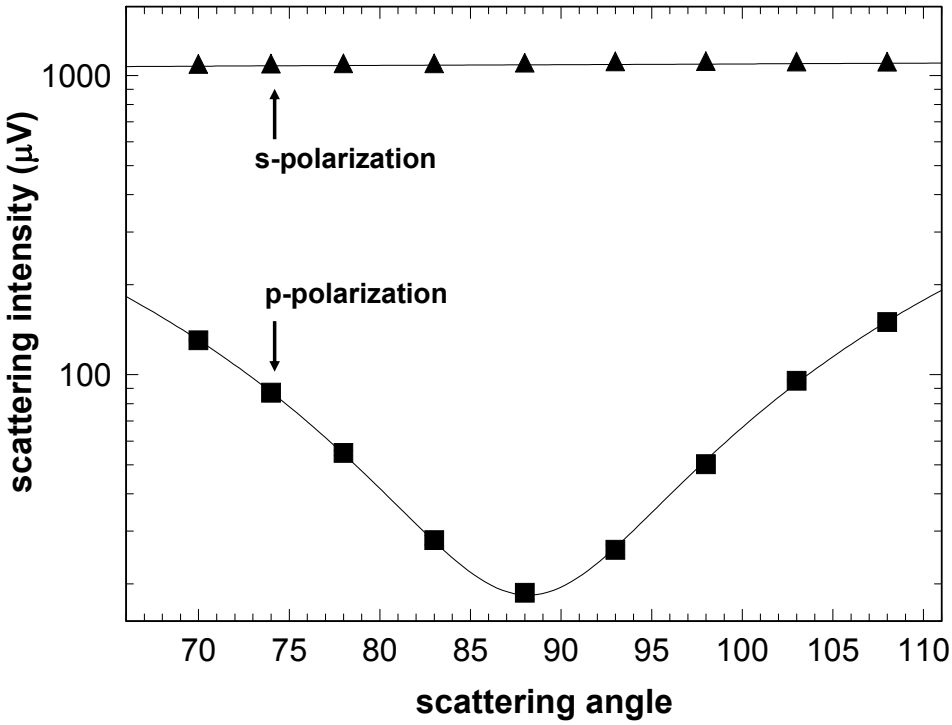

Figure 2. Angular dependence of the scattering intensity for s-s (triangles) and p-p (squares) polarization configurations during InGaN MOCVD at 757°C, 200 Torr. TMIn flow rate = 38.4 μmole/min, TMGa flow rate = 13.8 μmole/min.

Deep Level Optical Spectroscopy of GaN Nanowires

by A. Armstrong, G. T. Wang, Q. Li and A. A. Talin

Motivation—GaN-based nanowire (NW) applications include chemical sensing and light emitters spanning the IR to UV spectrum. An advantage of GaN NWs compared to thin films is their lack of threading dislocations. However, point defects still impact the electrical and optical properties of GaN NWs. Therefore, quantitative defect spectroscopy has been developed for GaN NWs to study the atomistic origin and role of defects.

Accomplishment—Deep level spectroscopy of GaN NWs has been limited mainly to luminescence, which is not quantitative in defect energy level (E_o) or defect density (N_t). Thus, we have demonstrated the applicability of deep level optical spectroscopy (DLOS) for GaN NWs. DLOS provides quantitative values for E_o and N_t, but is a photocapacitance technique that was originally developed for macroscopic diodes with planar geometry. We have extended DLOS to a photoconductivity technique for NWs with three-dimensional depletion regions.

GaN NWs were grown by metal-organic chemical vapor deposition (MOCVD) via the vapor-liquid-solid mechanism using Ni particles as a growth catalyst. The NWs were transferred to a Si substrate, and electrical contacts were made using optical lithography to form individual devices. DLOS measurements were performed by scanning the energy $h\nu$ of sub-bandgap light incident upon the NWs. When $h\nu$ is large enough to photoionize deep levels, a photoconductivity transient is measured. Majority carrier photoemission reduces the surface depletion region, which in turn increases the conductive, quasi-neutral NW cross-sectional area. The GaN NW DLOS spectrum is shown in Fig. 1. The spectral dependence of the deep level optical cross-section $\sigma_o(h\nu)$ is found by taking the derivative of the photoconductivity transient at the beginning of illumination. Abrupt onsets in the DLOS spectrum demarcate individual deep levels, and saturation occurs at the band gap E_g. E_o and the Franck-Condon shift (d_{FC}) are extracted by fitting $\sigma_o(h\nu)$ to a theoretical model. Since the NWs are *n*-type, positive photoconductivity indicates electron photoemission to the conduction band minimum E_c. Deep levels are observed at $E_c - 1.71$ ($d_{FC} = 0.77$ eV), $E_c - 2.81$ ($d_{FC} = 0.28$ eV), and $E_c - 3.19$ eV. The large d_{FC} of the former two defects indicates strong phonon coupling. The NW deep levels are similar to those observed in bulk GaN, suggesting the defects are not particular to the surface but pervade the NW volume.

N_t was estimated from the change in photoconductivity ΔI relative to the dark value I_0. Based on the electrostatics for cylindrical NWs,[1] $\Delta I/I_0$ is predicted to increase sharply with decreasing diameter, and N_t can be extracted from a fit to the model (Fig. 2). Measurements of several NWs show good agreement with the model, suggesting $N_t \sim 1.4 \times 10^{16}$ cm^{-3}.

Significance—DLOS has been extended to GaN NWs, enabling quantitative defect spectroscopy in nanoscale devices. An important application will be investigating defect incorporation as a function of NW growth method and impurity incorporation. This will provide important insight to the atomistic origin of defects in GaN NWs.

1. Calarco, *et al. Nano Lett. 5*, 981 (2005).

Sponsors for various phases of this work include: DOE Office of Basic Energy Sciences, and Laboratory Directed Research & Development

Contact: Andrew Armstrong, Semiconductor Material and Device Science, Dept. 1123
Phone: (505) 284-7757, Fax: (505) 844-3211, Email: aarmstr@sandia.gov

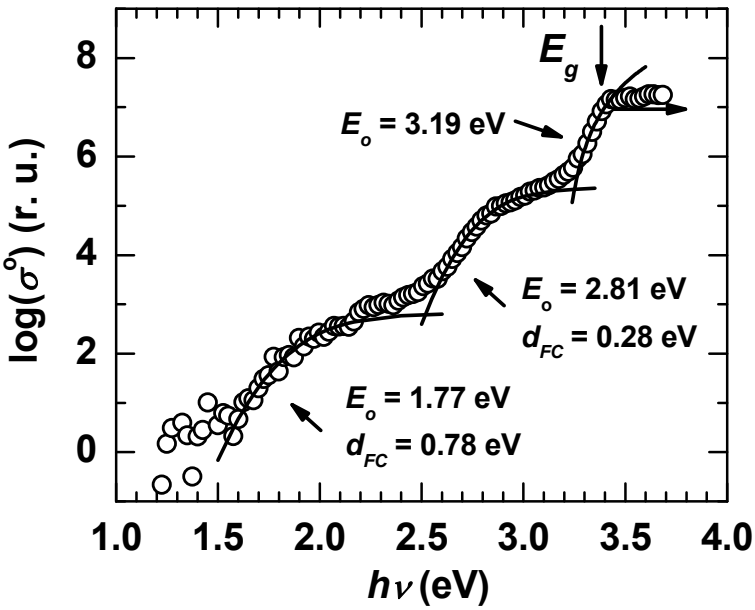

Figure 1. DLOS spectrum of a GaN NW. The symbols are experimental data and the lines are theoretical fits.

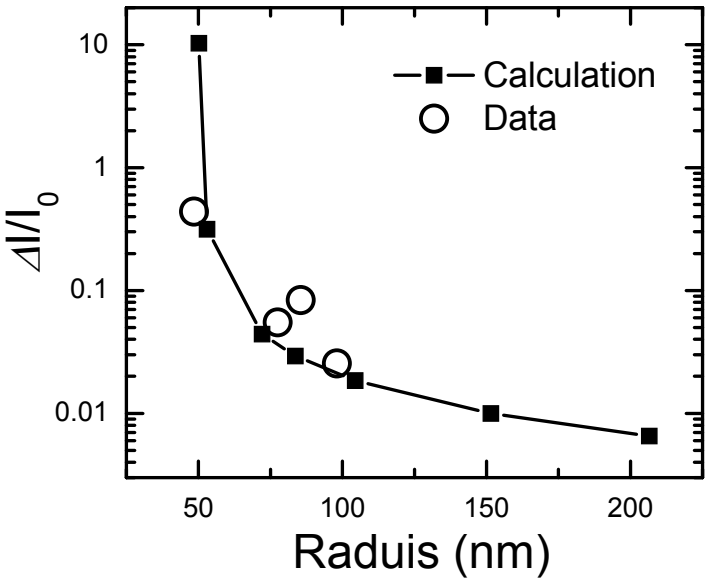

Figure 2. GaN NW photoconductivity as a function of size. The data are well fit using a model for cylindrical NWs.

Nanoscience
And
Nanotechnology

Extreme Response Field-structured Chemiresistors for Chemical Switch Arrays

by D.H. Read and J.E. Martin

Motivation—A chemiresistor is a composite whose electrical conductivity changes in the presence of chemical vapors. These sensor composites traditionally consist of carbon-black particles randomly distributed within a polymer. Chemiresistors have several advantages as chemical sensors. They are small (microdot printable), simple and inexpensive to manufacture, require minimal transduction equipment, and need little power to operate (<10mW). Despite these positive attributes, traditional chemiresistors fail to satisfy numerous criteria essential to a viable chemical sensor technology. Problems include: poor baseline stability (drift); poor sensor-to-sensor consistency; poor response reproducibility; and irreversible response. These problems are due to the chemical affinity of carbon black to organics, the random, uncontrolled structure of the particle network, and the fact that the polymer phase is often non-crosslinked.

Our goal is to determine whether magnetic field-structured composites will yield improved chemiresistors that eliminate all of the current problems. If successful, there are numerous arenas where field-structured chemiresistors (FSCRs) can have impact, including environmental and chemical process monitoring, homeland security, and military applications.

Accomplishment—We have demonstrated that FSCRs successfully address all of the difficulties with carbon black chemiresistors, while achieving much greater sensitivity (Figure 1), and controllability. These FSCRs are composed of electrically conductive magnetic particles encapsulated in an elastomeric matrix. The particles are organized into conducting pathways by magnetic fields during cure. The type of field used determines the structure of the particle network (Figure 2), which in turn determines the chemiresistor sensitivity. When exposed to chemical vapors, the polymer swells only slightly, yet this is amplified into a large resistance change, as much as 100,000,000,000%, at a swelling of only 1.5%. Because FSCRs transition from electrically conducting to insulating over a narrow range of analyte concentration, they function as chemical switches. We have developed methods of shifting the sensor response to lower or higher analyte concentrations and can now vary the switching point over a two-decade concentration range. We can also control the range of analyte concentrations over which the sensor has a measurable response. This tailorability enables us to create chemical switch arrays that cover broad ranges of analyte concentrations.

Finally, we have isolated the fundamental transduction mechanism of FSCR response, and have demonstrated an analyte-independent master transduction curve for a particular sensor. This latter discovery shows that once any individual sensor is calibrated with a single analyte, its response to any other analyte can be reliably predicted. This is an essential characteristic for a practical chemical sensor.

Significance—This patented technology is currently in the process of being licensed for environmental monitoring of underground fuel tanks. Other commercialization opportunities are also being pursued.

Sponsors for various phases of this work include: DOE Office of Basic Energy Sciences

Contact: Douglas H. Read, Nanomaterials Sciences, Dept. 1112
Phone: (505) 844-5338, Fax: (505) 844-4045, Email: dhread@sandia.gov

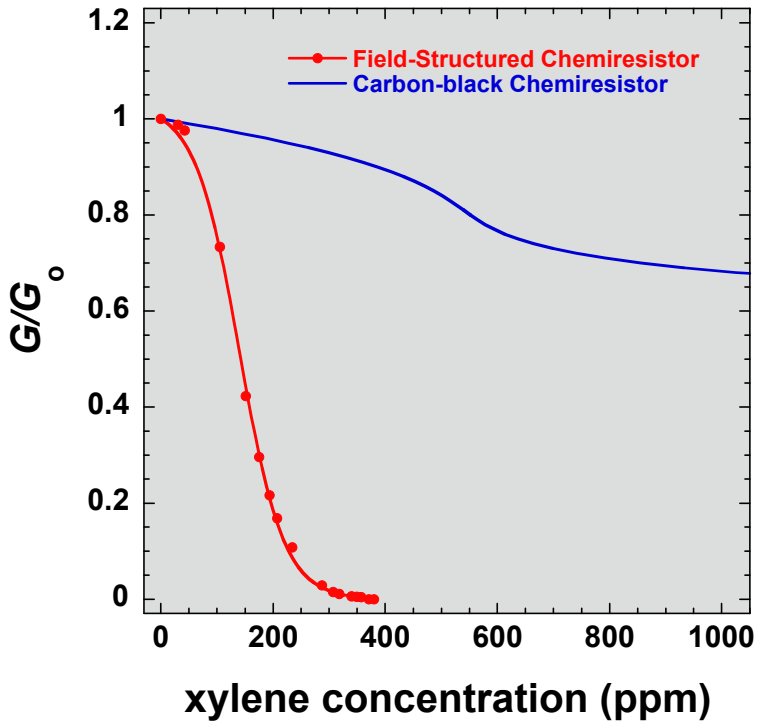

Figure 1. Response data for an FSCR and a carbon-black chemiresistor exposed to xylene. *G* is the conductivity of the sensors at a particular analyte concentration and G_o is the conductivity with no analyte present. The FSCR is a 15vol.% gold-plated nickel particle composite using PDMS as the polymer phase. The carbon-black sensor data represent the fit to the data presented in fig.48, p.63 of SAND2003-3410 for a PEVA polymer sensor.

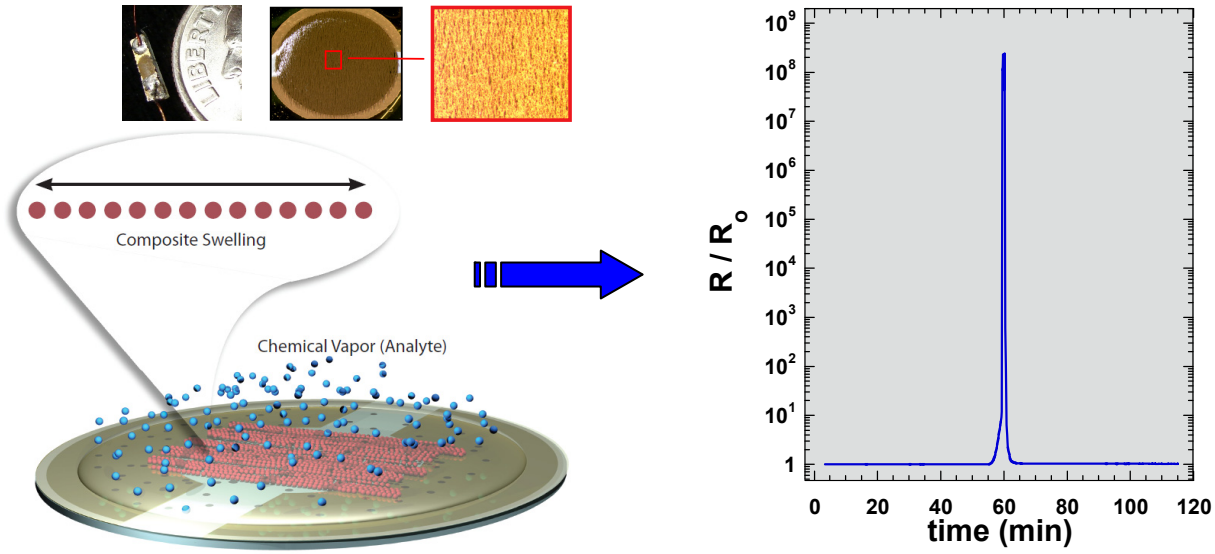

Figure 2. Photos of FSCRs (left: FSCR next to a U.S. dime) with a 60x magnified view of the chain-like particle structure. FSCR operation schematic showing analyte absorption and composite swelling. The composite swelling results in an extreme response of the FSCR to 17µg/mL *p*-xylene. The sensor resistance, *R*, increases by 300,000,000 times over its initial value, R_o.

Integrated Contamination Layers for Corrosion Sensors

by N. Missert, J. Rivera and R. G. Copeland

Motivation—Atmospheric corrosion is an important degradation mode for microelectronic components. The extremely small length scales associated with such components often mean that even a small amount of corrosion can significantly degrade performance, or even be catastrophic to the functionality of the device. Consequently, device failure may provide the first indication that a corrosion problem exists. Ideal corrosion sensors would be small, inexpensive devices which could be integrated into a component, system, or tester for *in situ* detection of accelerated corrosion processes before the onset of significant corrosion of the actual electronic devices. These sensors need to controllably degrade under a wide range of environmental conditions and have a measurable response that can be correlated with corrosion of real components. The sensors must incorporate corrosive contaminants and undergo tunable degradation.

Accomplishment—In order to develop an integrated contamination layer, we investigated evaporated thin films of NaCl. This layer was integrated with a microgalvanic couple to characterize the susceptibility to corrosion in humid environments. The microgalvanic couple is a simple Al-Au or Al_2Cu-Au meander line, designed to have high sensitivity to small corrosion volumes and enhanced susceptibility to relevant corrosion mechanisms. Figure 1(a) shows that a dense, homogeneous film of ~ 150 nm NaCl crystals was achieved on thin film Al. The distribution of crystallites using thermal evaporation is much more uniform than that obtained previously by standard "salt-spray" techniques. Al–Au and Al_2Cu-Au meander lines were fabricated using electron beam evaporation of the thin films onto SiO_2 coated Si substrates, in combination with standard photolithography, as shown in Figure 1 (b). The meander line consists of a series of twenty 5 µm wide bridges of Al or Al_2Cu that span 25 µm wide Au bars. This design was chosen to test two types of sites susceptible to corrosion: the contact areas and the proximity of the long bridges to the Au bars, which provide large areas for cathodic reactions.

The resistance is measured across the entire array in humid environments. The Al_2Cu films are more susceptible to corrosion. Figure 2 (a) shows an example of the change in resistance of an Al_2Cu-Au microgalvanic couple, with a 60 nm layer of evaporated NaCl, during exposure to 79% relative humidity. The response of a bare couple in aqueous 100 mM NaCl is shown in Figure 2 (b) for comparison. Mass transport limitations within the electrolyte layer in humid environments lead to a longer time to failure relative to aqueous exposures. The time to failure in humid environments is sensitive to both the thickness of the NaCl layer and the relative humidity.

Significance—Engineered aging structures that are susceptible to corrosion in humid environments are needed to act as early warning detectors of potential corrosion problems. This work, which integrates a contamination layer with an Al_2Cu-Au microgalvanic couple, demonstrates a sensor with tunable susceptibility to corrosion in humid environments. Calibration of this prototype sensor will ultimately allow *in situ* monitoring of device degradation in humid environments.

Sponsors for various phases of this work include: Nuclear Weapons: Enhanced Surveillance Campaign

Contact: Nancy Missert, Nanomaterials Sciences, Dept. 1112
Phone: (505) 844-2234, Fax: (505) 844-1197, Email: namisse@sandia.gov

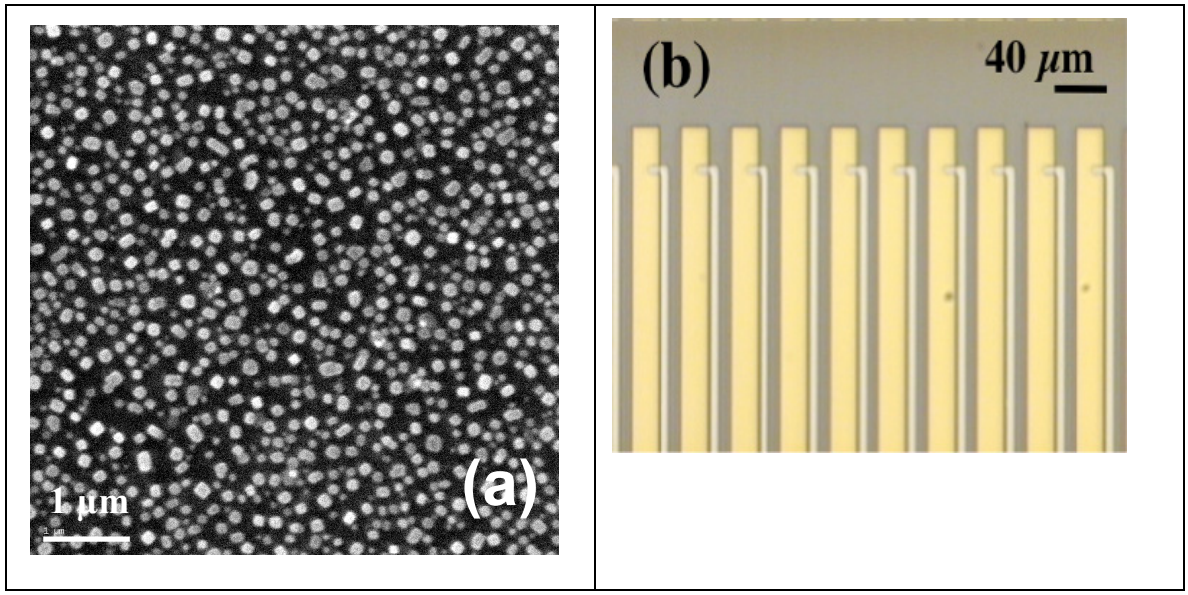

Figure 1. (a) Scanning electron micrograph of thermally evaporated NaCl crystals on Al showing homogeneous distribution. (b) Optical image of Al-Au meander line.

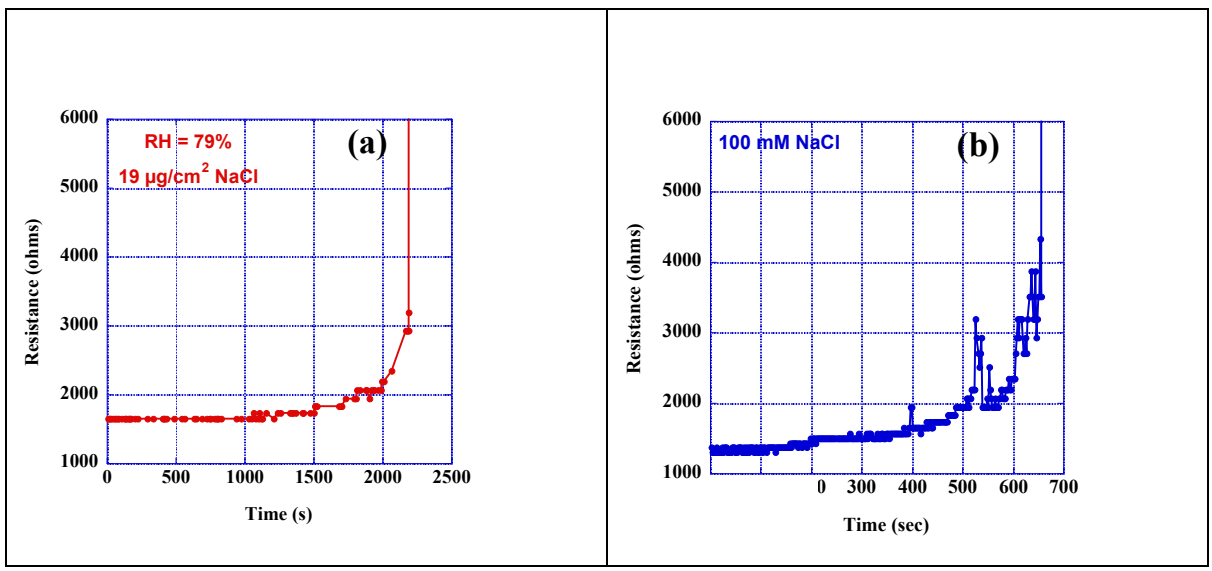

Figure 2. (a) Resistance change of a microgalvanic couple with incorporated NaCl layer during exposure to 79% relative humidity. (b). Resistance change of a microgalvanic couple (without incorporated NaCl layer) during exposure to aqueous 100 mM NaCl. Longer time to failure in 79% RH is indicative of mass transport limitations in the adsorbed water layer.

High Refractive Index TiO_2 Nanoparticle/Silicone Composites

by T. C. Monson and D. L. Huber

Motivation—There is a great need for moldable and processable high index of refraction (n) optical materials. Optical silicones have excellent material properties but are limited to n ~ 1.5. Increasing the refractive index of optical silicones (and being able to fabricate silicones with a range of refractive indices) will make a dramatic impact in a range of applications including optics for space environments and optical encapsulants. One common application that routinely uses silicone optical encapsulants is high brightness light emitting diodes (LEDs).

Accomplishment—In an effort to increase the index of refraction of optical silicones through the incorporation of inorganic materials, we have developed a new synthesis route for TiO_2 nanoparticles. Nanoparticles are an excellent choice for incorporation into optical encapsulants because their small size will not scatter visible light. Titania's material properties are ideal for this application because it is transparent to visible light and has a high refractive index (n=2.7).

Our synthesis is based on the hydrolysis of titanium isopropoxide which in the past was not a viable method for producing nanoparticles. Through careful control of the reaction conditions and by slowing the hydrolysis rate, we have successfully achieved nanoparticle growth. The nanoparticles can be synthesized with both isopropanol and trimethoxy(7-octen-1-yl)silane (a silane molecule terminated with a vinyl group) surfactants. These ligands can be replaced with other molecules if desired. The TiO_2 nanoparticles produced by this reaction have a small diameter (~ 5 nm) and a narrow size distribution, as can be seen in the transmission electron micrograph displayed in Figure 1. As a consequence of their small size, the particles do not scatter light with a wavelength > 350 nm, as determined from their UV-vis absorption spectrum (inset of Figure 2).

Since these nanoparticles are synthesized using surfactants, they do not form large agglomerates that would scatter visible light. (Commercially synthesized titania nanoparticles, which are typically fabricated through the spray hydrolysis of titanium tetrachloride and without the use of surfactants, contain particles as large as 50 nm in diameter and form agglomerates that can approach a μm in size.) The surfactants on the surface of our nanoparticles have an additional benefit in that they provide useful functionalities which allow the particles to be incorporated directly into a silicone matrix. The vinyl termination group on the trimethoxy(7-octen-1-yl)silane ligands is identical to the termination group on many commercial optical silicones. This allows our nanoparticles to disperse very uniformly and crosslink directly into a silicone matrix. Initial measurements of titania/silicone composites made by spin coating up to 5 wt.% TiO_2 in silicone show that we can achieve refractive indices as high as 1.9. (The final concentration of TiO_2 is higher in the final composite film than in the solution used to cast it.)

Significance—The highest refractive indices achieved in these optical composites could enable us to double the light extraction from high brightness LEDs. Controlling the mass loading of titania nanoparticles in silicone matrices allows for tuning of the composite's refractive index, making this technology also useful in other applications, such as flexible optics.

Sponsors for various phases of this work include: Laboratory Directed Research & Development

Contact: Todd C. Monson, Nanomaterials Sciences, Dept. 1112
Phone: (505) 845-2129, Fax: (505) 844-1197, Email: tmonson@sandia.gov

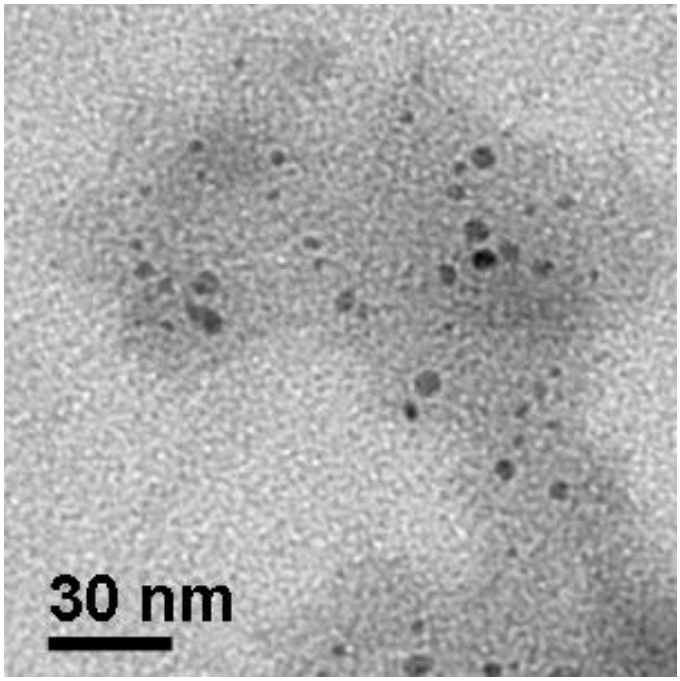

Figure 1. Bright field transmission electron micrograph of TiO_2 nanoparticles (dark spots of the image).

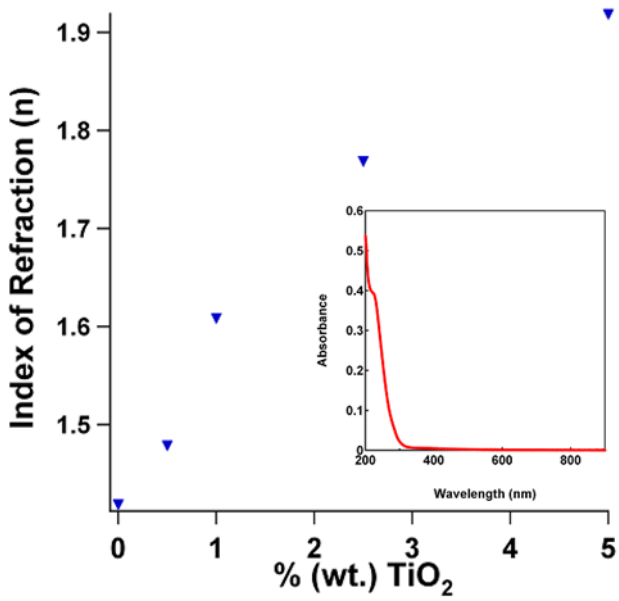

Figure 2. The index of refraction (n) of TiO_2 nanoparticle/silicone composites as a function of % (wt.) of titania in the solution used to spin coat the composites. The inset displays the UV-vis absorption spectrum for TiO_2 nanoparticles used to form the composites.

Epitaxial Diamond Growth on Ir(100) Surfaces

by T.A. Friedmann, J.P. Sullivan, E.S. Piekos, and S.L. Shinde

Motivation—The growth of large-area high-quality diamond thin films is limited by the ability to nucleate diamond on non-diamond substrates. Typically, diamond nucleates only sparsely on non-diamond substrates, and it is difficult to obtain aligned grains, limiting the quality of subsequently grown films. Recently, it has been found that the Ir(100) surface is particularly suited to nucleating oriented diamond crystallites. Unfortunately, Iridium is one of the rarest metals on earth, and large area crystals are not available. Silicon, on the other hand, is abundant, and large area wafers are routinely produced, suggesting that thin-film Ir layers on Si might be feasible for producing large area diamond films. Ir forms an undesirable silicide at typical diamond growth temperatures. One solution is to provide a nonreactive buffer layer between the two materials.

Accomplishment—We have used pulsed-laser deposition to produce thin (~25 nm) Yttria Stabilized Zirconia (YSZ) layers on 4" Si substrates. The Ir thin film (200 nm) is sputter deposited immediately following the YSZ deposition without breaking vacuum. X-ray diffraction results (Figure 1) show that we have achieved highly oriented films that are epitaxially aligned with the Si(001) substrate. The small fraction of (111) oriented Ir material present should have no significant effect on the subsequent diamond growth. For the YSZ material, it is important to perform the initial deposition in high vacuum (~10^{-7} Torr) to establish epitaxy with the silicon. Subsequent YSZ deposition is done in an oxygen background gas to maintain stoichiometry. For the Ir layer, the two most important deposition parameters for producing the favored (100) orientation are the substrate temperature (~775 °C) and the Ar gas pressure (2 mTorr) during sputtering. At lower temperatures and higher pressures, films with mostly (111) orientation are produced.

For the diamond nucleation and deposition, we commissioned a new microwave CVD system that enabled us to nucleate and grow epitaxial diamond layers upon the oriented Ir layers. An example of a (100) oriented epitaxial diamond layer is shown in Figure 2. Control of the diamond nucleation step is critical for growing oriented films, and we have found that a high negative DC bias (-350V) gives the best results. These diamond layers can be patterned using procedures developed in previous projects, and are suitable for creating device structures.

Significance—The problem of growing high-quality diamond thin films reduces to one of producing large area Ir(100) surfaces and uniformly nucleating diamond on this surface. Our progress towards this goal means that diamond thermal management, electronics, and MEMS applications are one step closer to fruition.

Sponsors for various phases of this work include: Laboratory Directed Research & Development, and DOE Office of Basic Energy Sciences

Contact: Thomas A. Friedmann, Nanomaterials Sciences, Dept. 1112
Phone: (505) 844-6684, Fax: (505) 844-1197, Email: tafried@sandia.gov

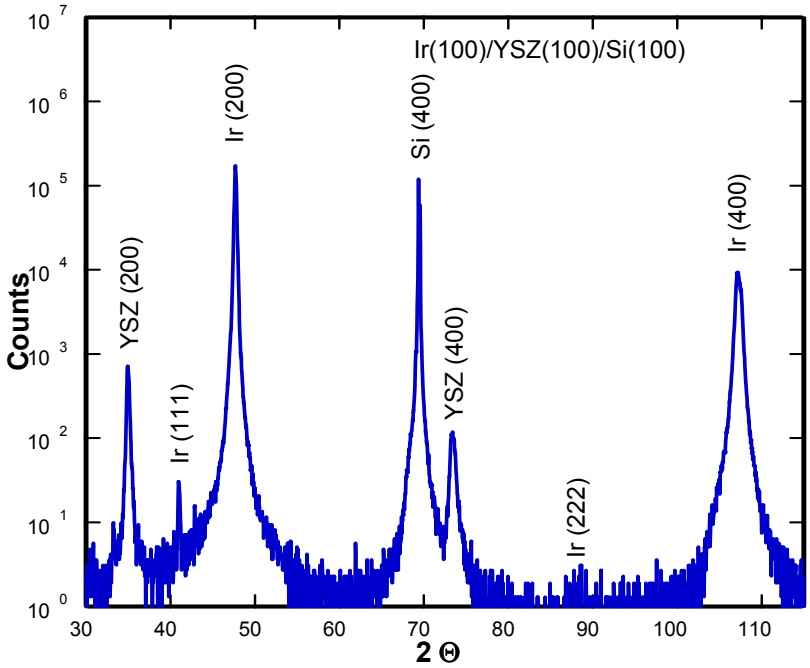

Figure 1. X-ray diffraction scan of Ir/YSZ layers on Si with a high degree of (100) orientation.

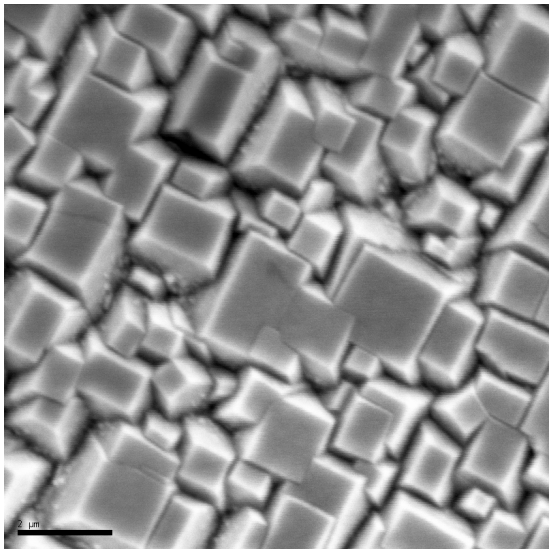

Figure 2. Epitaxial diamond layer nucleated on Ir. Subsequent textured growth produces continuous, flat surfaces.

Microstructural Origins of Saccharine Induced Stress Reduction in Electrodeposited Ni

by S. J. Hearne, and A. Bhandari, B.W. Sheldon*, S.K. Soni**

Motivation—The majority of high-strength electrodeposited Ni films form with large tensile intrinsic stress. To reduce the tensile stress, and increase the engineering yield strength, mM/l concentrations of sulfur containing additives are included in the electroplating baths. However, prior to this work there had been no direct observations as to the fundamental mechanism through which saccharin, a common industrial stress reducing additive, and in turn sulfur, reduce the deposition stress in electrodeposited Ni.

Accomplishment—Previously we developed a technique to decouple the geometrically limited tensile island coalescence stress from the kinetically limited compressive stress generation mechanism. This technique is based on the combination of *in situ* stress measurement and through-mask electrodeposition of Ni thin films, as shown in Figure 1. By electrodeposition through a photoresist mask a periodic array of identical island was created. The resultant control over the geometry allowed the correlation of the thin film growth stages with the stress evolution.

The solid curve in Figure 2 is a typical stress evolution profile taken using this technique. As seen in the figure, during the initial stages of growth the stress was nominally zero, indicative of island growth through and over the photoresist layer prior to contacting the neighboring island. At the moment the neighboring islands contact, the systems undergoes a rapid tensile rise, which we previously demonstrated to be the result of elastic deformation of the islands towards each other. This behavior is similar to that observed during coalescence of soap bubbles, where, to minimize the total surface energy, a lower energy boundary is formed at the expense of an increase in total surface area. In the case of metal islands where shear stresses can be supported, the deformation of the island during coalescence induces a tensile stress, the magnitude of which is proportional to the difference in surface and grain boundary energy.

In the new work presented here, we used this technique to study the impact of saccharin on the island coalescence process. The dashed line in Figure 2 shows the dramatic shift in the stress evolution when saccharin was added to a Ni plating solution. As seen in the figure, the "saccharin" film immediately became compressive (negative) starting at the moment of coalescence, indicating that saccharine directly impacted the generation of stress during coalescence. In further experiments, we demonstrated that the kinetically limited compressive stress mechanism was unaffected by saccharin and that the magnitude of the compressive stress was directly dependant on the saccharin concentration in the bath. Therefore, we concluded that saccharin reduced the driving force for island coalescence by decreasing the difference in the grain boundary free surface energies. This is not to say that the coalescence stress was eliminated, rather the compressive stress mechanism became dominant when the tensile island coalescence stress was reduced by saccharin.

Significance—For nearly a half century saccharin has been added to Ni plating baths to reduce stress, but the mechanism through which this stress reduction occurred was unknown. This work provided the first direct evidence as to the fundamental mechanism active in this process and identified a previously unobserved intrinsic stress reduction mechanism.

**Brown University*

Sponsors for various phases of this work include: DOE Office of Basic Energy Sciences, Laboratory Directed Research & Development, and Brown University

Contact: Sean J. Hearne, Center for Integrated Nanotechnologies, Dept. 1132
Phone: (505) 845-0804, Fax: (505) 284-7778, Email: sjhearn@sandia.gov

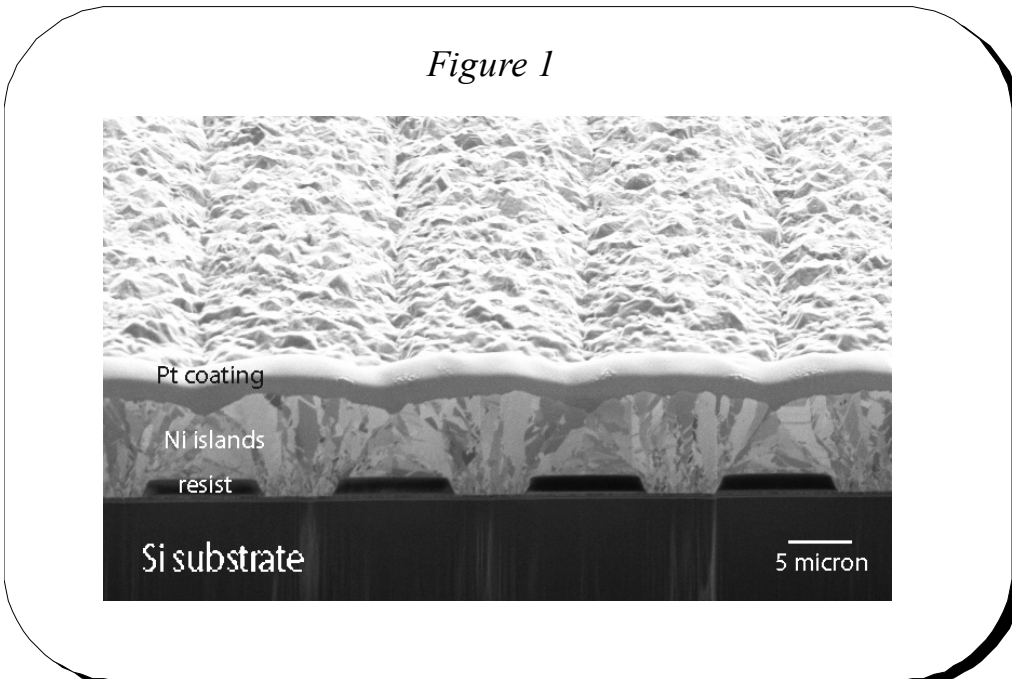

Figure 1. Obliquely viewed focused ion beam (FIB) cross-sectional image of a series of islands well after initial coalescence.

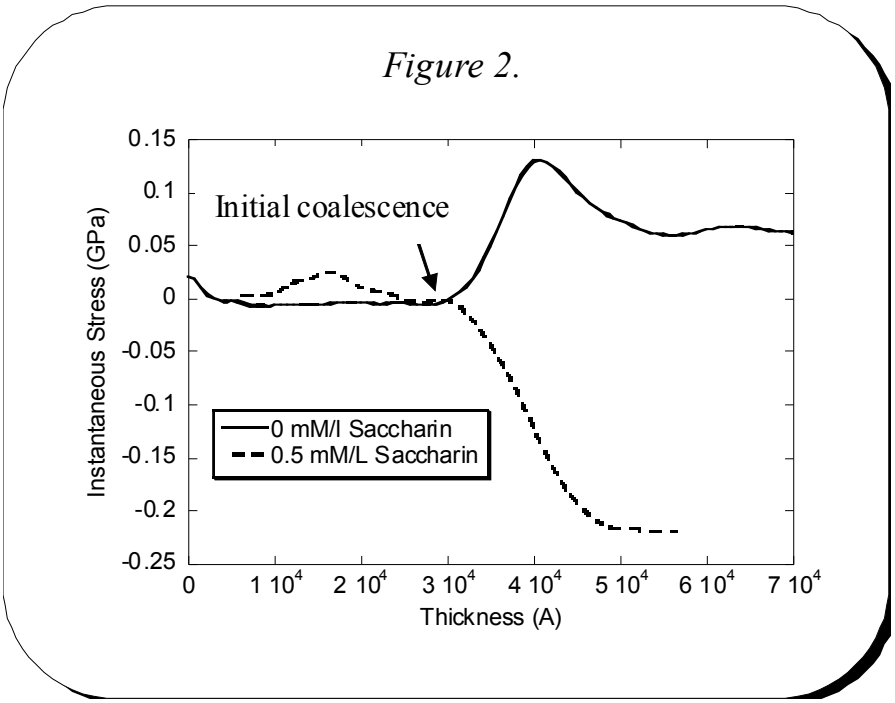

Figure 2. Stress as a function of film thickness taken during electrodeposition of the film. The arrow indicates the initial moment the islands contact in both plots. The solid curve is the Ni plated without additives and shows a strong tensile (positive) rise associated with the coalescence, whereas the dashed curve, Ni plated with saccharin, goes directly into compression with no tensile stress created during island coalescence.

Large Enhancements of Magnetic Anisotropy in Oxide-Free Iron Nanoparticles

By D. L. Huber, T. C. Monson, J. M. Lavin

Motivation—While the magnetism of isolated nanoparticles has been well understood for some time, a detailed understanding of the magnetism of nanoparticles interacting with a matrix material has been lacking. In particular, understanding the magnetic properties of nanoparticles with bound surfactants is critical for a variety of applications including such diverse areas as magnetic information storage and magnetic refrigeration.

Accomplishment—We are working with Fe nanoparticles as a model system to understand how the choice of surfactant modifies the magnetic properties of nanoparticles. Fe was chosen due to two important properties: it is both highly magnetic and extremely reactive. This allows us to easily measure the magnetic effects of chemical interactions of surfactants with the nanoparticle surface.

A recently developed synthesis that utilized beta-diketone based surfactants has been shown to produce oxide-free Fe nanoparticles with extremely high effective magnetic anisotropy. Measurements that demonstrate this are shown in Fig. 1. AC blocking temperature (the temperature where the particles direction of magnetization is able to reorient on the time scale of the experiment) measurements of 2.3 nm iron particles show a blocking temperature of approximately 20 K. Based on a calculation using the bulk anisotropy of iron, the expected blocking temperature is below 1K for particles of this size (see Fig. 2). The blocking temperatures of several sizes of particles are plotted in Fig. 2. These other sizes also exhibit the same high anisotropy, which is more than two orders of magnitude higher than the value for bulk iron.

There are a number of possible explanations for unusually high magnetic anisotropy in nanoparticles. One is surface anisotropy, where the lower coordination state of surface atoms causes excess anisotropy in the material. Another possibility is additional anisotropy caused by interparticle dipolar interactions. Both of these causes of excess anisotropy are, however, strongly size dependant. Surface anisotropy rapidly decreases with increased size due to the lower surface to volume ratio, while dipolar interactions increase greatly with increased size. Neither of these explanations are consistent with our observed constant anisotropy. It appears that the anisotropy is a material property induced by the unusual surfactant used. We are currently investigating this possibility and have observed unusual crystalline structure in these particles through X-ray diffraction. Developing an atomic level model of the structure of these particles is the subject of ongoing research.

Significance—Controlling the magnetic properties of nanoparticles has long been a goal of materials science. The technological benefits of exercising this control could be immense. For example, 2-5 nm magnetic particles could be used as bits for information storage if they were magnetically hard enough (have a high enough anisotropy). On the other hand, magnetic refrigeration requires lower anisotropy to maximize the magnetocaloric effect. Tuning the magnetic properties of the finite number of magnetic materials by varying surfactants could provide many new useful materials if it could be done in a controlled manner. This work is a step in that direction, as we have taken a famously soft magnetic material and made it a hard magnet.

Sponsors for various phases of this work include: DOE Office of Basic Energy Sciences

Contact: Dale L. Huber, Center for Integrated Nano Technologies (CINT) Science, Dept. 1132
Phone: (505) 844-9194, Fax: (505) 284-7778, Email: dlhuber@sandia.gov

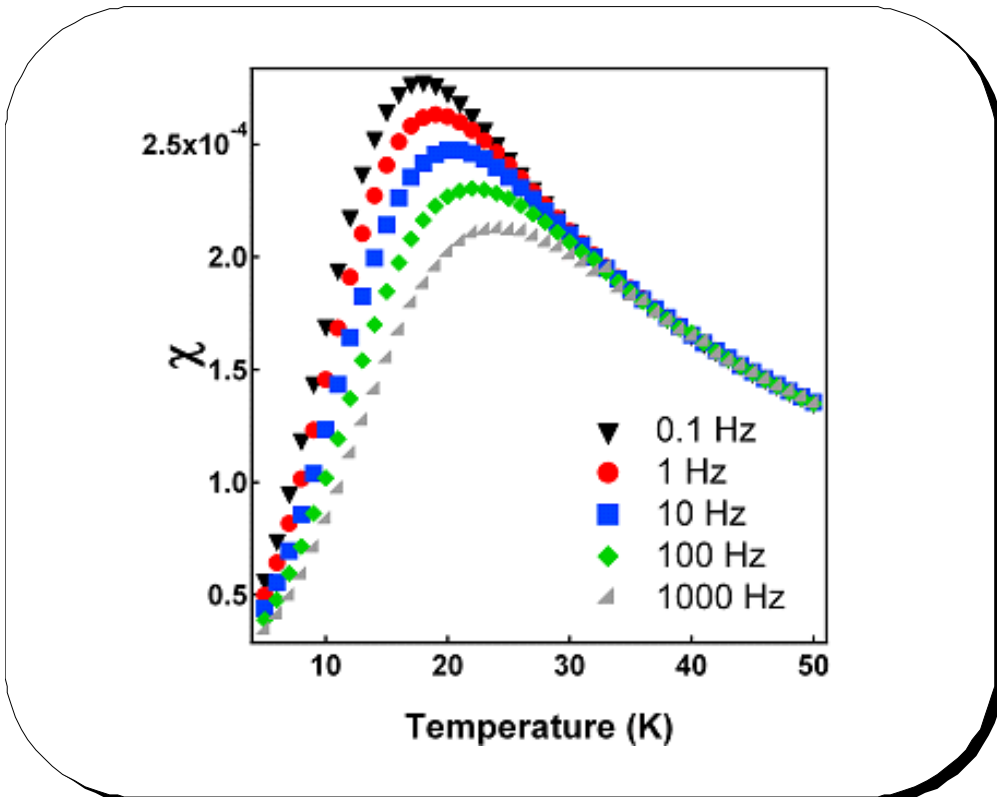

Figure 1. AC magnetic susceptibilities (χ) of a 2.3 nm diameter iron nanoparticle sample. These data are used to calculate an effective anisotropy for the nanoparticles.

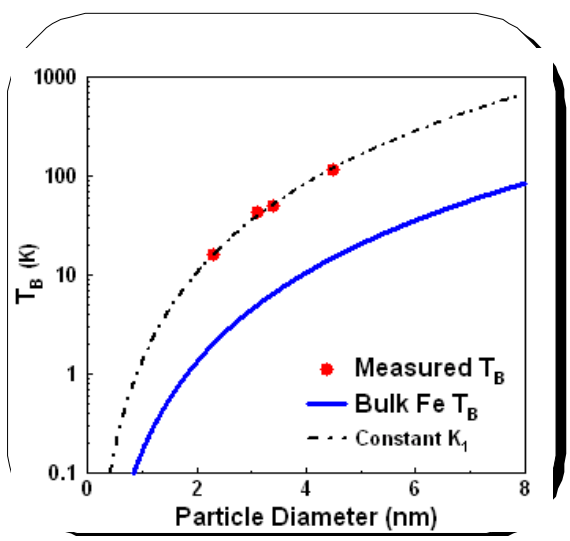

Figure 2. Plot of the measurement frequency (f) vs. $1/T_B$ for a 2.3 nm diameter iron nanoparticle sample. The data are fit with an Arrhenius function using the measured magnetic anisotropy for the nanoparticles and well-established literature values for bulk iron.

Measuring Diode Characteristics of Individual Semiconductor Nanowires

by B. S. Swartzentruber, A.A. Talin, F. Leonard, S.T. Picraux (LANL) and S.D. Hersee (UNM)

Motivation—Nanowires made from a variety of semiconducting materials are showing great promise as active elements in electronics and are being extensively characterized electrically. However, transport properties of nanoscale contacts can differ significantly from their bulk counterparts. Our goal is to understand the origin of diode characteristics at nanoscale metal-semiconductor contacts and the performance of engineered junction diodes in nanowires so that individual nanowires can be predictably and reliably integrated into unique device structures.

Accomplishment—We measured the electrical transport characteristics of two fundamentally different nanoscale diodes: the intrinsic diode formed at the metal-semiconductor interface of gold catalyst particles on Ge nanorods; and pn-diodes grown at the midpoint of GaN nanorods by switching growth conditions (doping) midway through the processing.

Using the nanomanipulator in the scanning electron microscope (SEM), we measured the diode characteristics of individual Ge nanorods as a function of diameter by contacting the gold-catalyst particle directly. A SEM image of the probe in contact with the gold particle is shown in Figure 1a. Figure 1b shows several current-voltage (I-V) spectra taken on rods with various diameters. By analyzing the slope of the forward-bias I-V curves, we find that the current is dominated by carrier recombination in the depletion region of the nanorod. Furthermore, we find that the small-bias conductance *increases* with smaller diameter, which is contrary to most models of nanowire transport. Through comparison with theoretical calculations we find that this increase in conduction is due to an increase in the depletion length with smaller diameter, which increases the total recombination current.

We also measured the diode characteristics of fabricated pn-junction diodes grown in GaN nanorods. Figure 2a shows an SEM image of the nanomanipulator probe over a GaN pn-diode nanorod. We measured the transport both through individual rods and through ensembles of ~300 rods top-contacted over a spin-on insulating layer. The light output of the ensemble LED system is shown in Figure 2b. The peak electroluminescent wavelength (not shown) was 372 nm at 30 mA, which slightly red-shifted at higher currents due to sample heating. The intrinsic diode character of the nanorods is very good, as evidenced by I-V measurements on the individual nanorods (Figure 2b inset), which exhibited very little (< 1pA) leakage current, in contrast to the rather high leakage of the ensembles. The comparison reveals that the top metallization layer on the p-side of some of the rods in the ensemble was most likely contacting the n-side leading to a parallel conductance channel.

Significance—The ability to measure transport through intrinsic diodes formed at metal-semiconductor contacts on individual nanorods and through engineered pn junctions in combination with a theoretical treatment at the nanoscale is critical to understand the transport mechanisms that prevail in nanostructures. These capabilities will enable the development of devices that integrate active nanostructures.

Sponsors for various phases of this work include: DOE Office of Basic Energy Sciences, and Laboratory Directed Research & Development

Contact: Brian S. Swartzentruber, CINT Sciences Dept. 1132
Phone: (505) 844-6393, Fax: (505) 284-7778, Email: bsswart@sandia.gov

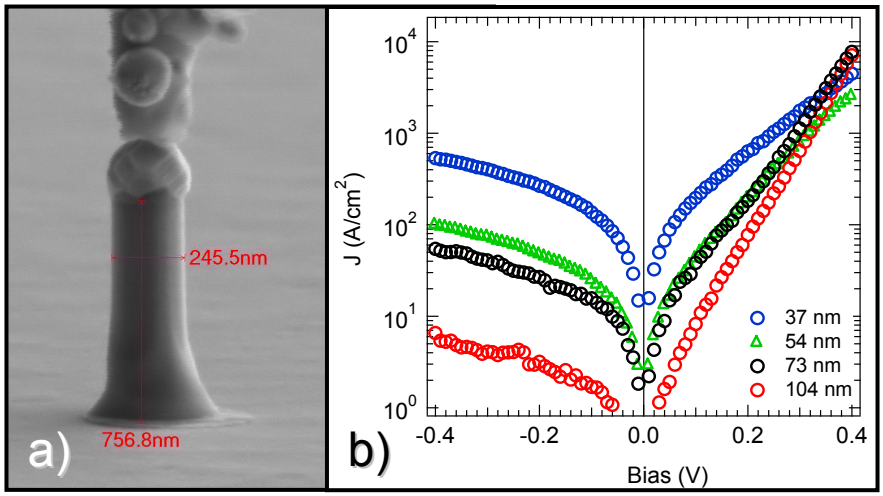

Figure 1. Conductivity of Ge nanorods. a) SEM image of tungsten probe contacting a gold catalyst particle. The nanorods grow from the bottom of the gold particle at high temperature as Ge from the vapor phase gets incorporated into the liquid gold drop and subsequently solidifies at the top of the Ge-crystal nanorod – so-called vapor-liquid-solid (VLS) growth. b) I-V spectra through Ge nanorods of various diameters showing diameter dependent electrical characteristics.

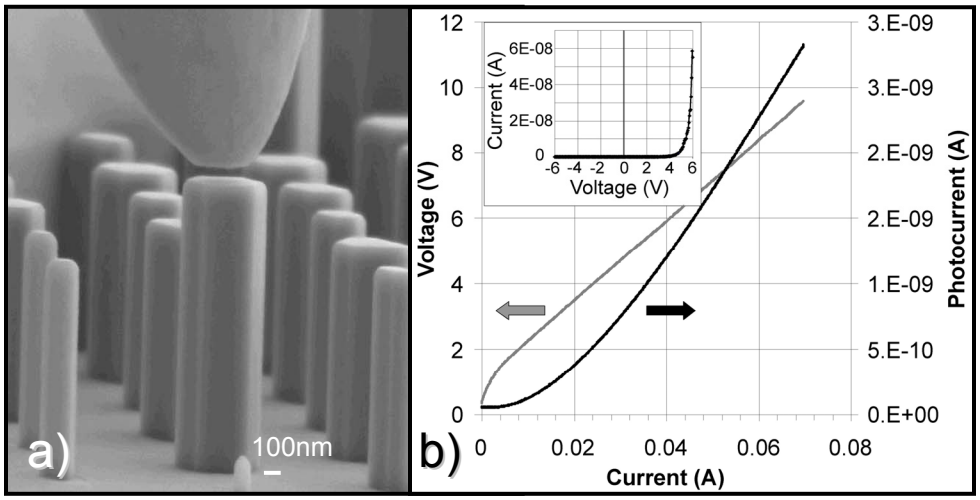

Figure 2. Electrical measurements of GaN pn-nanowire diodes. a) SEM image of a tungsten probe over a pn-nanowire diode. b) A typical L-I-V curve for a 300-nanowire LED. The electroluminescence intensity grows superlinearly over this current range. (inset: I-V curve for a single pn-nanowire diode.)

Elucidating Acid-base Behavior of Silica with *ab initio* Molecular Dynamics

by ***K. Leung, I.M.B. Nielsen, and L.J. Criscenti***

Motivation—Silanol (SiOH) groups on silica surfaces are readily deprotonated, leading to SiO^--lined water-silica interfaces ubiquitous in nanofluidics channels, biocompatible materials, and nanofabricated desalination membranes. For example, these negatively charged surfaces inside nanopores naturally repel chloride anions and can potentially remove salt from sea water. The silanol pK_a value determines its acidity, which in turn governs the surface charge at a given solution pH. A landmark surface-sensitive sum harmonic generation paper [Ong *et al*., Chem. Phys. Lett. (1992)] reveals two pK_a values: 4.5, similar to club soda, and a much less acidic 8.5 (Fig. 1a). The structural motifs associated with these pK_a's have been much speculated upon but never definitively determined.

Accomplishment—We take advantage of Sandia's massively parallel computer platforms, among the fastest in the world, and apply *ab initio* molecular dynamics (AIMD) methods with umbrella sampling to compute the pK_a of silanol groups on various crystalline surfaces. Our models include β-cristobalite (100) (unreconstructed, Fig. 2a, reconstructed, and also with a SiOH artificially replaced with SiH to break SiOH-SiOH hydrogen bonds), a $(H_3SiO)_3SiOH$ molecule, and a reconstructed quartz (0001) surface (Fig. 2b) – all immersed in liquid water. We find that most of the surface SiOH groups exhibit similar pK_a (median value ~8.4). Thus, contrary to assertions frequently made in the literature, varying the chemical connectivity (SiOH with its Si bonded to 2 versus 3 O-Si linkages) and hydrogen bonding network (whether surface silanol groups directly hydrogen bond to each other) do not yield SiOH groups that are more acidic by 4 pH units than the norm (Fig. 1b).

The lone exception is a reconstructed quartz (0001) surface. This model is designed to yield a low, 2.3 SiOH per nm^2 surface density, compared to the average experimental density of $4.6/nm^2$. This model is motivated by recent surface-sensitive vibrational spectroscopy measurements on silica and alumina, which suggest that the more acidic sites are associated with sparse hydroxyl density regions. This model quartz surface contains strained three member silica rings (Fig. 2b). Silanol groups residing on these rings exhibit a pK_a ~3 pH units lower than the median value for all other SiOH groups we have examined. *This is the only "strongly acidic" SiOH group we have found with our highly accurate and rigorous AIMD method.* Our study suggests that non-representative, strained, or defected regions on silica surfaces should be reexamined as the most promising source of low pK_a silanol groups.

Significance—As material interfaces shrink to nanometer sizes, e.g., in functionalized mesoporous silica membranes [Brinker, MRS Bulletin (2004)], novel behavior such as large shifts in silica pK_a may emerge. Our 2-year effort demonstrates that AIMD simulations conducted on Sandia's massively parallel computational platforms, with quantum chemistry input, can yield unique insights into long-standing interfacial acid-base problems. Our finding will motivate novel, nanoscale "litmus paper" experimental effort to verify the pK_a predictions. Going beyond flat interfaces, AIMD simulations will next be used investigate SiOH deprotonation inside silica nanopores, which is critical to desalination applications.

Partners: University of Ohio
Sponsors for various phases of this work include: Laboratory Directed Research & Development
Contact: Kevin Leung, Surface and Interface Sciences Department, Dept. 1114
Phone: (505) 844-1588, Fax: (505) 844-5470, Email: kleung@sandia.gov

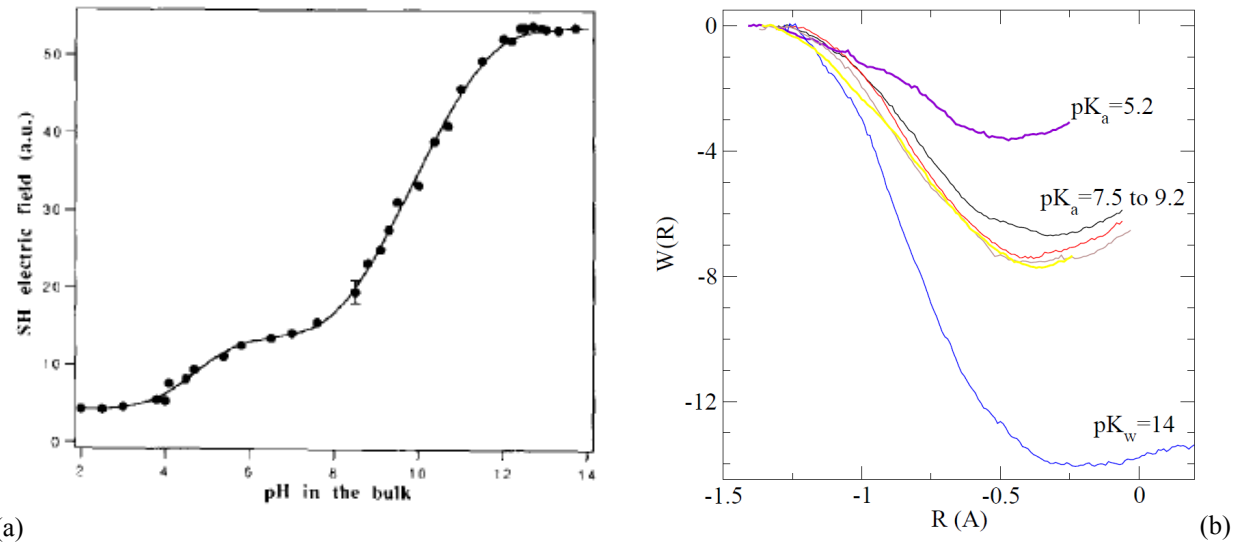

Figure 1. (a) Sum harmonic generation spectroscopy of silica surfaces, clearly indicating two pK_a values. (b) AIMD potential of mean force curves depicting the free energy changes associated with deprotonation of SiOH groups in different environments. Black & red: β-cristobalite (100); brown: reconstructed β-cristobalite (100); yellow: $(H_3Si)_3SiOH$; blue: water (reference system); violet: reconstructed quartz (0001), which alone exhibits a pK_a much lower than other silanol groups. Deprotonation proceeds in the negative "R" direction, and is almost complete at R=-1.4 A.

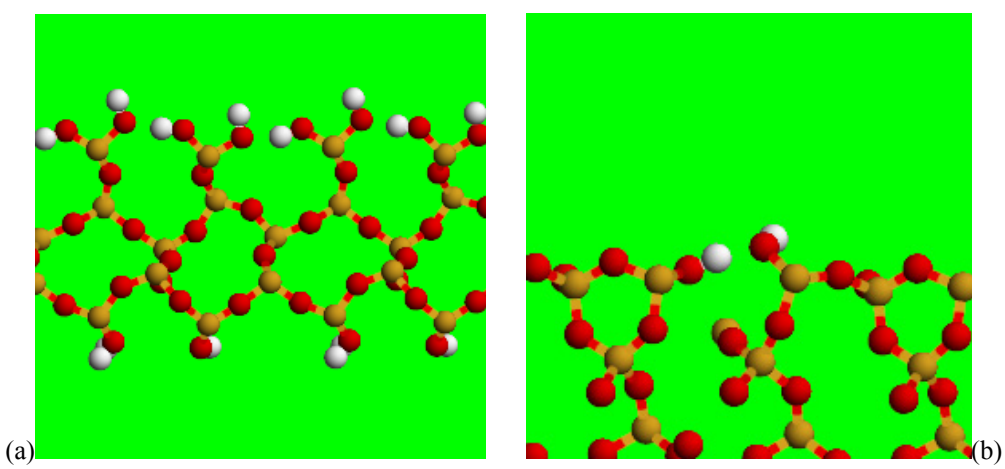

Figure 2. Side views of (a) β-cristobalite (100) surface, pK_a=7.5, 8.0 SiOH per nm^2; and (b) reconstructed quartz (0001) surface, pK_a=5.2, 2.3 SiOH per nm^2. Strained 3-member silica rings are clearly visible in the latter model. We stress that AIMD simulations are performed in the presence of liquid water at finite temperature; water molecules are omitted for clarity reasons.

Fundamental Studies

Dynamics of Entangled Polymer Melts: A Perspective from 20 Years of Molecular Dynamics Simulations*

by Gary S. Grest

Motivation—Polymer liquids display a rich and unusual viscoelastic response for time and distance scales in which ordinary liquids are Newtonian. The reason for their unusual behavior is that the motion of a polymer chain is subject to complicated topological constraints. Unlike simple molecules, the motion of long 'entangled' chain polymers are limited by the fact that they are connected to other monomers and cannot cut through each other. While there are experiments which probe the long time, macroscopic properties of polymers, few can study the molecular motion on the microscopic scale as well as molecular dynamics simulations.

Accomplishment—Twenty years ago, along with Kurt Kremer, I presented the first numerical evidence from computer simulations that the reptation model of Edwards and de Gennes correctly describes the dynamics of entangled linear polymer melts. For chains longer than what is known as the entanglement length N_e, we were the first to show that the monomers of a chain move predominantly along their own contour as illustrated in Figure 1. The distinctive signature of reptation dynamics, which we observed was that on intermediate time scales, the mean squared displacement of a monomer increases with time as $t^{1/4}$. Though limited to chains of a few N_e, previous simulations demonstrated the potential of computer simulations to contribute to our understanding of polymer dynamics but had not seen any evidence for the reptation model. Our early studies were quite limited in terms of the number of chains and length of the simulation run. However with present day computers coupled with efficient parallel molecular dynamics codes, it is now possible to follow the equilibrium dynamics of chains of length 10-20N_e from the early Rouse regime to the long time diffusive regime. Results of these new simulations support the earlier results obtained on chains of only a few N_e. Further evidence for the tube models of polymer dynamics has been obtained by identifying the primitive path mesh that characterizes the microscopic topological state of the computer-generated conformations of the chains. In particular, the plateau moduli derived on the basis of this analysis quantitatively reproduce experimental data for a wide spectrum of entangled polymer liquids including semi-dilute theta solutions of synthetic polymers, the corresponding dense melts, and solutions of semi-flexible (bio)polymers such as f-actin or suspensions of rodlike viruses. In agreement with the reptation model, the stress, end-to-end distance and entanglement length of an entangled melt subjected to uniaxial elongation, all relax on the same time scale as shown in Figure 2.

Significance—There has been considerable progress over the past twenty years in modeling the dynamics of polymer melts and networks. Numerical simulations have formed a natural bridge between experiment and analytic theory. The outlook for the future is bright as computers continue to become faster and cheaper, allowing us to access longer chains for longer times. There remain a number of outstanding challenges which numerical simulations are posed to address. These include the viscoelastic response of polymers at small strain and low shear rates, the effect of polydispersity, and the dynamics of branched and star polymers. Advanced modeling of polymers has potential impact for future Sandia needs in nuclear weapons such as polymer degradation.

* 2008 American Physical Society Aneesur Rahman Prize in Computational Physics lecture

Sponsors for various phases of this work include: Nuclear Weapons Program, and DOE Office of Basic Energy Sciences

Contact: Gary S. Grest, Surface & Interface Sciences, Dept. 1114
Phone: (505) 844-3261, Fax: (505) 844-5470, Email: gsgrest@sandia.gov

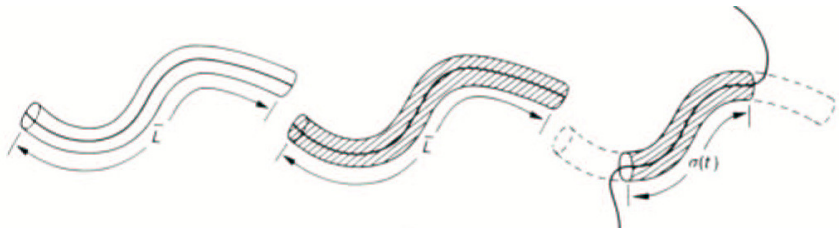

Figure 1. Illustration of the motion of a polymer in a tube formed by neighboring polymer chains

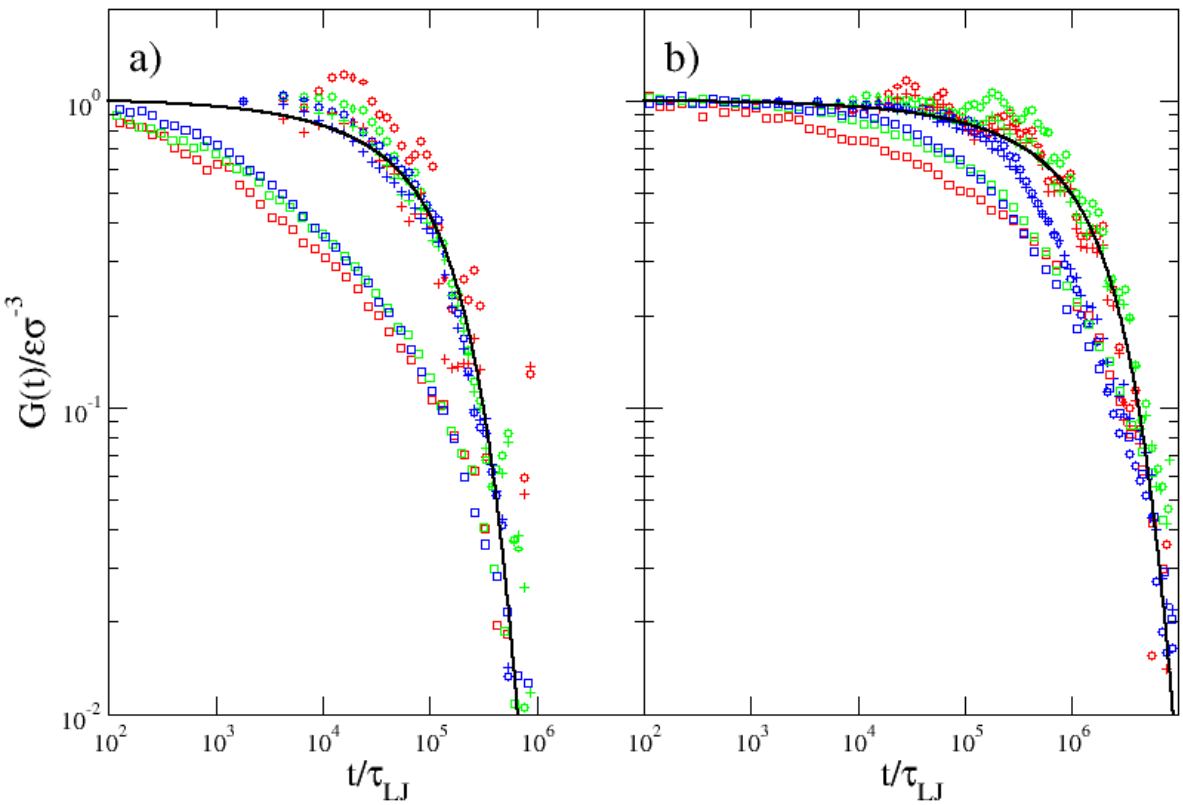

Figure 2. Stress relaxation (squares) after rapid elongation of a polymer melt by 200 % (red), 300% (green) and 400% (blue) for chain length (a) 350 and (b) 700. Also shown are the end-to-end distance (pluses) and entanglement length (circles).

Scattering in Bloch Oscillations in a One-dimensional Quantum Dot Superlattice

by **S.K. Lyo**

Motivation—One of the most fascinating phenomena in solid-state physics is the so-called Bloch oscillations (BOs) with many far-infrared device applications. In 1928, Felix Bloch (1952-Nobel Prize) proposed that electrons in a lattice undergo periodic oscillations in real as well as momentum space in a high electric field without scattering. Unfortunately, the BO period is much greater than the scattering time in natural conductors. Thus BOs have not been realized until the recent fabrication of superlattices which cause the formation of minibands and small Brillouin zones, yielding BO periods shorter than electron scattering times. It is necessary to study this in detail.

Accomplishment—We have solved two models of the Boltzmann transport equation for the nonlinear current of an electron gas in a one-dimensional miniband using a tight-binding model as a function of the time. The first model assumes a constant relaxation time for inelastic (electron-phonon) scattering, while the second model treats electron-phonon scattering exactly (*i.e.,* microscopically). An arbitrary potential for scattering from the impurities is assumed in both cases. The first model is solved analytically, yielding exact transparent results for the first time for the time-dependent current as a function of the elastic and inelastic scattering rates shown in Fig. 1(a). The results show, surprisingly, that the threshold for the onset of the BOs depends only on the elastic scattering rate but not on the inelastic scattering rate. Furthermore, the steady-state current that sets in after a time longer than the scattering time depends on the elastic and inelastic scattering rates in a very different way as shown in the I-V curve in Fig. 1(b) for a short-range impurity potential. For example, the current in the negative differential conductance (NDC) regime of the field E (> 30 V/cm) depends only on the inelastic scattering rate and the dependence is linear. Important quantities in this I-V curve are the peak current I_p and the field E_p at the peak. These quantities satisfy different scaling relationships with the elastic and inelastic scattering rates. Our result also yields an exact time development of the distribution function f(k,t) shown in Fig. 2 as a function of the wave number k. Here, f(k,t) is a Fermi-Dirac function at time t = 0, when the DC field is applied and approaches a non-equilibrium steady state at a long time t > 100 picoseconds after several BOs.

The purpose of the second microscopic model is to check the predictions of the first exact result. This model was solved by developing a purely numerical method which solves the time-dependent Boltzmann equation self-consistently to an arbitrary accuracy. This approach yields accurate numerical results but does not reveal salient underlying physics by itself. We compared the exact scaling relations for I_p and E_p obtained from the first model with these purely numerical results and found good agreement.

Significance—Our exact results yield clear insight into how the field-driven electron oscillation competes with elastic and inelastic scattering to produce BOs for the first time. The results can be used to improve the NDC properties (e.g., peak current and field) by adjusting elastic and inelastic scattering rates.

This research was performed in collaboration with Dr. D. Huang at Air Force Research Laboratory, Albuquerque, NM.

Sponsors for various phases of this work include: DOE Office of Basic Energy Sciences, and Laboratory Directed Research & Development

Contact: Ken Lyo, Semiconductor Material and Device Sciences, Dept. 1123
Phone: (505) 844-3178, Fax: (505) 844-4045, Email: sklyo@sandia.gov

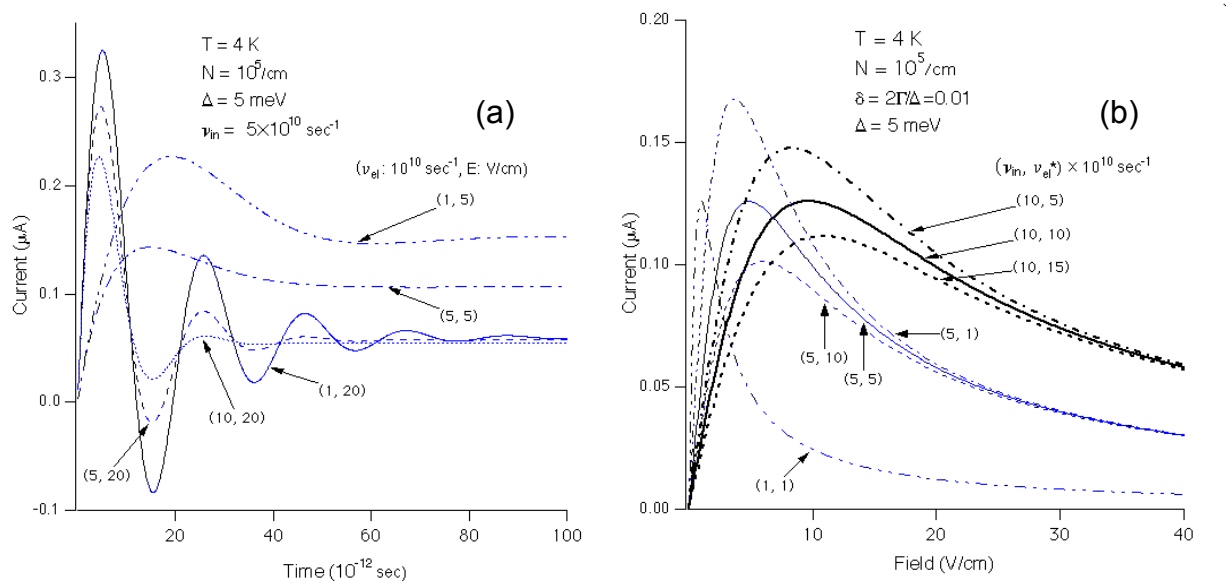

Figure 1. (a) Time-dependent currents for several sets of elastic scattering rates n_{el} and fields E for a fixed inelastic scattering rate n_{in}, band width D, electron density N, and temperature T. (b) Steady-state I-V curves for short-range impurity scattering for several sets of inelastic (n_{in}) and elastic scattering rates. The quantities G and n_{el}^* are level damping and the elastic scattering rate at the band center.

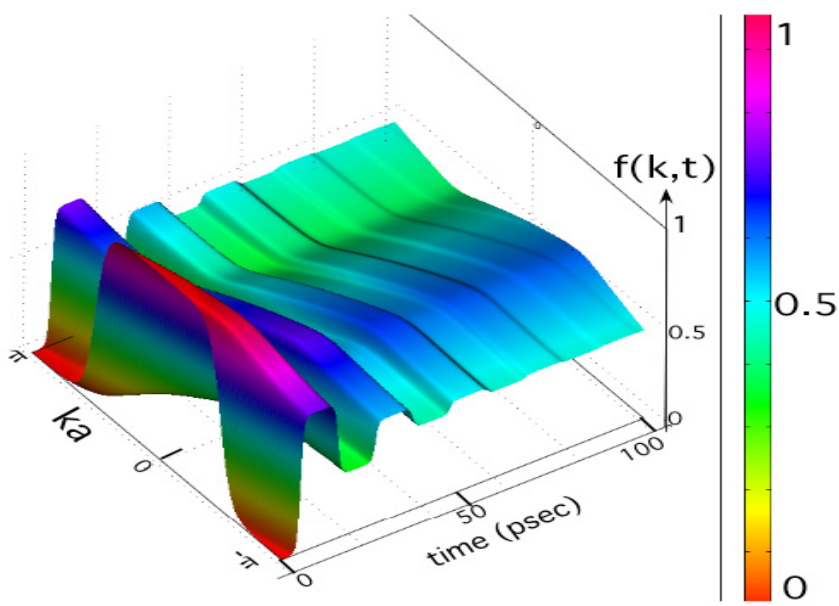

Figure 2. Time development of the distribution function f(k,t) for a one-dimensional superlattice with period a = 100 nm for an electric field E = 20 V/cm and inelastic and elastic scattering rates n_{in} = 5310^{10}/sec, n_{el} = 10^{10}/sec. Here, k is the wave number. Other parameters are the same as given in Fig. 1(a).

Coulomb Drag of Electron-hole Bilayers in the Exciton Regime

by M. P. Lilly, J. A. Seamons, C. P. Morath, and J. L. Reno

Motivation—Two-dimensional (2D) bilayers composed of electrons in one layer and holes in the other are expected to exhibit Bose-Einstein condensation (BEC) of excitons at zero magnetic field. Recent progress in quantum Hall [1] and optical [2] systems has demonstrated evidence for exciton condensation using both electrical and optical techniques. One system where exciton condensation is expected is the electrically generated 2D electron and 2D hole bilayer at zero magnetic field. Our experiments examine transport in electron-hole bilayers.

Accomplishment—We have fabricated undoped electron-hole bilayer (uEHBL) devices with separate electrical contact to each layer and performed transport measurements that reveal new physics in the strong coupling regime. A cross section of the uEHBL is shown in Figure 1a. Three devices from two different GaAs/AlGaAs heterostructures are discussed here: Sample A with a 30 nm barrier (EA1286) and Samples B and C with a 20 nm barrier (EA1287). Electron (n) and hole (p) densities are measured using the Hall resistance and adjusted independently. Here we present results for matched (n=p) density only.

Coulomb drag measurements were taken by sending a current through the electron layer while measuring the voltage induced in the hole layer (Figure 1b). The ratio of the voltage to current scaled for geometry is the drag resistivity, ρ_{DRAG}. For the larger barrier Sample A, the temperature dependence of the drag for three densities is shown in Figure 1c. As expected for Coulomb scattering in Fermi systems, the drag is approximately proportional to T^2 and lower densities result in larger ρ_{DRAG}. The red lines in Fig. 1c are T^2 best fits to ρ_{DRAG} over the range from T = 0.3 K to 10 K. Independent theory calculations [3] find excellent agreement between the data and Boltzmann transport calculations based on realistic device structures.

In Fig. 2b, the drag resistance for all three devices is shown $n = p = 8 \times 10^{10}$ cm^{-2}. The quadratic behavior of the data above 0.5 K indicates the 2D electrons and holes behave as Fermi liquids, but below 0.5 K in Sample B and Sample C a significant deviation develops. At a critical temperature the drag reaches a minimum, and for lower temperatures there is a pronounced *upturn* of the drag where ρ_{DRAG} increases with decreasing temperature. The increase in drag indicates the development of a strong coupling between the electron and hole layers, and may be caused by the formation and/or condensation of excitons in uEHBLs.

Significance—Temperature dependent Coulomb drag measurements are presented as a function of matched densities for electron hole bilayers with two different center to center separations. For the larger barrier, the drag resistance can be well described by interlayer Coulomb scattering between fermions. For the narrow barrier device, we observe an increase in the Coulomb drag as the temperature is lowered. The increased coupling suggests pairing of electrons and holes and formation of excitons in electrically generated electron-hole bilayers.

[1] J. P. Eisenstein and A. H. MacDonald, Nature **432,** 691 (2004).

[2] J. Kasprzak, *et al.*, Nature **443,** 409 (2006); R. Balili, *et al.*, Science **316,** 1007 (2007).

[3] E. H. Hwang and S. Das Sarma, Phys. Rev. B **78**, 075430 (2008).

Sponsors for various phases of this work include: DOE Office of Basic Energy Sciences, and Laboratory Directed Research & Development

Contact: Michael Lilly, Center for Integrated Nano Technologies (CINT), Dept. 1132
Phone: (505) 844-4395, Fax: (505) 284-7778, Email: mplilly@sandia.gov

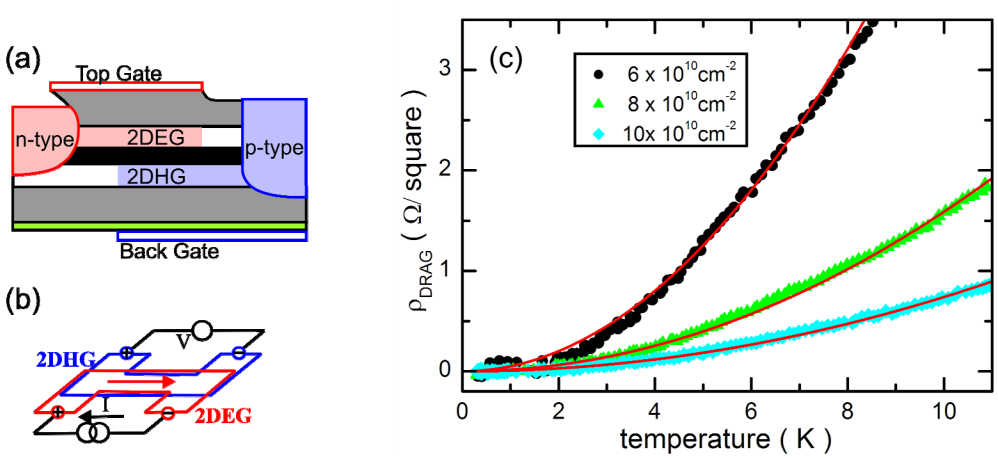

Figure 1. (a) Schematic cross section of the uEHBL sample: the conducting areas of the 2DEG (2DHG) are in red (blue), the $Al_{0.3}Ga_{0.7}As$ ($Al_{0.9}Ga_{0.1}As$) barriers are in grey (black), and an insulating SiN layer is shown in green. (b) Coulomb drag measurement where current flows in electron layer while voltage is measured in the hole layer. (c) Drag resistivity for 30 nm barrier at matched electron and hole densities is typical for Fermi systems. The red lines are T^2 best fits.

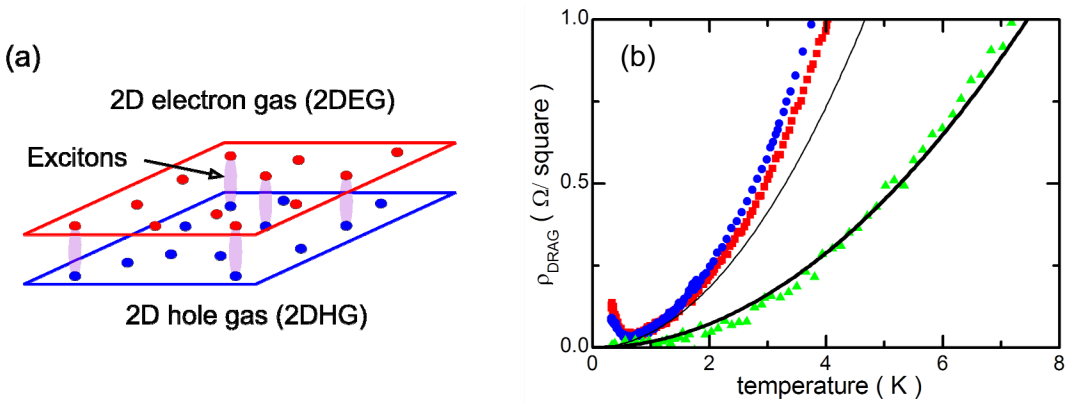

Figure 2. (a) Formation of excitons occurs as electrons and holes pair in opposite layers. (b) ρ_{DRAG} at $n = p = 8 \times 10^{10}$ cm^{-2} for three devices. Sample A, 30 nm barrier, (green triangles), Sample B, 20 nm barrier, (red squares), and Sample C, 20 nm barrier, (blue circles). The thick line is a T^2 best fit for an uEHBL with a 30 nm barrier. The thin line is the expected scaling for reducing the barrier from 30 to 20 nm.

Active Control of Surface Plasmons

*by E.A. Shaner, J.G. Cederberg, and Dan Wasserman**

Motivation—Advances in mid-infrared (mid-IR, 3-12μm) sources and the growing field of mid-IR photonics make this wavelength range very attractive for plasmonics research. Although less work has been done in this range, meshes and periodic structures utilizing surface plasmons and designed for the mid-IR have been shown to have similar properties to structures in the visible. It has also been shown that chemical attachment to the mesh surface can enhance the sensitivity of molecular absorption measurements by several orders of magnitude. Beyond applications, the mid-IR is also an interesting regime for fundamental plasmonics research as propagation lengths can be orders of magnitude longer than in the near-IR/visible.

Background—Surface plasmons (SPs) are propogating waves tied to the interface between a metal and dielectric. The SP dispersion relation is

$$k_{sp} = \frac{\omega}{c}\sqrt{\frac{\varepsilon_s \varepsilon_m}{\varepsilon_s + \varepsilon_m}}\ , (1)$$

where k_{sp} is the SP wavevector and ε_s and ε_m are the relative permittivities of the dielectric material and the metal, respectively. When photons are incident on a metal surface that is corrugated or perforated with holes, the momentum conservation for coupling to light is

$$k_{sp} = k_{xphoton} \pm \frac{2\pi}{a_o} m, k_{xphoton} = k_{photon} \sin\theta\ , (2)$$

where a_o is the period of the surface modulation, and m is a mode index. The coupling of light to SPs can lead to interesting effects. For example, a lattice of holes in a metal film can exhibit *extraordinary transmission* that causes light in specific frequency bands to transmit through the films at much higher levels than expected.

Accomplishment—While working with tuning the mid-IR transmission properties of perforated metal films (square mesh on GaAs) we have found a condition for launching a long-range SP excitation. The transmission bandpass peak of the mesh is first split by rotating the sample slightly (eq. 2). This splitting can be seen in Fig. 1a as the red trace. A 9.7 μm laser is then focused to a 50 μm spot size and the light transmitted through the mesh is spatially resolved. This is seen as the bright spot in Fig. 1a,b positioned at x=0.

The dielectric constant of the mesh substrate was tuned through heating the sample. In comparing the red traces in Fig 1a and Fig 1b, one can see a distinct shift in the bandpass spectral position (from about 1020 cm^{-1} to 1005 cm^{-1}). The striking feature in Fig. 1b is that the laser, which was propagating through the sample (out of the page) now has a tail streaking off to the left, the expected direction for SP propagation. The key result here is, with very little dielectric tuning (only a 15cm^{-1} shift in the bandpass), we are able to switch light from a transmitting mode, to a laterally propagating SP mode tied to the metal surface. As shown in Fig. 1c, the decay length for the mid-IR excitation we observed is 384 μm. This is in agreement with theory and significantly longer than propagation lengths in the near-IR (few μms).

Significance—The ability to control and direct light on chip opens up many possible applications, such as circuits that use light to transmit information as opposed to electrons. Our result is one step towards this realization and demonstrates that the mid-IR is a valuable spectral range for plasmonics research.

**UMass Lowell*

Sponsors for various phases of this work include: Laboratory Directed Research & Development, and Nuclear Weapons Program:Readiness in Technical Base & Facilities

Contact: Eric Shaner, Semiconductor Material & Device Sciences, Dept. 1123
Phone: (505) 284-5636, Fax: (505) 844-1197, Email: eashane@sandia.gov

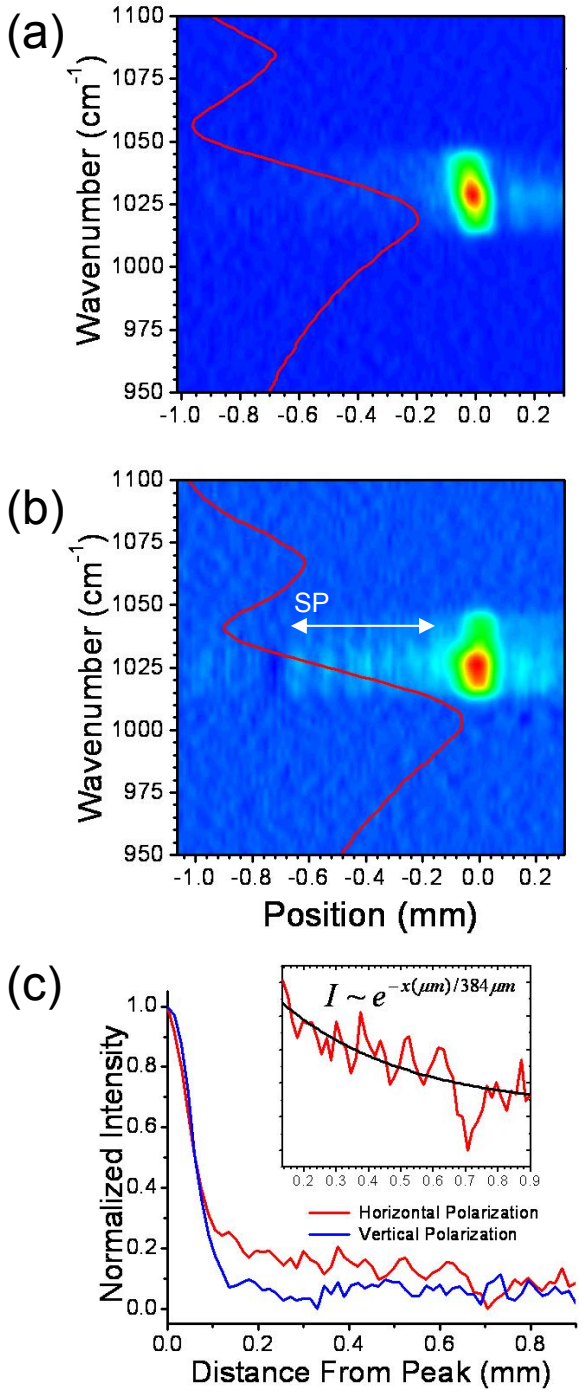

Figure 1: Spatially resolved laser excitation of a surface plasmon on a perforated metal film. The metal film on GaAs is 60nm thick and patterned with 1.4 μm holes spaced by 2.8 μm. The red trace in (a) and (b) shows the bandpass transmission characteristics of the mesh. In (a), the sample is at room temperature, while in (b), the sample is heated to 235°C in order to temperature tune the GaAs dielectric constant and shift the bandpass structure. When the 9.7 μm laser (bright spot in a,b) aligns with the bandpass peak in (a), it simply transmits through the sample. However, when it lines up on the falling edge of the bandpass, in (b), it launches a surface plasmon wave that propagates laterally on the sample surface. In (c) a comparison is made between vertically polarized light, which does not excite a surface plasmon in this geometry, and the horizontally polarized light, which does. An exponential fit was used to determine a surface plasmon decay length of 384 μm.

Recent Awards & Prizes

Recent Awards & Prizes

National and International Awards

2008 — **National Academy of Engineering (NAE):** "For development of large-scale simulations for improved understanding of metals, polymers, and particulate matter." (Gary Grest)

2005 — **American Academy of Arts and Sciences Fellow:** "For outstanding contributions in her profession." (Julia Phillips)
— **R&D100 Award:** "For the development of Ion Photon Emission Microscope (IPEM)." (Barney L. Doyle, Michael Mellon, Floyd D. McDaniel, and Paolo Rossi)

Other Awards

2008 — **American Physical Society Aneeesur Rahman Prize in computational physics:** "For ground-breaking development of computational methods and their application to the study of soft materials, including polymers, colloids, and granular systems." (Gary Grest)
— **American Physical Society George E. Pake Prize:** "For her leadership and pioneering research in materials physics for industrial and national security applications." (Julia Phillips)
— **Presidential Early Career Award for Scientists and Engineers (PECASE):** "For the combination of innovative research at the frontiers of science and technology and community service demonstrated through scientific leadership and community outreach." (Wei Pan)
— **Fellow, American Physical Society:** "For his pioneering experiments on metal-on-metal epitaxy leading to fundamental advances in understanding the structure of thin metal films, and for his exceptional service in the advocacy of nanoscience in the United States." (Robert Q. Hwang)
— **Fellow, American Association for the Advancement of Science:** "For outstanding accomplishments in chemically reacting flows and chemical vapor deposition modeling." (Michael E. Coltrin)
— **Fellow, American Association for the Advancement of Science:** "For outstanding accomplishments in semiconductor science and technology through personal research and leadership of group efforts, particularly in low dimensional physics and solid state lighting." (Jerry A. Simmons
— **Fellow, American Association for the Advancement of Science:** "For outstanding contributions to compound semiconductor research through personal research, research management, and service to the research community." (Jeffrey Y. Tsao)

2006 — **Fellow, American Physical Society:** "For investigations of, and contributions to, the science of atomic and molecular processes in plasmas through development of innovative optical, microwave, and rf diagnostics." (Greg Hebner)

2005 — **Fellow, American Physical Society:** "For experiments advancing the understanding of electron correlation and electrodynamic response in oxide superconductors, ferromagnets, Coulomb glasses and nonlinear optical polymers." (Mark Lee)

— **Materials Research Society (MRS) "Science as Art" Competition First Prize Award:** "For Garden of ZnO Nano-Yuccas." (Julia Hsu, Tom Sounart, Neil Simmons, Jim Voigt, and Jun Liu)

Sandia National Laboratories Awards

2008 — **Laboratory Directed Research & Development Award for Excellence:** "*For Ion-Neutron Simulation (INSIM)*". (Gyorgy Vizkelethy)

2007 — **Laboratory Directed Research & Development Award for Excellence:** "*For Nanolithography Directed Materials Growth and Self-Assembly.*" (Julia Hsu)

— **Laboratory Directed Research & Development Award for Excellence:** *"For Microwave to Millimeter Wave Electrodynamic Response and RF Applications of Semiconductor Quantum Nanostructures."* (Mark Lee)

2006 — **Laboratory Directed Research & Development Award for Excellence:** *"Elucidating the Mysteries of Wetting."* (Gary Grest)

Patents Awarded

2008

— Patent 7,338,590
Title: Water-Splitting using Photocatalytic Porphyrin-Nanotube Composite Devices
Originators: John A. Shelnutt, James E. Miller, Craig Medforth, Zhongchun Wang

— Patent 7,374,599
Title: Dendritic Metal Nanostructures
Originators: John Shelnutt, Yujiang Song, Eulalia Pereira, Craig Medforth

— Patent 7,376,403
Title: Terahertz Radiation Mixer
Originators: Michael C. Wanke, S. James Allen, Mark Lee

— Patent 7,420,225
Title: Direct Detector for Terahertz Radiation
Originators: Michael C. Wanke, Mark Lee, Eric A. Shaner, S. James Allen

— Patent 7,422,724
Title: Biological Preconcentrator
Originators: Ronald P. Manginell, Bruce C. Bunker, Dale L. Huber

2007

— Patent 7,223,474
Title: Heteroporphyrin Nanotubes and Composites
Originators: John A. Shelnutt, Craig J. Medforth, and Z. Wang

— Patent 7,248,397
Title: Wavelength-Doubling Optical Prametric Oscillator
Originators: Darrell J. Armstrong and Arlee v. Smith

2006

— Patent 7,148.974
Title: Method for Tracking the Location of Mobile Agents Using Stand-off Detection Technique
Originators: Susan F.A. Bender, Philip J. Jargis, Jr., Mark S. Johnson, Philip J. Rodacy, and Randal L. Schmitt

— Patent 7,132,163
Title: Hereroporphyrin Nanotubes and Composites
Originators: Jahn A. Shelnutt, Craig J. Medforth, and Z. Wang

— Patent 7,122,164
Title: Niobate-Based Octahedral Molecular Sieves
Originators: Tina M. Nenoff and May D. Nyman

— Patent 7,119,245
Title: Synthesis of an Un-supported, High-Flow ZSM-22 Zeolite Membrane
Originators: Steven G. Thoma and Tina M. Nenoff

— Patent 7,064,817
Title: A Method to Determine and Adjust the Alignment of the Transmitter and Receiver Fields of View of a LIDAR
Originators: Philip J. Hargis, Jr., Tammy D. Henson, Leslie J. Krumel, and Randal L. Schmitt

— Patent 7,041,616
Title: Enhanced Selectivity of Zeolites by Controlled Carbon Deposition
Originator: Mutlu Kartin, Tina M. Nenoff, and Steven G. Thoma

2005

— Patent 6,980,354
Title: A Self-Seeding Ring Optical Parametric Oscillator
Originator: Darrell J. Armstrong and Arlee V. Smith

— Patent 6,964,936
Title: Method of Making Maximally Dispersed Heterogeneous Catalysts
Originator: Dwight R. Jennison

— Patent 6,866,560
Title: Method for Thinning Specimen
Originator: David M. Follstaedt and Michael P. Moran

— Patent 6,844,378
Title: Method of Using Triaxial Magnetic Fields for Making Particle Structures
Originator: James E. Martin, Robert Anderson, and Rodney Williamson

Government Advisory Boards, Professional Societies, International Committees, and Journals

Government Advisory Boards

Department of Energy, Office of Basic Energy Sciences

— BES Advisory committee on Facing Our Energy Challenges in a New Era of Science; Julia Phillips, member; 2008
— Council of the BES Division of Materials Sciences & Engineering; Julia Phillips, member; 2006-2008
— BES Advisory Committee Subcommittee on Grand Challenges in BES; Julia Phillips, member; 2006-2007
— Workshop on Basic Research Needs for Solid State Lighting: Julia Phillips, Workshop Chair; Jerry Simmons, Panel Chair; Mary Crawford, Panel Member; 2006

Los Alamos National Laboratory

— Materials Capability Site Review; Julia Phillips, participant; 2008
— Materials Capability Site Review; Tina Nenoff, participant; 2007

National Academy of Engineering

— Council; Julia Phillips, member: 2008-2011
— Peer Committee, Materials Section: Julia Phillips, member, 2007-2009, Chair, 2009
— U. S. Frontiers of Engineering Program: Julia Phillips, Chair, 2005-2008; Mary Crawford, participant, 2005; George Bachand, participant 2007, Greg Hebner, Session Organizer, 2008
— Draper Prize Committee; Julia Phillips, member; 2005-2007

National Research Council

— Committee on Nanophotonics Assessability and Applicability; Jerry Simmons, member; 2006-2007
— Review Panel, National Research Council Associateship Program: Diane Peebles, Neal Shinn, and Greg Hebner, members; 2006-2009
— Committee on Benchmarking the Research Competitiveness of US Chemical Engineering; Julia Phillips, member; 2006
— Committee to Assess the Impact of the MRSEC Program; Julia Phillips, BPA liaison; 2005-2006
— Board on Chemical Sciences & Technology; Bob Hwang, member; 2004-2007
— Board on Physics and Astronomy; Julia Phillips, member; 2000-2006

New Mexico State University

— New Mexico Nanoscience Education Initiative, Advisory Board; Neal Shinn, member; 2007
— Physics Advisory Board: Neal Shinn, member, 2004-2007; Alan Wright, member 2002-2004, 2006-2008

Oak Ridge National Laboratory

— BES Chemical Sciences Site Review; Tina Nenoff, participant; 2007
— BES Site Review; Gary Kellogg, participant; 2006

Texas State University

— Materials Science & Engineering Advisory Board; Carlos Gutierrez, member; 2006-2008

Wessex Institute of technology (UK)
— Scientific Committee; Frank Van Swol, member, 2006-present

Professional Societies/International Committees/Journals

American Association for Crystal Growth
— 20th American Conference on Crystal Growth and Epitaxy; Sean Hearne, Symposium Chair; 2006, Symposium Organizer, 2009, West Program Chair 2010
— Executive Committee; Bob Biefeld, member; 2005-present

American Association for the Advancement of Science (AAAS)
— Council; Julia Phillips, member; 2003-2005
— Physics Section; Julia Phillips: Chair-elect, Chair, Past Chair; 2003-2005
— Physics Section Nominating Committee: Julia Phillips, member, 2003-2004; Chair, 2005

American Chemical Society (ACS)
— Committee on Science; Tina Nenoff, associate; 2007
— COLL Division; Tina Nenoff, councilor; 2006-2008

American Physical Society (APS)
— March Meeting Program Committee, Workshop on Energy for Young Physicists; Julia Hsu, member; 2008
— Aneesur Rahman Prize Committee; Gary Grest, member; 2008,
— George E. Pake Prize Committee; Julia Phillips, member; 2008
— McGroddy Prize Committee; Julia Hsu, member; 2007-2008
— March Meeting Focused Session; Julia Hsu, organizer; 2007
— Division of Condensed Matter Physics (DCMP): Julia Phillips, Vice-Chair, 2005; Chair-Elect, 2006; Chair, 2007; Past Chair, 2008
— Forum on Industrial & Applied Physics (FIAP): Mark Lee, Vice-Chair, 2005; Chair-Elect, 2006; Chair, 2007
— Committee on Minorities; Carlos Gutierrez, Chair; 2006
— Bouchet Prize Committee; Carlos Gutierrez, member; 2005-2006
— Division of Materials Physics (DMP) Executive Committee; Julia Hsu, member-at-large; 2004-2006
— Committee on Meetings; Mark Lee, member; 2003-2006

American Vacuum Society (AVS)
— Neal Shinn, President; 2007
— 53rd International Symposium; Neal Shinn, Vice Chair; 2006
— Distinguished Lecture Series Committee; Neal Shinn, Chair; 2004-2006
— Board of Directors; Neal Shinn, member; 2003-2006

ASM International – The Materials Information Society
— Events Committee; Dan Barton, member; 2003-present
— Electronic Device Failure Analysis Society (EDFAS): Dan Barton, Board of Directors member, 1998-present; Vice-President, 2005

Chemistry of Materials
— Editorial Board; Tina Nenoff, member; 2006-2009

Conference on Magnetism and Magnetic Materials
— Scientific Advisory Board; Carlos Gutierrez, member; 2005-2007

Electrochemical Society
— Symposium; Nancy Missert, organizer; 2006, 2007
— Corrosion Division, Nancy Missert: Student Travel Grant Coordinator, 2005-2008; executive committee member, 2006-present
— Nash Miller Award Committee; Nancy Missert, member; 2005
— Individual Membership Committee; Nancy Missert, member; 2003-2006

Fifteenth International Conference on Crystal Growth
— Bob Biefeld, Program Co-Chair; 2006-2007

Gaseous Electronics Conference (GEC)
— 56th Annual Meeting; Greg Hebner: Chair-elect, Chair, Past Chair; 2003-2006

Gordon Conference
— Zeolite Gordon Conference; Tina Nenoff, Vice-Chair; 2008

Institute of Electrical and Electronics Engineers (IEEE)
— *Transactions on Plasma Science*, 4th issue on Images in Plasma Science; Greg Hebner, guest editor; 2004-2005
— *Transactions on Device and Materials Reliability (TDMR)*; Dan Barton, guest editor; 2002-present
— International Reliability Physics Symposium, Management Committee; Dan Barton, member; 2001-present

International Conference on Applications of Accelerators in Research and Industry
— Barney L. Doyle, Chairman; 2004, 2006, 2008

International Conference on Defects in Semiconductors
— International Advisory Board, Alan Wright,: Co-organizer, 2005-2007, Co-Chair, 2007

International Conference on Electrorheological Fluids and Magnetorheological Suspentions
— James E. Martin, program committee; 2001-2009

International Conference on Ion Beam Analysis
— Barney Doyle, Gyorgy Vizkelethy; International Committee, 2008

International Conference on Low Energy Electron Microscopy/Photoemission Electron Microscopy (LEEM/PEEM)
— International Advisory Committee; Gary L. Kellogg, member; 2000-present

International Conference on Nuclear Microprobe Technology and Applications
— International Committee; Gyorgy Vizkelethy; Internaitol Committee, 2008

International Conference on Particle-Induced X-Ray Emission and its Analytical Applications
— International Committee; Barney L. Doyle, member; 2005

International Conference (4th) on Porphyrins and Phthalocyanines
— Symposium; John Shelnutt, Organizer and Chair; 2004, 2006, 2008

International Electron Devices Meeting
— Session; Tom Friedmann, organizer; 2007

International Journal of PIXE (IJPIXE)
— Editorial Board, Barney Doyle; 1996-present

International Union for Vacuum Science, Technique, and Applications (IUVSTA)
— 17th International Vacuum Congress; Neal Shinn, Program Committee member; 2007
— Surface Science Electoral College, Neal Shinn, Unisted States Representative; 2001-2007
— Surface Science Division: Neal Shinn, Chair, 2004-2007; Secretary, 2001-2004

International Zeolite Association (IZA)
— Commission on Synthesis Committee; Tina Nenoff, member; 2004-2007

Journal of Chemical Physics
— Editorial Board; Jim Martin, member; 2003-2006

Journal of Crystal Growth
— *Journal of Crystal Growth* for subject areas: "Epitaxial Growth and Nanostructures"; Bob Biefeld, Associate Editor; 2004-present

Journal of Materials Research
— Editorial Advisory Board; Julia Phillips, member; 2004-present; chair; 2008-present

Lawrence Berkeley National Laboratory
— Accelerator Fusion Research Department Review; Barney Doyle, 2006-2007

Materials Research Society (MRS)
— Surface Electron Microscopy Symposium; Gary Kellogg, lead organizer; Spring 2008
— Information Services Committee; Sean Hearne, Chair; 2007
— Operational Oversight Committee; Julia Hsu, Treasurer and member; 2006-2007
— *MRS Bulletin*: H_2 Production; Tina Nenoff, co-editor; October 2006
— Symposium Organizers: Neal Shinn and John Sullivan, organizers; Spring 2006; Barney Doyle, organizer, Fall 2005;

— Meeting Chair: Julia Hsu, Fall 2007
— Board of Directors: Julia Hsu, member, 2005-2007
— Technical Program Committee; Julia Phillips, Chair; 2005-2008
— Web Advisory Sub-Committee: Sean Hearne, member, 2005-2006; Chair, 2006
— Electronic Services Task Force: Sean Hearne, member; 2005
— Membership Committee: Sean Hearne, member, 2004-2008
— Information Services Committee: Sean Hearne, Chair 2006-2008
— JMR Editor-in-Chief Search Committee: Sean Hearne, Chair, 2008

Microelectronics Reliability (Elsevier Journal)
— Editorial Advisory Board; Dan Barton, member; 2000-present

National Association of Corrosion Engineers
— H.H. Uhlig Educator Award Committee; Nancy Missert, 2006-2008

Nuclear Instruments and Methods in Physics Research, Section B: Beam Interactions with Materials and Atoms
— Editorial Board; Barney Doyle, member; 2003-2006

Pacifichem (Honolulu)
— Symposium; John Shelnutt, organizer and Chair; 2005

Physical Review E
— Gary Grest, Senior Editor; 2002-present

Solid State Communications
— Julia Hsu, Editorial Board; 2005-present

The Minerals, Metals, and Materials Society (TMS)
— Electronic Materials Conference: Nanoscale Characterization, Zinc Oxide, and Organic/Hybrid Photovoltaics Symposium; Julia Hsu, organizer; 2007
— Electronic Materials Committee: Bob Biefeld, member, 2002-present; secretary, 2002-2004; Vice Chair, 2005-2007; Chair, 2007-2009; Past Chair, 2009-2011; Julia Hsu, member, 2000-2006
— Symposium; Sean Hearne, organizer; March 2004

US Organometallic Vapor Phase Epitaxy Workshop
— Organizing Committee; Bob Biefeld, member; 1991-present

World Scientific Publishing Company (WSPC)
— Editorial Board, “Reviews of Accelerator Science and Technology”; Barney Doyle, 2007-2008

Resources & Capabilities

— Diagnostics and Characterization —

Atomic-Level Imaging and Spectroscopy
We have developed technical capabilities in the following areas:

- Scanning Tunneling Microscopy (STM) with the ability to track the diffusion of single atoms on surfaces
- Low Energy Electron Microscopy (LEEM) with nanometer spatial resolution and real-time spectroscopic imaging capability at sample temperatures from 300K to over 1000K
- Field Ion Microscopy (FIM) with single atom resolution and accurate temperature control to 1 Kelvin,
- Atom Probe Microscopy (APM) with pulsed laser desorption capability
- Interfacial Force Microscopy (IFM), with feedback for accurate, simultaneous normal and frictional force profile measurements for the quantitative study of adhesion, tribology, nanomechanics, and the mechanical assessment of microsystem components
- Atomic Force Microscopy (AFM) for imaging, force profiling, and manipulation of individual biomolecules in fulid environments with simultaneous fluorescence detection
- Piezo Force Microscopy (PFM) for measuring piezoelectric coefficient, imaging ferroelectric domains, and spatial variation in piezoelectric properties, and input

Chemical Vapor Deposition (CVD)
Sandia will provide experimental tools for investigating CVD which include optical probes (such as reflectance-difference spectroscopy) for gas phase and surface processes, a range of surface analytic techniques, molecular beam methods for gas/surface kinetics, and flow visualization techniques. These tools are also integrated in a unique manner with research CVD reactors and with advanced chemistry and fluid models.

Electrochemical Scanning Probe Microscopy
We have developed the ability to study nanoscale changes at surfaces during oxidation and dissolution of metal surfaces under electrochemical control using scanning tunneling microscopy. These studies can be performed in a variety of electrolytes in order to determine the mechanisms governing passive film growth.

Growth Science Laboratory
Sandia has capabilities for in-situ characterization of materials during thin film deposition, molecular beam epitaxial growth, and low energy ion beam simulated growth, using intensity profile sensitive reflection high energy electron diffraction (RHEED) for surface structure, x-ray reflectometry for in-situ surface and interface structure, multibeam wafer curvature for strain (Patent #5,912, 738), and Auger electron spectroscopy for surface composition.

Ion Accelerator Nuclear Microprobe
Sandia will provide energy >4 MeV, nuclear microscopy and radiation effects microscopy. This 6 MV tandem accelerator generates ion species from hydrogen to gold for both radiation effects research and quantitative ion beam analysis of materials containing light elements (hydrogen to fluorine) using heavy ion elastic recoil detection (ERD) and heavy elements using high-energy back scattering spectrometry. An external Micro Ion Beam Analysis (X-MIBA) capability enables multi-elemental analysis and ion irradiation of samples, which are vacuum incompatible or extraordinarily large. The Sandia Nuclear Microprobe with submicrometer size high-energy ion beams is used to study materials and devices. Special emphasis is given to the evaluation of the radiation hardness of

microelectronic devices using three new advanced diagnostic techniques invented at Sandia: Single-Event-Upset Imaging, Ion-Beamed-Induced-Charge Collection Imaging (IBICC), and time-resolved IBICC. We have also developed the Ion Electron Emission Microscope (U. S. Patent No. 6,291,823 and 2001 R&D-100 Award winner), which can perform radiation microscopy using very highly ionizing particles without focusing the ion beam. A recent extension of this microscope is a desktop version that uses an alpha radiation source, called the Ion Photon Emission Microscope (which also received an R&D 100 Award in 2005).

KMAP X-ray Diffractometer

Based on double crystal x-ray diffractometry in combination with position sensitive x-ray detection, our KMAP x-ray diffraction analysis is used to determine the lattice constant, strain relaxation, composition, layer orientation, and mosaic spread for a large variety of advanced epitaxial semiconductor materials.

Lasers and Optical Spectroscopies

Sandia has capabilities in characterizing semiconductor materials by photoluminescence and magnetoluminescence down to low temperatures by optical laser imaging and laser microscopy, by laser excitation spectroscopy, and by the time-resolved measurements of optical emission. We also have developed a high lateral resolution, near-field scanning optical microscopy (NSOM) capability with time and frequency resolution. Sandia also has capabilities in gas phase spectroscopy using pulsed and CW laser sources covering the range from microwave frequencies, THz and thorough the deep UV.

Lasers and Optics

We provide characterization and advanced understanding in the area of solid-state lasers and non-linear optics, especially as coherent sources of broadly tunable light in rugged, compact geometries. We also have established expertise in long-term and transient radiation effects characterization of optical materials. Capabilities include the widely used (approximately 2000 users worldwide) SNLO (Sandia Non-Linear Optics) code, which is a lab-tested code for predicting the performance of non-linear optical components. In the area of integrated optical materials, our laboratories produce new types of photosensitive materials (processing patent applied for) for directly-writeable waveguides and reconfigurable optical interconnects.

Low-Temperature Plasma Analysis

We have state-of-the-art capabilities for the analysis of low-temperature plasmas as found in commercial processing reactors. These include emission spectroscopy, electrical characterization, laser and microwave-based measurements of species concentrations, *in situ* electric field measurements, and others. Sandia is the only lab that combines new diagnostics, relevant process chemistries (complex mixtures), and massively parallel (MP) computer models for simulation of continuous and transient plasmas. We also have strengths in plasma – surface interactions, plasma enhanced catalisis and plasma surface modification using plasma sources.

Quantum optics and cold matter physics

Sandia has capabilities in quantum optics and cold matter physics. This includes Bose Einstein condensates, trapped ion for applications to quantum computing and entangled state photon systems for improved remote sensing systems.

Remote Sensing
Sandia has extensive capabilities related to laser based remote detection of materials. We have established and field tested systems that are mounted in trailers, vans and flexible air craft platforms. These systems are flexible and portable spectroscopy systems that find a wide range of applications including WMD detection and topology characterization.

Materials Microcharacterization
Our capabilities in this area include optical microscopy, scanning, electron microscopy, analytical transmission electron microscopy, double crystal x-ray diffraction, ion beam analysis of materials (RBS, channeling, ERD, PIXE, NRA), Hall measurements, microcalorimetry, photoluminescence, light scattering, electronic transport, deep level spectroscopy, magnetization, and dielectric and magnetic susceptibilities.

MEMS-based Tensile Testing
We have developed the capability to perform pure uni-axial loading of metal MEMBS test structure *in situ* and ex situ of a TEM. The technique has been demonstrated using Al, Ni and Cu, but is applicable to a wide range of other materials.

Nanoelectronics Laboratory
Sandia has capabilities for fabrication of nanoscale quantum device structures together with capabilities for ultra-low noise measurement of transport form 0.3 Kelvin to ambient at high magnetic fields.

Scanning Cathodoluminescence Microscopy
We have developed the ability to measure and image cathodoluminescence from insulators and semiconductors on the submicron scale in order to understand how defects influence the emission of light from the ultraviolet to the visible. Individual spectra are also obtained at controlled locations in order to identify heterogeneities.
Scanning Probe Metrology
We have developed a unique wide-field scanning Interfacial Force Microscope with calibrated force detection for the dynamic measurement of normal and lateral forces of micro-electrical-mechanical system components in operation**.**

Simultaneous Measurement of H, D, and T in Materials
We have designed and implemented a new ion beam analysis (IBA) system to simultaneously measure the absolute quantities of H, D, and T in materials using an elastic recoil detection (ERD) technique. The technique uses an E-dE detector arrangement, or particle telescope, to provide for accurate separation of the H, D, and T signals. The system can also simultaneously acquire information about medium and high Z elements in the sample using Rutherford backscattering spectrometry (RBS). Measurement of other light elements is possible using the nuclear reaction analysis (NRA) technique, which is isotope specific. The system will have an accuracy of $< 2\%$ for measuring the composition of solids.

Zeolite and Nanomaterials Analytical Lab
The Zeolite and Nanomaterials Analytical Lab has a suite of instrumentation relevant for the characterization or analysis of a wide array of novel zeolite, complex oxide or nanoparticulate materials for project research applications. The lab houses characterization equipment including a Siemens x-ray diffractometer (XRD), a Fourier transform infrared spectroscopy (FTIR) system, a Temperature Programmed Desorption (TPD) system, a Brunauer, Emmett and Teller (BET) system, and Thermogravimetric Analysis (TGA) instruments.

— Synthesis and Processing —

We apply our facilities and personnel expertise for synthesis and processing of novel materials requiring higher accuracies, or greater understanding of the link between process and performance, than normal. These facilities and expertise range from chemical processes such as chemical vapor deposition to physical processes such as pulsed laser deposition to complex multi-phenomena processes such as ECR plasma deposition and etching. Our technical capabilities include:

400 keV and 180 keV Ion Implanters
These systems are equipped with a variety of sources (gas, sputter, and metal vapor). This facility provides ion species from hydrogen to bismuth that can be used for studying fundamental irradiation mechanisms and selective chemical doping in semiconductors, metals, ferroelectrics and superconductors. The 180 keV Implanter is capable of both ambient and high temperature implants up to 600°C and ion currents up to 50 micro-A.

Crystal and Thin Film Growth
Capabilities in this area include a pulsed laser deposition chamber, a thin film oxide deposition chamber, a diamond-like carbon deposition chamber, a hot filament, chemical vapor deposition chamber, and various apparatus for single crystal growth. Our capabilities for stress relief of diamond-like carbon films and structures produced by pulsed laser deposition are not available elsewhere.

Electron Cyclotron Resonance (ECR)
This plasma facility has been built for studying fundamental processes governing the growth of oxide and nitride dielectric films used in optoelectronics and used as hard coatings. This is the only system in the U. S., that combines ECR plus e-beam evaporation.

Metal-Organic Chemical Vapor Deposition (MOCVD)
We maintain research facilities with capabilities in MOCVD of compound semiconductor materials. These capabilities include research reactors designed specifically for studies of CVD chemistry, fluid dynamics, the development of advanced in-situ diagnostics, and the development of advanced semiconductor heterostructures and devices. We also investigate the synthesis and properties of a variety of nanostructures including quantum dots and nanowires using MOCVD.

Molecular Beam Epitaxy (MBE)
We have research semiconductor growth laboratories for ultra-pure and ultra-flexible MBE growth of III-V materials

Monolayer Deposition of Organic Films
We have a Langmuir-Blodgett facility for controlled deposition of mono- and multi-layer organic films. The facility includes two computer-controlled troughs, in situ fluorescence microscopy, vibration isolation, and a dust-free down flow work area. These combined capabilities are not available in the private sector.

Nanocluster Laboratory
We have developed numerous processes for the synthesis of large quantities of monodisperse particles and clusters of metals, semiconductors, and oxides.

Soft Nanolithography
Soft nanolithography refers to patterning techniques that complement UV and electron beam lithography. These approaches avoid the chemical and radiation exposure often used in conventional lithography processing, making soft nanolithography particularly useful for bio, organic, and molecular materials. Current capabilities include micro-contact printing, nano-transfer printing, and dip-pen nanolithography.

Stress Evolution During Electrodeposition
We have developed the capability to measure stress evolution during thin film electrodeposition and have used it to measure stress during patterned and unpatterned film growth. Our studies range from fundamental mechanisms that create stress during island coalescence to materials-specific systems, such as electrodeposited Ni, Cu, Sn, Ag and their alloys.

Synthetic Organic Laboratory
Novel lipids, surfactants, and other small molecules are prepared in this laboratory via synthetic organic techniques. The laboratory is also capable of forming and characterizing self-organized structures (e.g., liposomes, micelles, self-assembled monolayers, LB films) generated with the newly synthesized molecules in pure or mixed molecular systems.

Zeolite and Nanomaterials Chemical Synthesis Laboratory
The primary work in this lab involves the production and synthesis of novel materials via standard chemical processing for research applications for relevant projects. In addition to needed chemical materials stock, the lab includes standard laboratory equipment including fume hoods, pH meters, filtration devices, small tube furnaces, synthetic glassware, ovens, and stir plates.

— Theory and Simulation —

Our capabilities in theory and simulation can be applied toward understanding of the synthesis and properties of new materials and/or structures. They are particularly valuable for understanding how to tailor or tune properties for specific applications. The technical capabilities include:

Chemical Processes
We have extensive capabilities, including massively parallel computation, to model complex chemically reacting flows that occur in chemical vapor deposition manufacturing processes. Our numerical simulations can include the coupled gas-phase and gas-surface chemistry, fluid dynamics, heat, and mass transfer to provide predictive models of a chemical process.

Complex System Analysis
We have developed a suite of tools to manage complex data collections and process them to produce user defined information. One key advantage of our approach is that the user employs high-level interactions to process the data and is freed from traditional programming language constructs.

Electronic Structure and Linear Scaling
We have developed state-of-the-art massively parallel electronic structure algorithms, based on ab initio pseudopotentials and plane-wave/Gaussian basis functions. These codes are used to develop a fundamental understanding of physical phenomena and materials, including compound semiconductor band structure, diffusion of point defects, dopants and impurities, optoelectronic properties of extended defects, adsorbate interactions on surfaces, bonding at metal-oxide interfaces, and enhanced reactivity of nanoparticles. To allow the investigation of more complex systems and phenomena, we have developed new computationally efficient algorithms, e.g., self-consistent linear scaling density functional theory, and variable and real-space gridding.

Low-Temperature Plasmas
We have extensive capabilities in massively parallel codes to simulate the time and space evolution of low-temperature plasmas, focusing on new theoretical techniques for achieving rapid convergence and on direct comparisons with experimental results.

Molecular Dynamics Simulation
Large scale, classical molecular dynamics simulations using the massively-parallel code LAMMPS (Large-scale Atomic/Molecular Massively Parallel Simulator) are being used to model a wide variety of systems. These classical simulations cover the length and time scale intermediate between quantum and continuum calculations. Systems of current interest include adhesion and friction in self-assembled monolayers, degradation of polymer adhesives, wetting and spreading of multi-component fluids and transport in polymer membranes for fuel cells. Modifications of the algorithm to include particle rotation and friction have been implemented to study granular materials.

Optical and Wave Propagation
We have developed advanced simulation codes for understanding wave propagation in optical parametric oscillators and amplifiers for the purpose of designing highly efficient, tunable laser sources. We also have capabilities in novel optical designs, including resonators for compact laser geometries. These capabilities are coupled to in-house micro-optics construction facilities and state-of-the-art optics testing.

Physical, Chemical and Nano Sciences Center FY08 Budget - by Customer

Operating ($47.3M)

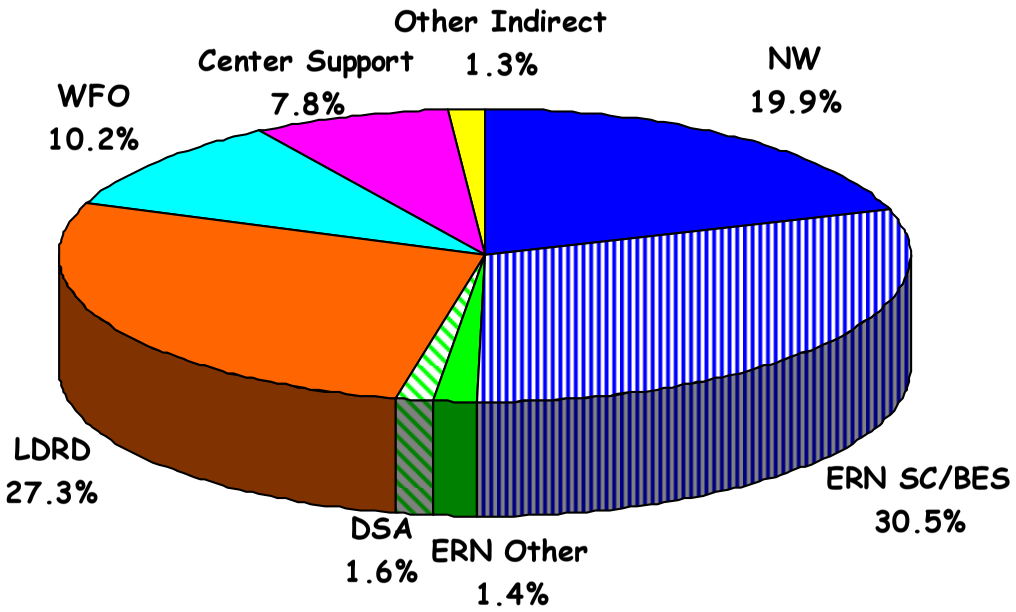

Capital ($3.1M)

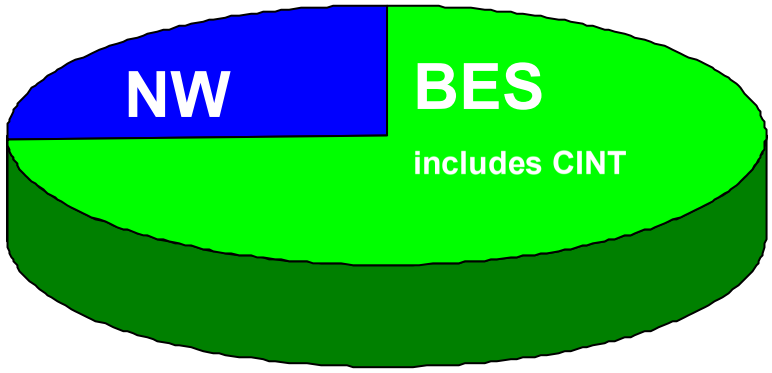

NW	Nuclear Weapons	ERN	Energy, Resources & Nonproliferation	WFO	Work for Others (includes WFOs in ERN,DSA,HSD)
DSA	Defense Systems & Assessments	SC/BES	Office of Science/Basic Energy Sciences	LDRD	Laboratory Directed Research & Development

Glossary of Acronyms

AC	Alternating Current (variable polarity) (pg. 52)
AF	Annealing Factor (pg. 8)
AFM	Atomic Force Microscope (pg. 32)
AIMD	*ab intitio* Molecular Dynamics (pg. 56)
APD	Avalanche Photodiode (pg. 26)
ASC	Advanced Simulation & Computing (pg. 7)
BEC	Bose-Einstein Condensation (pg. 64)
BJT	Bipolar-junction Transistors (pgs. 6, 12)
BO	Bloch Oscillations (pg. 62)
CCD	Charge Coupled Device (pg. 18)
CINT	Center for Integrated Nano Technologies (p. 52 & 64)
CL	Cathodluminescence (pg. 22)
CVD	Chemical Vapor Deposition (pg. 48)
DC	Direct Current (pg. 48, 62)
DFT	Density-Functional Theory (pg. 6)
DLOS-	Deep Level Optical Spectroscopy (pg 38)
DLTS	Deep Level Transient Spectroscopy (pgs. 6, 8, 14)
FIB	Focused Ion Beam (p. 51)
FSCRS	Field Structured Chemiresistors (pg. 42)
GSGG	Gadolinium Scandium Gallium Garnet (pg. 20)
IBL	Ion Beam Laboratory (pgs. 6, 10)
IC	Integrated Circuit (pg. 22)
ICCD	Intensified Charge Coupled Device (pg. 18)
IPEM	Ion-photon Emission Microscopy (pg. 22)
IR	Infrared (pg. 38, 66)
IVs	Interstitals & Vacancies (pg. 11)
LED	Light Emitting Diodes (pgs. 30, 32, 34, 46, 54)
LIDAR	Light Detection and Ranging (pg. 26)
MEMS	MicroElectro Mechanical Systems (pg. 48)
MOCVD	Metal-organic Chemical Vapor Deposition (pg. 22, 30, 36, 38)
MQW	Mulitple Quantum Well (pg. 22)
NDC	Negative Differential Conductance (pg. 62)
NW	Nanowire (pg 38)
PCNSC	(Sandia's) Physical, Chemical, and Nano Sciences Center (pg. 6)
PDMS	Poly(dimethylsiloxane) (pg. 43)
PEVA	Polyethylene Vinyl Acetate (pg. 43)
PL	Photoluminescence (pg. 22, 34)
QASPR	Qualification Alternatives to the Sandia Pulsed Reactor (pgs. 6, 8, 10, 12, 14)
QW	Quantum Well (pg. 32, 34)
RH	Relative Humidity (pg. 45)
SEM	Scanning Electron Micrograph (pgs. 54)
SP	Surface Plasmons (pg. 66)
SPR	Sandia Pulse Reactor (pg. 6, 10, 12)
SSL	Solid State Lighting (pg 36)
TEM	Transmission Electron Microscope (pg. 32)
uEHBL	Undoped Electron-Hole Bilayer (pg. 64)
UV	Ultra-violet (pg. 30, 38)
VLS	Vapor-Liquid-Solid (pg. 55)
VP	Vacancy Phosphorus (pg. 14)
XRD	X-Ray Diffraction (pg. 24,)
YSZ	Yttria Stablalized Zironia (pg. 48)

SAND2008-7810P: *Research Briefs* for the Physical, Chemical, & Nano Sciences Center is published by Sandia National Laboratories, a multiprogram laboratory operated by Sandia Corporation, a Lockheed Martin Company, for the United States National Nuclear Security Administration and the Department of Energy under Contract DE-AC04-94AL85000.

Printed 2008